Transfer of Polarized Light in Extended Atmospheres
Applied to Exoplanets and Titan

Sushen Joshi

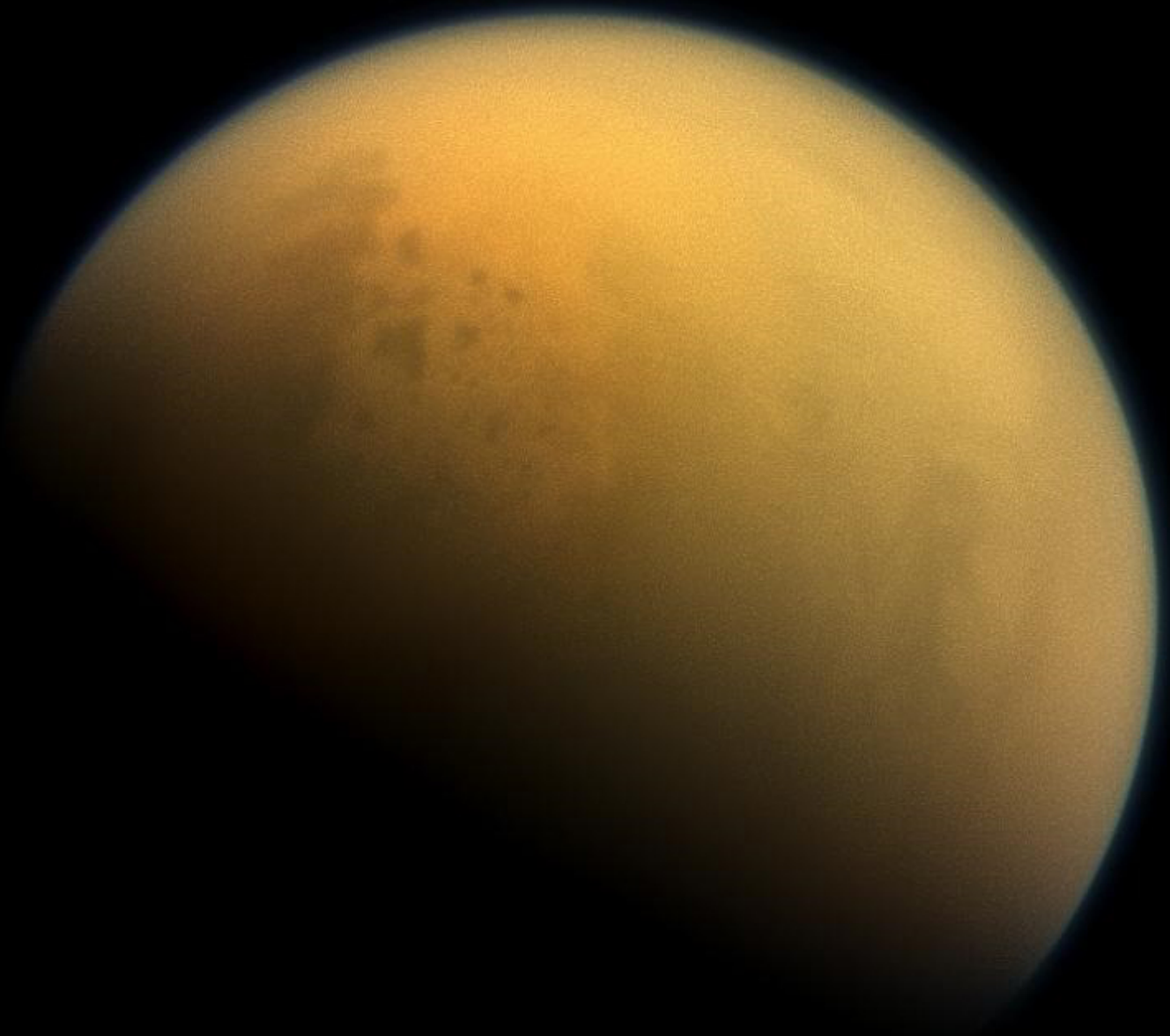

Technische Universiteit Delft

TU Delft

Transfer of Polarized Light in Extended Atmospheres

Applied to Exoplanets and Titan

by

Sushen Joshi

to obtain the degree of Master of Science
at the Delft University of Technology,
to be defended publicly on Monday May 31, 2021

Student number:	4898338	
Thesis committee:	Dr. D. M. Stam	Delft University of Technology (Supervisor)
	Dr. W. van der Wal	Delft University of Technology
	Dr. P. M. Visser	Delft University of Technology

An electronic version of this thesis is available at http://repository.tudelft.nl/.

Cover image: Titan's northern seas and lakes observed by Cassini spacecraft's Imaging Science System instrument using special spectral filter. Credit: NASA/JPL-Caltech/Space Science Institute.

TU Delft

Acknowledgements

I have had the privilege to work with and learn from a renowned expert in radiative transfer and planetary sciences - my supervisor Dr. Daphne M. Stam. I express my sincerest gratitude towards her for guiding and providing me all the support, not only for the MSc. thesis but also for future studies. She gave me the freedom to try different things in the development of this thesis work while at the same time helped me to keep the work on track, which I consider to be a very important aspect of doing research. I express my sincere gratitude towards Dr. Wouter van der Wal and Dr. Paul Visser for their time and efforts to review this thesis and for their assessment during the defense.

I would like to thank my parents and my brother, who always supported my decisions and because of them, I am able to do things that I like. Their support and understanding helped me to put more time into my work in the last months of the thesis when I was at my home.

I was amazed to experience the helping nature in the research community. I would especially like to thank Dr. Barbara Whitney, an expert in Monte Carlo radiative transfer, who, even after she is retired and was in a hospital, helped me to understand the rejection sampling method. I would also like to thank Dr. Jessica Ramella-Roman and Dr. Tomas Stolker whose inputs helped me to correctly implement the Stokes vector calculations.

Finally, I would like to thank my friend, fellow student, and flatmate Shubham Kulkarni for being with me for the entire MSc. studies, and to all my friends in Delft who made this journey more beautiful.

Sushen Joshi
Delft-Pune, May 2021

Abstract

We have developed, from scratch, a 3D radiative transfer code based on the Monte Carlo method, that fully takes into account the spherical shape of a planetary atmosphere, multiple scattering, and the polarized nature of light. Accounting for the sphericity of an atmosphere is important for the analysis of observations near the planetary limb and the twilight zone, i.e. the regions on a planet where the parent star and/or the observer are low or even below the local horizon. In such regions, the widely used radiative transfer models that are based on the locally plane-parallel atmosphere approximation can lead to significant errors, especially for planets that have extended atmospheres. With our code, we simulate total flux and polarization signals of light that is reflected by spatially resolved and spatially unresolved planets with extended atmospheres. We discuss the effects due to the atmosphere's sphericity and compare against computations with a locally plane-parallel code. Our results are relevant both for the interpretation of observations of various Solar System planets and moons (with atmospheres) and for the investigation of total flux and polarization signals of exoplanets at all phase angles, including during transits. Especially hot Jupiters are likely to have extended atmospheres and to be detected in edge-on orbits with transits. During a transit, an extended atmosphere can strongly increase the amount of starlight that is measured, thus leading to a smaller derived planet size. We also specifically simulate the polarimetric signal of Titan, Saturn's largest moon that is known to have an extended atmosphere. We find that at small phase angles, as observed from Earth, Titan's limb is strongly affected by the sphericity of its atmosphere and that at large phase angles, as observed by a spacecraft like Cassini, Titan's brightness increases strongly due to forward scattered light.

Delft-Pune, May 2021

Contents

List of Figures

List of Tables

1

Introduction

Titan, Saturn's largest moon, is a unique satellite in the solar system having a dense, hazy atmosphere and is the only body apart from Earth, known to support stable liquid on its surface (Stofan et al., 2007). Though we learned a great deal about Titan's atmosphere and hydrocarbon lakes through NASA/ESA/ASI Cassini-Huygens mission we are yet to know many aspects of this enigmatic moon e.g. evolution of Titan's detached haze layer (Seignovert et al., 2021), surface (Brossier et al., 2018) which is shrouded by atmospheric haze, and we are yet to bring tighter constraints on the composition of its lakes and seas Cordier and Seignovert (2019), Mastrogiuseppe et al. (2016, 2018a,b). A wealth of Cassini data is yet to be analyzed and in coming years Titan will be observed from ground-based telescopes. Though lakes of Titan were extensively studied through Cassini using RADAR and unpolarized infrared wavelengths, they have not yet been studied in polarized visible and infrared wavelengths. On the other hand, Titan's haze was primarily studied using polarimetric observations obtained during the descent of Huygens probe in the equatorial region. But, a significant variation was observed in Titan's haze distribution over the latitudes (and altitudes) (Barnes et al., 2013, Hirtzig et al., 2013, Karkoschka, 2016), thus the constraints brought by polarimetric study of haze in the equatorial region might not apply exactly for the haze in other regions. Polarimetry has already been proven to be an important tool to understand the optical properties of atmospheric constituents as well as liquid surfaces. Cassini's Imaging Science Subsystem (ISS) instrument was equipped with many polarizing filters for visible as well as near-infrared wavelengths (Porco et al., 2004). Through some atmospheric windows, especially at 939 nm, ISS has taken some images of the northern seas of Titan using polarization filters (Cordier and Seignovert, 2019). Along with the Cassini data, recently polarimetric observations of Titan were obtained using an advanced ground-based polarimetric facility, Spectro-Polarimetric High-contrast Exoplanet REsearch (SPHERE (Beuzit et al., 2019)), augmented to Very Large Telescope (VLT) by Sylvestre et al. (2019) and those observations can be used to bring new constraints on the properties of Titan's north polar seas and the atmospheric haze.

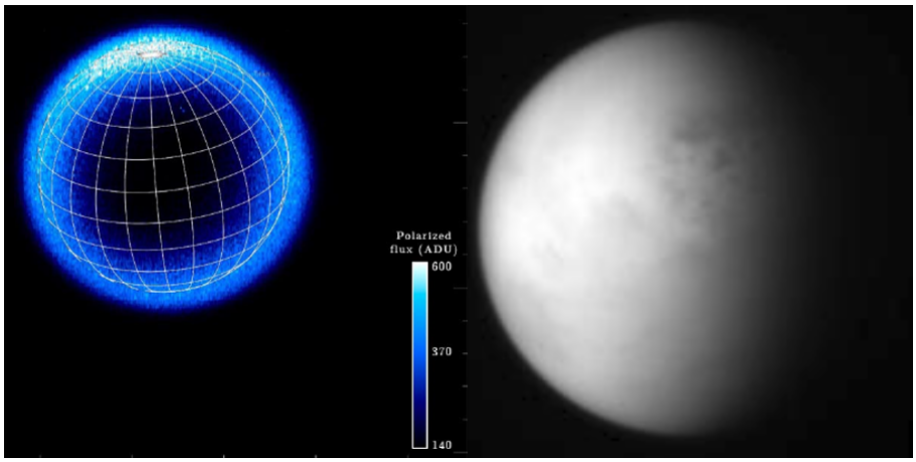

Figure 1.1: Left: Polarized flux of Titan viewed using N_R filter (617.5-674.2 nm) of SPHERE facility at the VLT (Sylvestre et al., 2019). Right: Titan's North polar seas (black patches near the terminator) observed using CB3 and IRP90 polarization filters of the Imaging Science Subsystem instrument onboard Cassini spacecraft.

Being a ground-based instrument, SPHERE measurements were taken at a small phase angle (an angle between the star and the observer as seen from the center of the planet/moon) while ISS observations were taken at large phase angles as Cassini spacecraft flew close to Titan. In the case of the SPHERE measurements, North polar lakes are located on Titan's limb (the outermost part of the observed planetary disk). Also, during Cassini flyby, the viewing geometry for ISS measurements was such that light coming from Titan's twilight zone (the regions on a planet where the parent star and/or the observer are low or even below the local horizon) was observed. These observations are shown in Figure 1.1. Titan is known to have an extended atmosphere due to its low gravity (it extends as high as 1000-1200 km considering its ionosphere, and Titan has a radius of 2575 km) and it was observed that using radiative transfer models that assume a plane-parallel atmosphere to study observations around Titan's limb introduces large errors. Due to its extended atmosphere, the twilight zone on Titan is broader than e.g. on Earth. Radiative transfer models that assume plane-parallel atmosphere neglect the light coming from the twilight zone of a planet/moon and thus cannot be used to study observations of the twilight zone of a planet/moon. This inspired us to develop a radiative transfer code that takes into account the sphericity of the atmosphere and fully considers the polarized nature of light.

Apart from Titan, observations of twilight zones of many other solar system objects such as Venus and Pluto are also available and those can be studied using radiative transfer models that consider a spherical atmosphere. Apart from solar system planets/moons, in the near future phase curves of reflected starlights from exoplanets will also be available e.g. through observations by Nancy Grace Roman Space Telescope (Spergel et al., 2013) slated to launch in 2025 or through the proposed missions (if they are approved) such as Large-Aperture UV-Optical-Infrared (LUVOIR) Mission (Bolcar et al., 2016) and The Habitable Exoplanet (HabEx) Imaging Mission (Mennesson et al., 2016). These observations may help us to better understand their atmospheres. Carrión-González et al. (2021) recently made a catalog of exoplanets accessible to Nancy Grace Roman Space Telescope's coronagraph in reflected starlight. They carried out a population study and also addressed the prospects for phase-curve measurements of those exoplanets. Some of these exoplanets may have extended atmospheres. Apart from this, taking into account the sphericity of the atmosphere may be important to study exoplanets that are expected to have extended atmospheres, such as puffy 'hot Jupiters' (gas giant exoplanets that have masses similar to Jupiter but orbit very close to their stars) e.g. HAT-P-1b, COROT-1b, TrES-4, WASP-17b, and Kepler-7b.

In this research, we have developed, from scratch, a 3D radiative transfer code based on the Monte Carlo method, that fully takes into account the spherical shape of a planetary atmosphere, multiple scattering, and the polarized nature of light. We named the code as Spherical POlarimetric Radiative Transfer (SPORT). After the development and validation of the code we investigated the following aspects of extended atmospheres for spatially resolved and spatially unresolved model planets:

- At what atmospheric geometrical thickness it is important to take into account the sphericity of the atmosphere and what is the effect of the extension of atmosphere on observed flux and polarization signals of a planet.
- What is the effect of the surface albedo on observed flux and polarization signals of a planet having an extended atmosphere.
- What is the effect of the single scattering albedo of scatterers in the atmosphere on observed flux and polarization signals of a planet having an extended atmosphere.
- Total flux and polarization signals of Titan using model atmospheres.

1.1. Report Structure

Chapter 2 describes how radiative transfer calculations in a planetary atmosphere are performed using SPORT. In Chapters 3 and 4 we present our simulation results. Chapter 3 focuses on spatially resolved images of total and polarized fluxes of model planets having different geometrical thicknesses of the atmosphere, having an extended atmosphere and different surface albedos, having an extended atmosphere and different single-scattering albedos of scatterers in the atmosphere, and Titan's atmosphere. Chapter 4 focuses on phase curves of total and polarized fluxes of spatially unresolved planets with the same settings discussed in Chapter 3. In Chapter 5 we present conclusions and a discussion of our results. We close with providing recommendations for future development of SPORT in Chapter 6.

2

Radiative Transfer in a Planetary Atmosphere Using SPORT

Radiation is a primary mechanism for energy transfer in space, through electromagnetic waves or their associated particles i.e. photons. According to Maxwell's equations, a spatially varying electric field is always associated with a magnetic field that changes over time. Likewise, a spatially varying magnetic field is associated with specific changes over time in the electric field. Based on this principle, in an electromagnetic wave, electric and magnetic components vibrate perpendicular to each other and the wave propagates in empty space until it interacts with some matter, where it is scattered or absorbed.

By convention, polarization of an electromagnetic wave refers to the confinement of vibration of the electric field to a certain plane. When it does not vibrate in a particular, fixed plane or when the plane is not rotating in a specific direction, the light can be said to be unpolarized. On the other hand, if it is, light can be, in general, said to be elliptically polarized, as the tip of the electric field vector can be imagined as tracing an ellipse in the empty space. Two special cases of elliptical polarization are linear and circular polarization. In linear polarization, the electric and magnetic fields oscillate in a single particular plane. In this project, we deal with only linear polarization as the contribution of circular polarization in the light reflected by planets is very low (see e.g. Rossi and Stam (2018)) and also the scatterers (gas molecules and haze particles) that we used in this project do not cause a circular polarization. The haze particles are described in Chapter 3.

Light, which we commonly measure, is the net effect of many simple waves and in general, it is partially polarized (Hansen and Travis, 1974). In extreme ends, it can either be completely polarized or unpolarized. An arbitrary incoming beam of light with total flux F consists of an unpolarized part and a polarized part (Hansen and Travis, 1974)

$$F = F_{unpol} + F_{pol} \tag{2.1}$$

The ratio F_{pol}/F is called as the degree of polarization. A complete description of an electromagnetic radiation i.e. the total flux and the state of polarization can be given by a Stokes vector (see e.g. Hansen and Travis (1974), Hovenier et al. (2004)), $\mathbf{F} = [F, Q, U, V]^{\mathrm{T}}$, where the Stokes parameter F represents the total flux, Q and U linearly polarized, and V the circularly polarized flux. We express these Stokes parameters in $\mathrm{W\,m^{-2}}$.

For a polychromatic light following inequality holds,

$$F \geq \sqrt{Q^2 + U^2 + V^2} \tag{2.2}$$

From Stokes parameters thus we can define flux of unpolarized and a linearly polarized light as:

$$\begin{aligned} F_{unpol} &= F - \sqrt{Q^2 + U^2} = F - F_{pol} \\ F_{pol} &= \sqrt{Q^2 + U^2} \end{aligned} \tag{2.3}$$

While the degree of polarization is expressed as:

$$P = \frac{F_{pol}}{F} = \frac{\sqrt{Q^2 + U^2}}{F} \quad 0 \leq P \leq 1 \tag{2.4}$$

Stokes parameters Q and U are always defined with respect to some reference plane and they can be transformed from one reference plane to another using the following rotation matrix (see e.g. Hovenier et al. (2004) or Hovenier and van der Mee (1983))

$$\mathbf{L}(\sigma) = \begin{bmatrix} 1 & 0 & 0 & 0 \\ 0 & \cos 2\sigma & \sin 2\sigma & 0 \\ 0 & -\sin 2\sigma & \cos 2\sigma & 0 \\ 0 & 0 & 0 & 1 \end{bmatrix} \tag{2.5}$$

Where σ is the angle between reference planes and it is considered positive if the initial reference plane is rotated through this angle in the anticlockwise direction when looking in the direction of propagation of the light beam.

As mentioned in Chapter 1, in this project, we are using the Monte Carlo method for radiative transfer calculations in a planetary atmosphere. The Monte Carlo method, in general, is a stochastic approach that repeats a certain experiment multiple times, directed by random sampling from a certain probability distribution function. At the crux of all Monte Carlo methods are random numbers. In the Monte Carlo Radiative Transfer (MCRT), we deal with "photon energy packets" (often referred to simply as a photon) and their interactions with the matter in a medium (Wood et al., 2013). In a simple way, radiative transfer in a planetary environment in the Monte Carlo context can be viewed as: a photon is emitted, it travels some distance, and then something happens to it e.g. scattering or absorption in the atmosphere, or reflection or absorption by the surface. We keep track of all these events until the photon is terminated after e.g. escape from the atmosphere or getting absorbed in the atmosphere or by the ground. In MCRT, photon paths and interactions or scattering events are simulated by sampling randomly from various probability distribution functions that determine photon's probabilistic path length, scattering angles, and also absorption rates. Although, note that we do not use molecular absorption in this research.

Development of the MCRT code used in this project (SPORT) comprised the major part of the thesis work. Though the principles of MCRT are discussed in the literature, it is challenging to convert them into a working computer model and because Monte Carlo is a stochastic method there are several parameters that affect the final desired output and there can be many ways that something can go wrong during the code development. Thus, rigorous testings, sensitivity analysis for different parameters, and validations were done throughout the code development. Figure 2.1 shows flow-chart of the current version of SPORT. In the next sections, code features are described step-by-step.

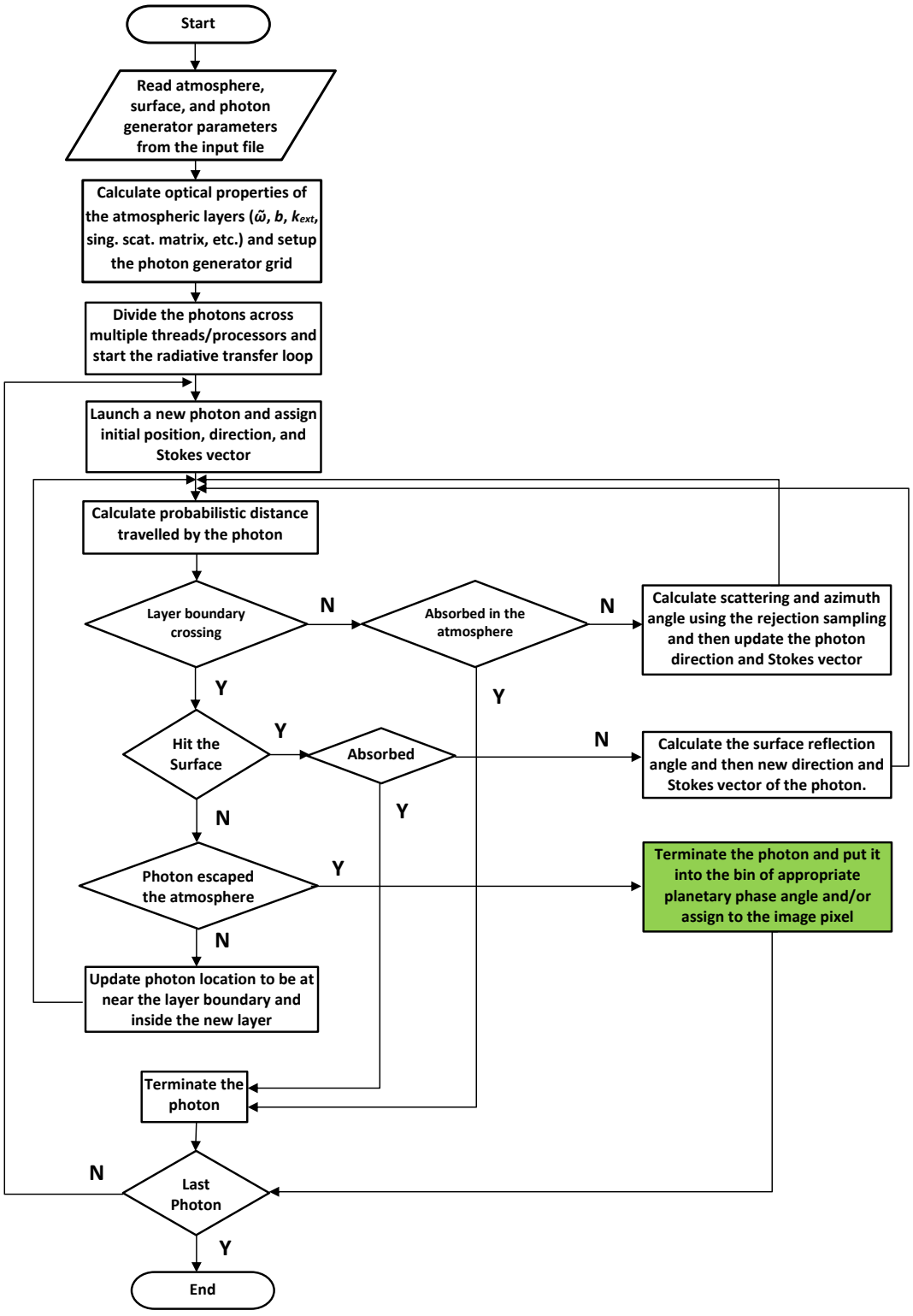

Figure 2.1: Flow-chart of SPORT code.

2.1. Setting up the atmosphere

Atmospheric constituents (gases, haze, etc.) scatter the light incident on them. The scattering matrix **P** gives the resultant angular distribution and polarization of the scattered light for any polarization of incident light and it is defined in the scattering plane i.e. the plane containing the incident and scattered light. In many practical applications, **P** is taken as a function of only the scattering angle, θ, with at most six independent parameters for symmetric particles (e.g. spherical) (Hansen and Travis, 1974):

$$\mathbf{P}(\theta) = \begin{bmatrix} P^{11} & P^{21} & 0 & 0 \\ P^{21} & P^{22} & 0 & 0 \\ 0 & 0 & P^{33} & -P^{43} \\ 0 & 0 & P^{43} & P^{44} \end{bmatrix} \tag{2.6}$$

This special case is valid for (1) randomly oriented particles, who have a plane of symmetry, (2) randomly oriented asymmetric particles if half of the particles are mirror images of the others. In the most generalized form, the matrix is completely filled, where all the 16 elements may have non-zero values.

Element P^{11} in matrix **P** is called a phase function and it represents the probability for the scattering of unpolarized incident light in a given direction. **P** is normalized such that

$$\int_{4\pi} P^{11} \frac{d\Omega}{4\pi} = 1, \tag{2.7}$$

where $d\Omega$ is an element of a solid angle. Thus, the probability that the incident light is scattered into 4π steradians is unity.

Scattering by gases i.e. by particles whose size is much smaller than the wavelength of the incident light is described by Rayleigh scattering. The Rayleigh scattering optical thickness for a particular gas can be calculated as:

$$b^m_{\text{sca}}(\lambda) = N_{\text{gas}} \sigma_{\text{sca}} \tag{2.8}$$

where the subscript sca and the superscript m mean 'scattering' and 'molecule', respectively, N_{gas} is the column number density (m^{-2}) and σ_{sca} is the Rayleigh scattering cross-section (m^2) of gas molecules in a particular atmospheric layer. N_{gas} can be computed as:

$$N_{\text{gas}} = N_A \frac{P_{\text{bottom}} - P_{\text{top}}}{mg} \tag{2.9}$$

where N_A is the Avogadro's constant, P_{bottom} and P_{top} are the pressures at the bottom and top of the layer, respectively, m is the mass of one mole of gas in atomic mass units and g is the acceleration due to gravity. σ_{sca} can be computed as:

$$\sigma_{\text{sca}} = \frac{24\pi^3}{N_L^2} \frac{(n_r^2 - 1)^2}{(n_r^2 + 2)^2} \frac{6 + 3\delta}{6 - 7\delta} \frac{1}{\lambda^2} \tag{2.10}$$

where N_L is the Loschmidt's number (molecules/m^3) depicting the gas particle density, n_r is the wavelength-dependent real refractive index of the gas molecule, λ is the wavelength considered, and $\frac{6+3\delta}{6-7\delta}$ is the depolarization term or the King factor in which δ is the depolarization factor or the depolarization ratio.

The Rayleigh scattering matrix has the elements as (Hansen and Travis, 1974):

$$\mathbf{P}(\theta) = \Delta \begin{bmatrix} \frac{3}{4}(1+\cos^2\theta) & -\frac{3}{4}\sin^2\theta & 0 & 0 \\ -\frac{3}{4}\sin^2\theta & \frac{3}{4}(1+\cos^2\theta) & 0 & 0 \\ 0 & 0 & \frac{3}{2}\cos\theta & 0 \\ 0 & 0 & 0 & \Delta' \frac{3}{2}\cos\theta \end{bmatrix} + (1-\Delta) \begin{bmatrix} 1 & 0 & 0 & 0 \\ 0 & 0 & 0 & 0 \\ 0 & 0 & 0 & 0 \\ 0 & 0 & 0 & 0 \end{bmatrix} \tag{2.11}$$

where

$$\Delta = \frac{1-\delta}{1+\delta/2} \quad \text{and} \quad \Delta' = \frac{1-2\delta}{1-\delta} \tag{2.12}$$

The depolarization factor (δ) is wavelength dependent and it represents the ratio of intensities parallel and perpendicular to the plane of scattering for the unpolarized incident light scattered at $\theta = 90^o$. Thus, it describes the effect due to molecular anisotropy. $\delta = 0$ for isotropic Rayleigh scattering and generally $0 \leq \delta \leq 0.5$ (Hansen and Travis, 1974). Equation 2.17 from Hansen and Travis (1974) shows that anisotropy reduces the degree of polarization for all scattering angles.

A single atmospheric layer can have multiple types of constituents e.g. different gases, aerosols, etc., that can have different optical properties. Scattering of light in a particular layer can be treated with the overall optical properties of the layer that are obtained by combining the optical properties of those of its constituents. The main entities that we need are, single scattering albedo, scattering matrix, and the optical thickness of the layer, which can be computed as (from Stam et al. (1999))

$$\tilde{\omega}_{\text{layer}}(\lambda) = \frac{b^m_{\text{sca}}(\lambda) + b^a_{\text{sca}}(\lambda)}{b^m_{\text{sca}}(\lambda) + b^m_{\text{abs}}(\lambda) + b^a_{\text{sca}}(\lambda) + b^a_{\text{abs}}(\lambda)} \tag{2.13}$$

$$\mathbf{P}_{\text{layer}}(\theta, \lambda) = \frac{b^m_{\text{sca}}(\lambda)\mathbf{P}^m(\theta, \lambda) + b^a_{\text{sca}}(\lambda)\mathbf{P}^a(\theta, \lambda)}{b^m_{\text{sca}}(\lambda) + b^a_{\text{sca}}(\lambda)} \tag{2.14}$$

$$b_{\text{layer}}(\lambda) = b^m_{\text{sca}}(\lambda) + b^m_{\text{abs}}(\lambda) + b^a_{\text{sca}}(\lambda) + b^a_{\text{abs}}(\lambda) \tag{2.15}$$

where $\tilde{\omega}_{\text{layer}}$ refers to the single-scattering albedo that gives the probability that the photon is scattered, b refers to the optical thickness, the superscripts m and a represent 'molecule' and 'aerosol', respectively, and the subscripts sca and abs represent 'scattering' and 'absorption', respectively. Note that we do not use molecular absorption in this research.

In SPORT, atmospheric layers have a spherical shape and multiple layers are dealt with as concentric spherical shells. Also, there are no restrictions on the size and number of layers. Using the atmospheric layer's geometrical thickness l (which is defined in the radial direction or perpendicular to the spherical shell of the layer) and the calculated optical thickness, the extinction (i.e. scattering + absorption) coefficient k_{ext} (m^{-1}) of a layer is then calculated as

$$k_{\text{ext}} = \frac{b_{\text{layer}}}{l} = \frac{N\sigma_{\text{ext}}l}{l} = N\sigma_{\text{ext}} \tag{2.16}$$

where N is the number density of scatterers and absorbers and σ_{ext} is the extinction cross-section. This is an important entity in MCRT and its use will be discussed in Section 2.3.

2.2. Photon generator and photon's initial properties

The main coordinate system used to keep track of photon events is a global Cartesian coordinate system having its origin at the center of a planet/moon and is illustrated in Figure 2.2.

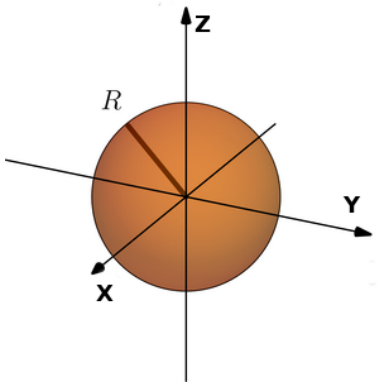

Figure 2.2: The main coordinate system used to keep track of photon events. The origin of the coordinate system is at the center of a planet/moon. R represents the radius of a planet/moon. Illustration figure adapted from: Brilliant.org

SPORT uses a square (or rectangular) photon generator. Using the input file for a simulation, photon generator physical dimensions viz. length and width in kilometers and grid dimensions viz. the number of rows and columns can be specified. Also, the number of photons per grid cell is specified in the input file. Thus, the incident stellar flux on the planet/moon is split into the total number of photons that we wish/need to track. By default, the photon generator then generates a raster of photons in the x,z space, and the initial x and z coordinates being the coordinates of the center of the grid cell. Then by inverting the equation $y = \sqrt{R^2 - x^2 - z^2}$, the y coordinate is found; here R = radius of the planet + altitude of the top of the atmosphere. Thus, every photon has a 3D initial position on the spherical atmosphere top and initially, their direction of propagation is along the +y direction. The initial direction can be tweaked according to the desired geometry for radiative transfer calculations. The front and side views of the illumination are illustrated in the figure 2.3

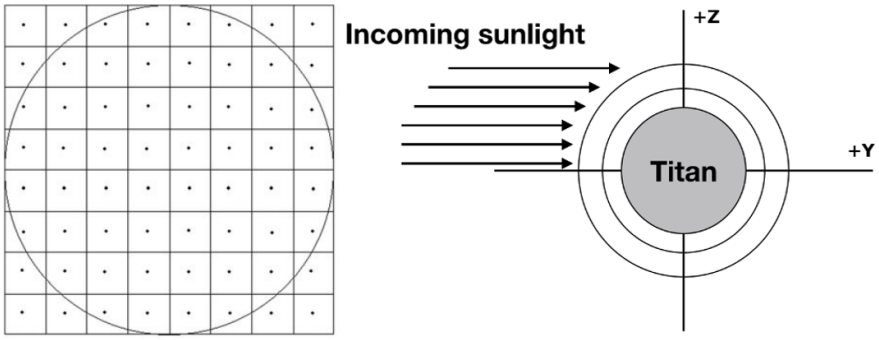

Figure 2.3: **Left**: Example of the front view of the planet/moon's (here Titan's) illumination using the square photon generator. Titan's disk is inscribed inside the photon generator. **Right**: Side view of the illumination. Titan's gray solid body is surrounded by concentric atmospheric layers. The X-axis is pointing out of the screen/paper.

A photon's direction is described by a Cartesian 3D unit vector (hereafter, direction vector) whose elements are the direction cosines i.e. cosines of angles between photon's direction with respect to the positive directions of X, Y, and Z axes. For the illumination geometry used in this project, which is shown in Figure 2.3, the initial direction vector for all photons is **dir** = [0,1,0]. The light coming from the Sun can be considered as unpolarized light (Kemp et al. (1987)), thus, the initial Stokes vector of photons is given by [1,0,0,0], and it can be changed if necessary.

2.3. Traversing photon's journey in a planetary atmosphere-surface system

In this section, we will discuss how photon's probabilistic distances are computed and how scattering and surface reflection events are tracked in SPORT.

2.3.1. Estimating photon distance travelled

The discussion in this subsection is based on Wood et al. (2013) unless specified otherwise. In a planetary atmosphere, photons undergo probabilistic interactions governed by extinction cross-sections of the particles in the atmosphere. In general, in a homogeneous medium with a geometrical thickness L, incident and outgoing fluxes, F_{in} and F_{out}, respectively are related by

$$F_{\text{out}}(L) = F_{\text{in}} e^{-N\sigma L} = F_{in} e^{-k_{\text{ext}} L} \tag{2.17}$$

where k_{ext}, the extinction cross-section depicts the fraction of photons scattered or absorbed per unit length. This gives us an important quantity - photon mean free path, $1/N\sigma$, which is nothing but the average distance a photon travels between interactions. Thus, the probability that a photon interacts i.e. either scattered or absorbed by the particle over a length L is $N\sigma L$ i.e. the optical thickness, b. In physical essence, the optical thickness over a distance L in a given direction is nothing but the number of photon mean free paths over that distance.

Since there is a probability distribution function associated with the photon path length, the distances traveled are not uniformly chosen from all space $L\{0,\infty\}$ and thus, we must sample optical thickness (b) such that its chosen values "fill in" the respective probability distribution function (PDF), $P(b)$. In SPORT, the probabilistic distance l_p that the photon will travel in a particular atmospheric layer is calculated as

$$l_p = \frac{1}{k_{\text{ext}}} \log \frac{1}{\xi} \tag{2.18}$$

where ξ is a random number sampled uniformly from the range 0 to 1. Thus, in SPORT, we need to sample how far a photon travels before interacting. The probability that it travels an optical thickness b without interaction is e^{-b}. And thus, the probability of scattering prior to b is $1 - e^{-b}$.

Depending on the value of l_p, a photon can either cross the atmospheric layer or undergo an interaction in the same layer. SPORT uses a ray-tracing technique to determine if the photon's path crosses the atmospheric layer using the line-sphere intersection equations. If the photon crosses the layer's boundary, its location is updated to be at the boundary (the photon is now inside the new layer) while its traveling direction remains the same. Again a new random number is generated and using the k_{ext} of the new layer, a new l_p is determined.

If the photon interacts in the same layer it is either

- absorbed or scattered in the atmosphere which is dependent on the $\tilde{\omega}_{\text{layer}}$. If the photon is absorbed, it is no longer tracked and a new photon is emitted. If it is scattered, it travels in a new direction that is determined by elements P_{11} (the phase function) and P_{12} from the scattering matrix of the particle (their role in determining the new direction is explained in Subsection 2.3.2).
- absorbed or reflected by the surface (if the photon is in the lowermost atmospheric layer and if there is a surface), which depends on the surface albedo.

2.3.2. Photon direction calculation and Stokes vector update after scattering

A photon's direction and Stokes vector need to be updated when it interacts with a scattering particle because the scattering event generally changes its direction as well as the Stokes vector. Figure 2.4 depicts the scattering geometry in a local scattering reference frame, where a photon is scattered by a particle and the scattered direction is determined by the scattering angle θ ([0, π] radians) and the azimuth angle ψ ([0, 2π] radians). The plane containing the incident as well as the scattered direction of a photon is called the scattering plane.

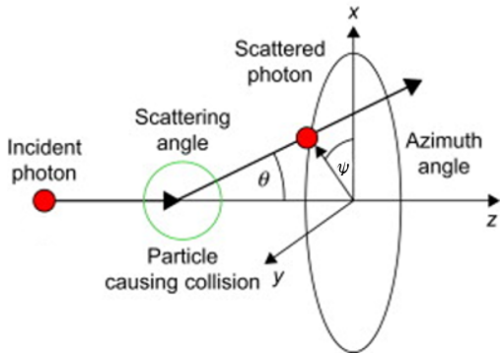

Figure 2.4: Figure depicting the scattering geometry. The angles θ and ψ determine the scattered direction. The X-Y-Z coordinate system is the local scattering coordinate system. Illustration figure adapted from Szirmay-Kalos et al. (2011).

In SPORT, we use rejection sampling to sample/determine angles θ and ψ (see e.g. Whitney (2011), Wood et al. (2013), or Ramella-Roman et al. (2005)). When we deal with polarization of a light, we need to generate three random numbers ξ_1, ξ_2, and ξ_3 for the rejection sampling. Using those random numbers θ and ψ can be sampled as follows:

1. Sample a random scattering angle, θ_r as $\theta_r = acos(2\xi_1 - 1)$
2. Sample random ψ_r as $\psi_r = 2\pi\xi_2$

3. Determine the scattering probability for these angles as (Ramella-Roman et al., 2005)

$$P(\theta_r, \psi_r) = P_{11}(\theta_r)F_{\text{in}} + P_{12}(\theta_r)[Q_{\text{in}}\cos 2\psi_r + U_{\text{in}}\sin 2\psi_r] \tag{2.19}$$

   where $F_{\text{in}}, Q_{\text{in}}, U_{\text{in}}$ are the Stokes parameters of the photon incident on the scattering particle.

4. Generate a random deviate $P_r = F_{\max}(\theta, \psi)\xi_3$ where $F_{\max}(\theta, \psi)$ is the maximum value the scattered total flux F can have for the given incident Stokes vector.

5. If $P_r \leq P(\theta_r, \psi_r)$, accept θ_r, ψ_r otherwise repeat from Step 1.

From Step 4 it can be seen that to use the rejection sampling, we need to know the maximum value of the scattered flux, $F_{\max}$ beforehand. This can be determined numerically by calculating the values of scattered fluxes (Eq. 2.19) for all combinations of θ, ψ, and Stokes vectors and then picking the maximum value. Indeed as described in Whitney (2011), we also found that this maximum value to be $P_{11}(0)$ for the scattering matrices used in this research.

From Eq. 2.19 it can be seen that the probability of photon scattering in a certain direction depends not only on $P_{11}(\theta)$ but also $P_{12}(\theta)$. This is when we take the polarization into account to determine the scattering direction. When we ignore the polarization, the scattering probability is dependent on $P_{11}(\theta)$ only and the Eq. 2.19 reduces simply to $P(\theta_r) = P_{11}(\theta_r)F_{\text{in}}$, thus requiring to randomly sample only θ_r in the rejection loop (ψ will needed to be sampled only once in this case and is sampled outside the rejection loop).

After θ and ψ are sampled, we calculate new direction cosines of the photon that are defined with respect to the global Cartesian reference frame (Figure 2.2). Direction cosines after scattering (kx_{new}, ky_{new}, and kz_{new}) are then calculated using direction cosines before scattering (kx_{old}, ky_{old}, and kz_{old}) as:

if $|kz_{old}| \approx 1$ i.e. if photon travels parallel to Z axis:

$$\begin{aligned} kx_{new} &= \sin\theta\cos\psi \\ ky_{new} &= \sin\theta\sin\psi \\ kz_{new} &= \cos\theta\frac{kz_{old}}{|kz_{old}|} \end{aligned} \tag{2.20}$$

else:

$$\begin{aligned} kx_{new} &= kx_{old}\cos\theta + \frac{\sin\theta(kx_{old}kz_{old}\cos\psi - ky_{old}\sin\psi)}{\sqrt{1-kz_{old}^2}} \\ ky_{new} &= ky_{old}\cos\theta + \frac{\sin\theta(ky_{old}kz_{old}\cos\psi + kx_{old}\sin\psi)}{\sqrt{1-kz_{old}^2}} \\ kz_{new} &= ky_{old} - \sqrt{1-kz_{old}^2}\sin\theta\cos\psi \end{aligned} \tag{2.21}$$

Once we obtain the new direction cosines of the photon, we update its Stokes vector using so-called meridian planes first introduced in Chandrasekhar (1950) and further elaborated in e.g. Hovenier and van der Mee (1983) and Hovenier et al. (2004) as below:

$$\mathbf{F_{scat}} = \mathbf{LPLF_{inc}} \tag{2.22}$$

where $\mathbf{F_{inc}}$ and $\mathbf{F_{scat}}$ are the Stokes vectors of the incident and scattered photon, respectively, $\mathbf{L}$ is the rotation matrix as described in Equation 2.5, and $\mathbf{P}$ is the scattering matrix. We need Stokes vector rotations because the scattering matrix is defined with respect to the scattering plane. The Stokes vector of the incident photon is defined with respect to the meridian plane consisting of the Z-axis of the global Cartesian coordinate system and photon's direction before scattering. It is then rotated to the scattering plane so as to multiply it by the scattering matrix. After that, it is rotated to the meridian plane containing the Z-axis of the global Cartesian coordinate system and photon's direction after scattering in this coordinate system. There are several ways

to obtain the rotation angles used in the rotation matrix which produce the same end result for the equation 2.22. In SPORT, the way described in Ramella-Roman et al. (2005) is used (except the direction cosines; they are updated using Eq. 2.20 - 2.21). After the Stokes vector is updated, it is normalized using the first Stokes parameter i.e. F to follow the conservation of energy principle, and the resulting Stokes vector looks like

$$\mathbf{F}_{\text{Scat}} = \begin{bmatrix} 1 \\ Q_{\text{scat}}/F_{\text{scat}} \\ U_{\text{scat}}/F_{\text{scat}} \\ V_{\text{scat}}/F_{\text{scat}} \end{bmatrix} \tag{2.23}$$

Note that this equation can be used directly when we consider only scattering in the atmosphere. When we also consider the absorption, we also need to keep track of the 'weight' of the photon i.e. how much energy is still remained in the photon, and then multiply this weight to the final Stokes vector when the photon exits the atmosphere.

2.3.3. Photon direction calculation and Stokes vector update after surface reflection

In the current version of SPORT, we use a Lambertian surface, which reflects the light isotropically. When the photon is not absorbed by the surface and is reflected, first the surface reflection angle θ_{refl} is calculated as (Modest, 2013):

$$\theta_{\text{refl}} = asin(\sqrt{\xi}) \tag{2.24}$$

where ξ is a random number. Equation 2.24 represents the reflection function of a Lambertian surface.

After obtaining the local surface reflection angle, first, the direction vector of the photon in the local East-North-UP (ENU)[1] coordinate frame is calculated, and then, the direction vector in the global Cartesian coordinate system is calculated.

Lambertian surface completely depolarizes the light, hence the Stokes vector after the surface reflection is updated as $A_S[1, 0, 0, 0]$, where A_S is the surface albedo.

2.4. Generation of planetary phase functions and images

Once the photon exits the atmosphere to space, the exit azimuth and elevation (with respect to the planetary equatorial plane) of its direction vector is calculated and the photon is put in a bin of the appropriate planetary phase angle, which is the angle between the star and the observer as seen from the center of the planet/moon as shown in Figure 2.5.

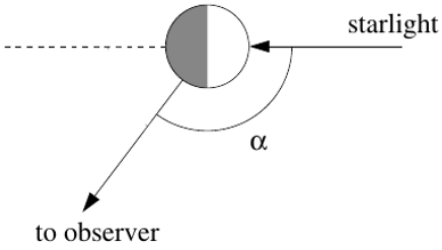

Figure 2.5: Planetary phase angle α. Illustration figure adapted from Stam and Hovenier (2005).

The phase function of a planet depicts the brightness of a planet viewed from different planetary phase angles e.g. phases of the Moon or the Venus. It can give information about the planetary atmosphere (if present) such as atmospheric composition and optical properties, and surface reflection properties making it a valuable tool for planetary studies. The reflected planetary flux at a particular wavelength can be described as (Stam, 2008):

$$F_r(\alpha, \lambda) = A_G(\lambda)\varphi(\alpha, \lambda)\pi B(\lambda, T_S)\frac{R_P^2 R_S^2}{d^2 D^2} \tag{2.25}$$

[1]Transformations between planet-centered, planet-fixed and ENU coordinate system: https://gssc.esa.int/navipedia/index.php/Transformations_between_ECEF_and_ENU_coordinates

Where
- A_G is the geometrical albedo of the planet which is the ratio of the brightness of the planet/moon at $\alpha = 0°$ to the brightness of the Lambertian disk of same radius illuminated with the same amount of irradiance. The planet/moon can have a different A_G for a different λ.
- $\varphi(\alpha, \lambda)$ is the wavelength dependent phase function of a planet/moon and its values at different phase angles describe the brightness of the planet/moon relative to the brightness at $\alpha = 0°$ (thus $\varphi(0, \lambda) = 1$).
- T_s is the temperature of the star and $B(\lambda, T_S)$ is its wavelength dependent brightness.
- R_P and R_S is the radius of the planet/moon and Star, respectively.
- D is the orbital radius of the planet and d is the distance to the observer.

Depending on what kind of analysis is needed to be done, the phase curve of the planetary flux can either be represented as the phase function, $\varphi(\alpha, \lambda)$ or it can be normalized such that at $\alpha = 0°$, it represents the A_G of the planet (in principle, $A_G \varphi_\alpha(\lambda)$).

In SPORT, with changing the filter for the elevation of exit direction (basically, kz_{exit}: direction cosine with the global Z axis), phase function for different observing conditions e.g. from the Earth or from the spacecraft can be generated.

Stokes vector of the photon exiting the atmosphere is defined with respect to the meridian which contains the photon exit direction and the global Z axis. This Stokes vector needs to be rotated to the common reference plane to have consistency across all the planetary phase angles. To simulate the observations taken from the Earth, the common reference plane to which the Stokes vector of the exiting photon is rotated is taken as the plane containing star-planet and planet-observer lines. In general, this plane can also be called the planetary scattering plane.

Apart from planetary phase functions, SPORT can also generate 2D planetary images for any phase angle and is flexible with the image resolution (pixel rows and columns).

2.5. Statistical errors, simulation run times, and model code parallelization

Wood et al. (2013) mention the random sampling errors accompanied in Monte Carlo simulations as $E/\sqrt{N_i}$, where E is the physical property under investigation (e.g. planetary Stokes parameters) and N_i is the number of photons. Thus, care needs to be taken to include at least a minimum number of photons in the calculations to minimize the statistical fluctuations in the physical property under investigation.

The program has been built in a way that not all photons are needed to be in computer's RAM at a time and their journey in the atmosphere is independent of each other. The first aspect allows a generation of a large number of photons and thus improving the S/N ratio ($\sqrt{N_i}$) and the second aspect allows a complete parallelization of the code as each photon will have its journey not dependent on other photons. Parallelization is needed to reduce computation time, especially for a dense hazy atmosphere like that of Titan. The OpenMP framework of the Fortran language was used for code parallelization.

2.6. SPORT Validation

Validation is an important process in the development of any new code to ensure that the code produces expected results and is free of or has minimum errors. SPORT was validated at various stages throughout its development. First, using the simple case of Lambertian sphere without having an atmosphere. The reflected flux $F_r(\alpha)$ at different phase angles of Lambertian sphere with a surface albedo A_S can be given by an analytical equation (see e.g. van de Hulst (1980)). Here, $F_r(0)$ represents geometrical albedo (A_G) of the Lambertian sphere.

$$F_r(\alpha) = \frac{2}{3\pi} A_S(\sin\alpha + \pi\cos\alpha - \alpha\cos\alpha) \tag{2.26}$$

After this, the validation was first done for the version dealing with only flux (i.e. polarization not considered) and then for the version which fully considers flux and polarization using the benchmark results from the

already proven code based on the adding-doubling method (which assumes the atmosphere to consist of plane-parallel layers) and was used in Stam et al. (2004). The validation results are shown in Figure 2.6.

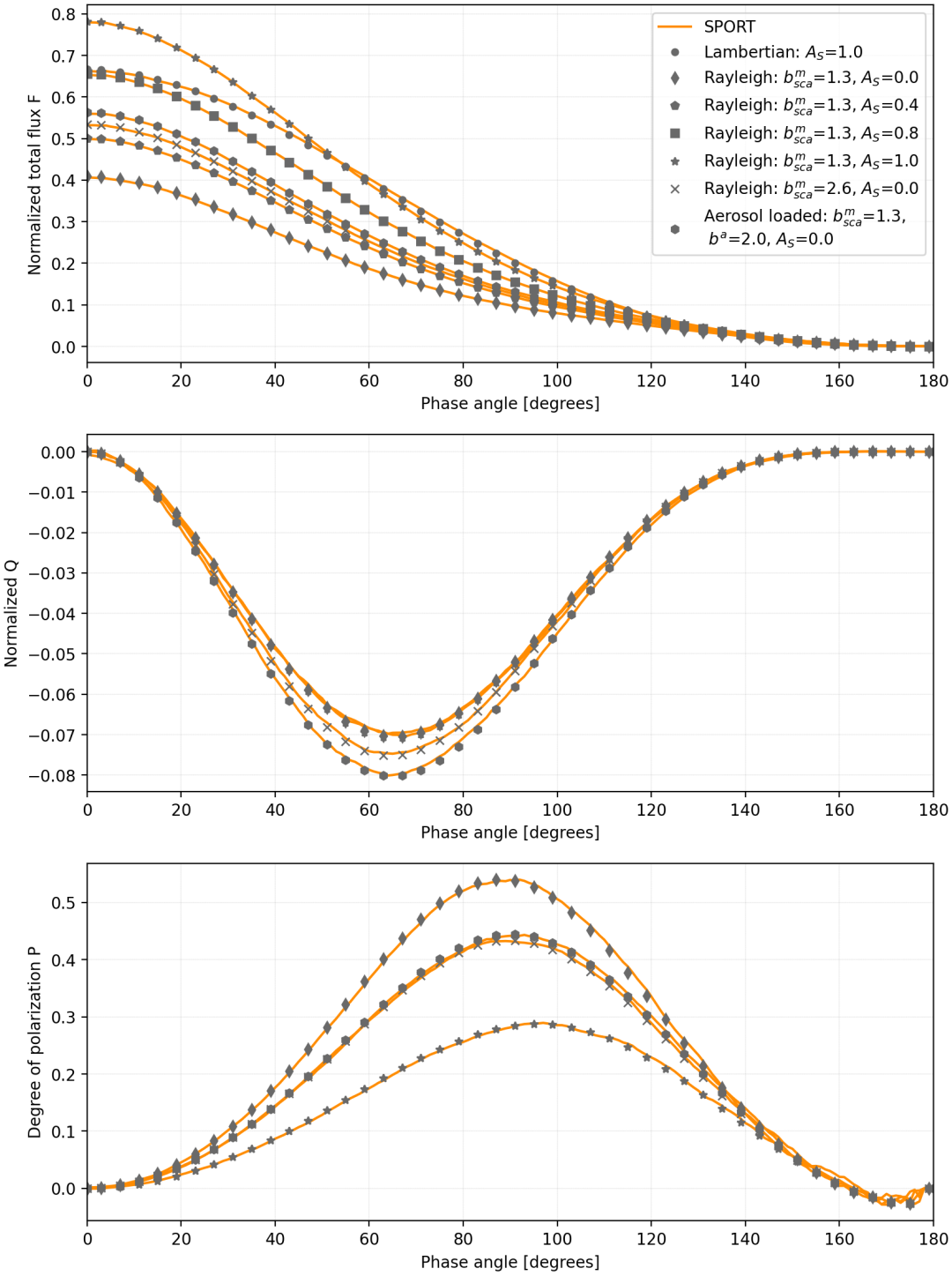

Figure 2.6: Validation results of SPORT for different model settings. The total flux F is normalized such that at $\alpha = 0°$ F represents the geometric albedo of the planet. To normalize Q the same factor which was used to normalize F was used. The degree of polarization, P is calculated as $-Q/F$. The atmosphere is divided into three layers with each layer having the thickness of 2 km and b^m_{sca}=1.0,0.2,0.1 from bottom-most to the top-most layer for a total b^m_{sca} of 1.3. The depolarization factor for Rayleigh scattering was taken to be 0.0279 (depolarization factor of Earth's purely molecular air). For a total b^m_{sca} of 2.6, b^m_{sca} of each layer is multiplied by 2. Aerosol is loaded in the bottom-most layer. A_S depicts the surface albedo. Orange lines represent SPORT output, while markers represent benchmark values. For the Lambertian sphere Equation 2.26 was used for benchmark, while for the atmosphere-surface validations phase curves generated using the adding-doubling code used in Stam et al. (2004) was used.

In Figure 2.6, SPORT results are shown by orange curves, while the markers represent benchmark results. For the validation of Lambertian reflection, Equation 2.26 was used. Markers for a planet with an atmosphere (represented by labels Rayleigh: and Aerosol loaded:) represent the benchmark results from adding-doubling code used in Stam et al. (2004). For the comparison with results from the adding-doubling method, we considered a planet with a radius of 2575 km (radius of Titan) and a geometrically very thin atmosphere with a total geometrical thickness of 6 km in SPORT simulations. This setting closely simulates the plane-parallel atmosphere approximation due to a very low extent of the atmosphere. The atmosphere was divided into 3 layers with each layer having a geometrical thickness of 2 km. We used purely molecular as well as aerosol loaded atmosphere i.e. atmosphere consisting of molecules and aerosols and we did comparisons for many combinations of optical depths and surface albedos as shown in legends of the graphs in the figure. In the figure, the first panel represents the total flux F which is normalized such that at phase angle $\alpha = 0°$, the total flux represents the geometric albedo of the planet. The second panel represents the normalized Stokes parameter Q of the reflected light from the planet. We used the same factor to normalize Q that we used to normalize total flux F. The third panel represents the degree of polarization which was calculated as $P = -Q/F$. Here the $-$ sign provides the information about the direction of polarization. $P > 0$ (<0) indicates that the scattered light is polarized perpendicular (parallel) to the scattering plane, which is the planetary scattering plane (described in Section 2.4) in this case. From F,Q, and P curves we can see that SPORT produces results very close to the benchmark values and the difference is almost indistinguishable in many cases and thus we can say that SPORT can be used to study reflected total and polarized fluxes of a planet(ary atmosphere).

3

Results: Spatially Resolved Planets

In this chapter, we discuss total flux and polarization signals (images) of disk resolved planets having different atmospheric extent, surface albedo (A_s), and the single scattering albedo ($\tilde{\omega}$) of atmospheric particles.

Single scattering matrix elements (Eq. 2.6) of the scatterers (molecules and haze) used in this research are shown in Figure 3.1. The haze particles are used to simulate Titan's atmosphere and are described in Section 3.4.

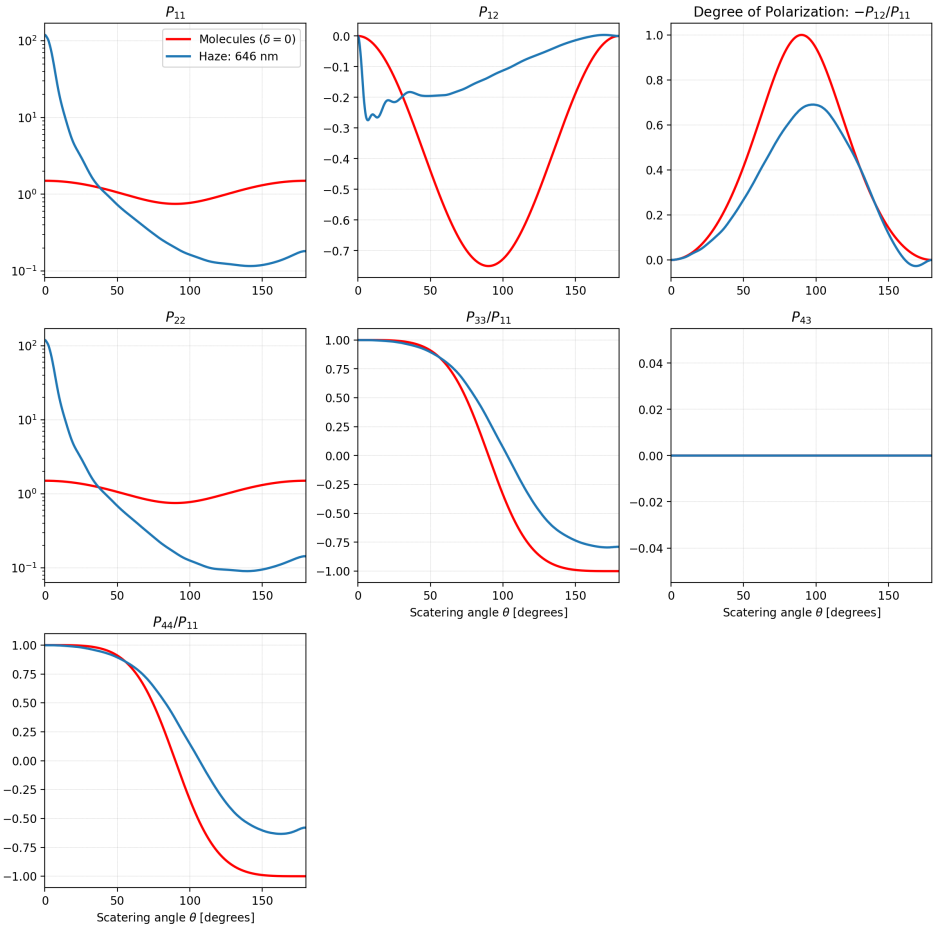

Figure 3.1: Single scattering matrix elements of molecules (Rayleigh scattering) and the aggregate haze particles used in this research. Phase functions P_{11} are normalized using Eq. 2.7. From P_{11} it can be seen that haze particles strongly scatter light in the forward direction. The degree of linear polarization (P) after single scattering is calculated as $-P_{12}/P_{11}$. Here the $-$ sign provides the information about the direction of polarization. $P > 0$ (<0) indicates that the scattered light is polarized perpendicular (parallel) to the scattering plane i.e. the plane containing incident and scattered light.

3.1. Effect of the geometrical thickness of the atmosphere

In SPORT, as we are considering atmospheric layers as spherical shells we can investigate the effect of the sphericity of the atmosphere on the observed flux and polarization signals when the extent of the atmosphere increases. We discuss our investigation for this effect in this section.

3.1.1. Atmospheres consisting of single homogeneous layer

To study this effect, we first did an investigation with a simple planet having an atmosphere consisting of only one layer and we did simulations for different geometrical thicknesses of the atmosphere. In the following text, when we refer to the thickness of the atmosphere we mean the geometrical thickness unless specified otherwise. Also, by the thin (thick) atmosphere we mean an atmosphere having a smaller (larger) extent.

We considered a hypothetical planet/moon of a radius of 2575 km (radius of Titan; we used this radius for all simulations done in this research) and the surface albedo was set to 0 so as to decouple the contribution from the surface and investigate solely the atmospheric effect. The b^m_{sca} of the atmosphere was chosen to be 1.3. We considered a purely molecular (i.e. gaseous) atmosphere and the depolarization factor was taken to be 0.0279 (Earth-like purely gaseous air). The investigation of increasing atmospheric extent was done relative to the planet of a size of 2575 km, but these principles should apply to planets with other sizes as well, as they are relative. We present here atmospheres with thicknesses of 30, 300, 600, and 1200 km. Disk resolved images for $\alpha = 0°$ for these cases are shown in Figure 3.2. In all the cases, the planet was irradiated with the same number of photons (3927280000).

First thing to notice is how the total flux (hereupon, F) appears over the disk. It looks nearly uniform for the major part of the disk except near the limb (the outermost part or the edge of the disk). Near the limb, due to the sphericity of the atmosphere, the percentage of light ultimately scattered back to the $\alpha = 0°$ (in this case) is smaller than in the inner part of the disk. Thus we see the gradient and eventually smaller flux near the edge of the disk. Near the limb we primarily see the light that travelled longer distance in the atmosphere than at the central part due to the sphericity of the atmosphere. It can be seen that this effect increases as the thickness of the atmosphere increases. This is because, when we increase the geometrical thickness of the atmosphere while keeping the optical thickness same, the atmosphere becomes more tenuous. This leads to more photons in the limb region travelling longer distance and ultimately not returning back to the smaller phase angles.

Q and U show clear structures (yellow and black lobes) for the thinner atmosphere and they start to fade with the increase in the atmospheric extent; this is because, for the thinner atmosphere, scatterers (i.e. gas molecules) are concentrated at comparatively smaller region. Also, as we are using a (horizontally) homogeneous atmospheric layer, we see the symmetry in the disk resolved Q and U images. Remember that Q and U are defined with respect to the planetary scattering plane. We see lower values for Q, U, and thus the total polarized flux and P in the central part of the disk for all atmospheric thicknesses, because in this part we see the higher percentage of light which is singly scattered in the backward direction (scattering angles closer to 180°). If we look at the element P_{12} from the single scattering matrix of molecules (figure 3.1), we see that the light scattered at these larg scattering angles have very small polarization. On the other hand, around the limb, we see the light that is traveled longer distance in the atmosphere and the percentage of light scattered twice (second-order scattering) is also higher (this was confirmed by tracking the number of times photons scatter for every image pixel). In this case, light scatters twice with scattering angles near to 90°. From the P_{12} of the single scattering matrix of molecules, it can be seen that the light scattered near $\theta = 90°$ has the highest polarization. Though the multiple scattering reduces P as compared to the singly scattered light with θ around 90°, it is still significant to have a high P. With the increasing atmospheric thickness, P values become noisier around the limb. This is because P is a relative quantity and the noise increases as the number of photons contributing to F decreases. Thus, care needs to be taken so as not to erroneously interpret noisy P values as high P values, especially around the limb. For all the P images in this research, the noise threshold ($1/\sqrt{\text{number of photons}}$) was taken to be 0.1 unless specified otherwise, to filter out the noisy pixels. Below this threshold, a significantly low number of pixels remained in the P images of the atmosphere with 1200 km thickness for the chosen incoming flux.

Figure 3.3 shows variation of F and P across the equatorial part of the planetary disk. For each atmospheric case, every data point in F and P graphs represent their values for a horizontal pixel for the vertical image

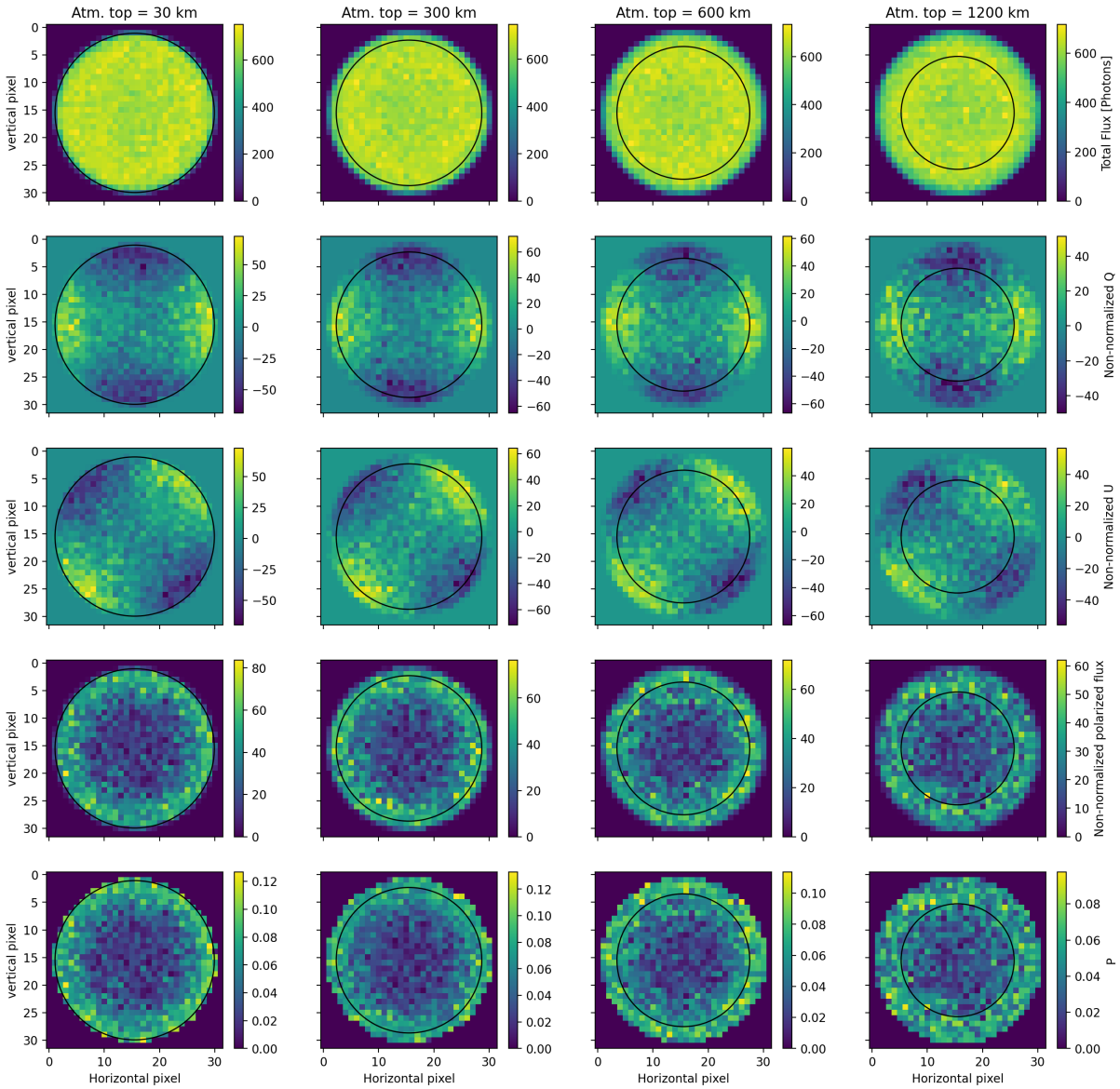

Figure 3.2: Disk resolved images at $\alpha = 0°$ for a planet with increasing atmospheric geometrical thickness. The atmosphere consists of only one layer. First to last rows depict the non-normalized total flux (F) in photons, Q, U, total polarized flux ($\sqrt{Q^2+U^2}$), and P, respectively. Each column represents those quantities for a particular atmospheric thickness (mentioned in the title of each column). Note that every image has a different colour-bar and the range of values represented by colour-bars might be different for a particular row in the figure. This is applicable to all the figures showing such images in this report. The black circle represents the projection of the surface in the case of a rocky planet.

pixel number 15 from Figure 3.2. Near the start and end of the graphs we see pixels near the limb while in the central part of graphs, we see pixels from the inner part of the disk. We see that, although P graphs show similar variation along the horizontal pixels for all atmospheric cases, F graphs show different variations with the increase in the atmospheric extent. From F graphs, we see that more pixels near the limb of the disk have smaller values than the central bright pixels when the atmospheric extent increases. Because we see clear variation in F graphs than in P with the change in thickness of the atmosphere, we find it to be a suitable parameter to further investigate at what atmospheric thickness effect of atmospheric sphericity around the limb starts to become large. The atmosphere with a thickness of 30 km closely depicts how the plane-parallel atmosphere model would represent the disk resolved planet. Thus, with this investigation, we want to see at what atmospheric thickness assumption of the plane-parallel atmosphere or ignoring the sphericity of the atmosphere will introduce large deviations in values of Stokes parameters around the limb of the planet. To do this investigation we used more atmospheric thicknesses in between 30 and 300 km. F graphs for the equato-

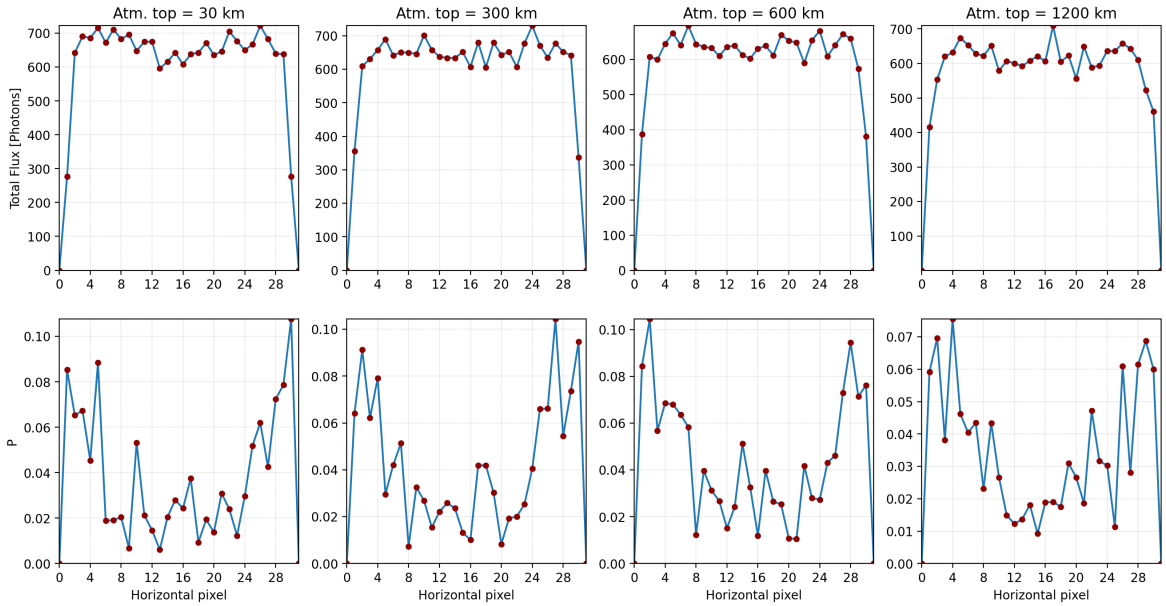

Figure 3.3: First and second rows representing total flux in photons and P, respectively for pixels along the equator (vertical pixel number 15) of planets shown in Figure 3.2.

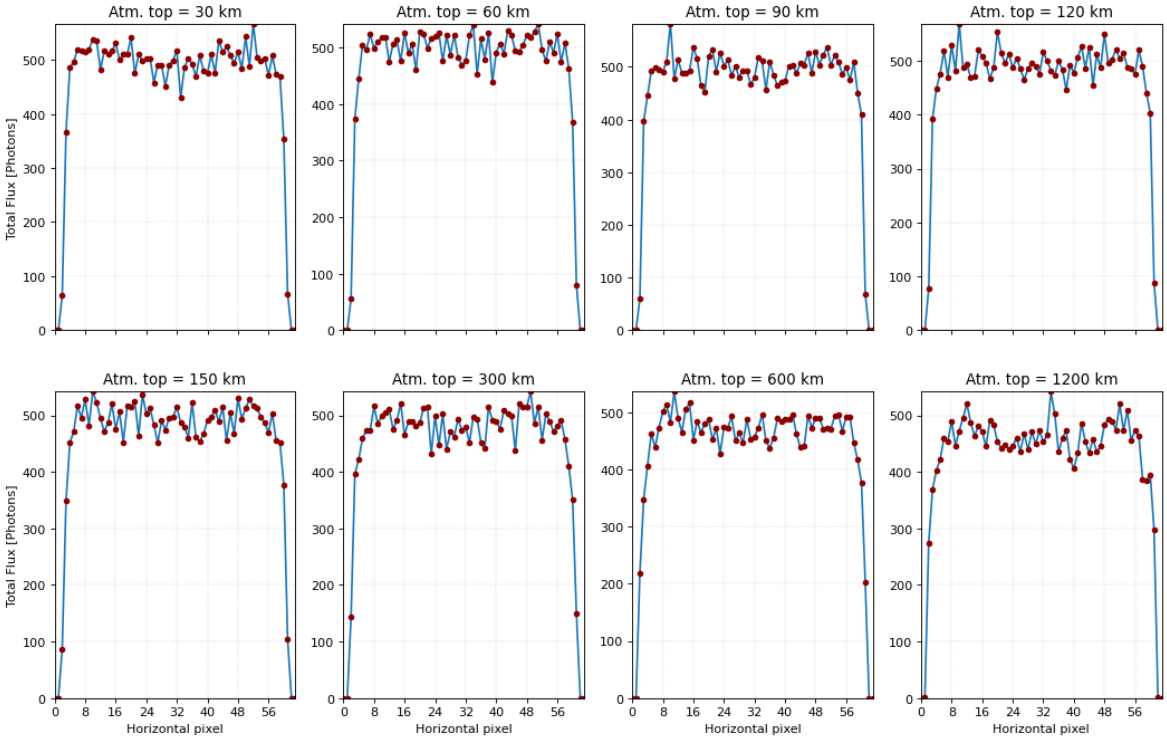

Figure 3.4: Graphs representing F values along the equator of planets with different atmospheric thicknesses (mentioned in the title of every graph) for $\alpha = 0°$. Graphs were produced using images of resolution of 64x64 pixels. To have a better S/N ratio we used three vertical pixel lines near the equator of planets.

rial part of the atmosphere cases presented in Figure 3.2 and additional atmospheric thicknesses between 30 and 300 km are shown in Figure 3.4. Note that we used images with 64x64 resolution for a better comparison among the different atmosphere cases. From Figure 3.4, though it seems to be a bit difficult to quantify the deviations in F values near the limb for different atmospheric thicknesses due to statistical fluctuations, we can see that starting from total thickness of 300 km we see more pixels near the limb have smaller F than

the atmospheric thicknesses smaller than 300 km. Thus, for this particular planet with the considered atmospheric properties in this section, we see that at smaller phase angles, the effect of sphericity starts to become larger from atmospheric extent of around 300 km.

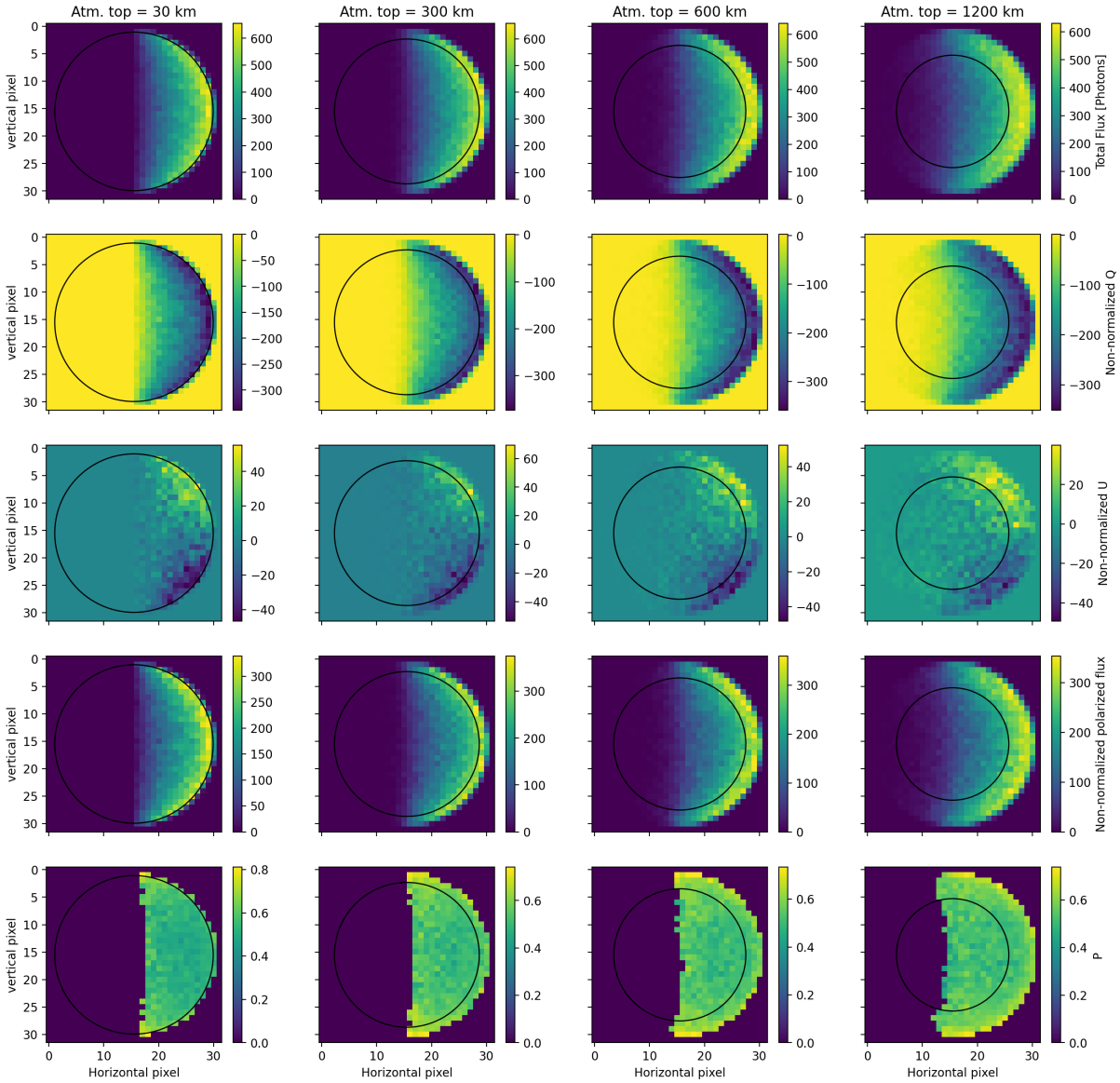

Figure 3.5: Same as figure 3.2, but for $\alpha = 90°$

In figure 3.5, disk resolved images for $\alpha = 90°$ are shown. We see a very sharp terminator (a line separating illuminated and non-illuminated parts of the planet) at the middle of the image for the atmosphere with 30 km thickness as compared to atmospheres with larger thicknesses. From all the images in Figure 3.5 it can be seen that as the atmospheric extent increases, the twilight zone (the region on the planet that is illuminated by scattered light, even though the star is below the local horizon) becomes broader. When the atmosphere is extended, even if the star is below the local horizon, photons that traveled longer in the atmosphere contribute to the flux from the extended twilight zone. Plane-parallel atmospheric models do not consider the light coming from the twilight zone and thus the non-illuminated part of the planet appears completely dark. Thus, spherical atmospheric models are extremely useful to study planetary signals from the twilight zone.

Note that Q values are higher at this phase angle than at $\alpha = 0°$, this is because, at this α, the percentage of light scattered around $\theta = 90°$ is higher, which produces the maximum polarization for the singly scattered

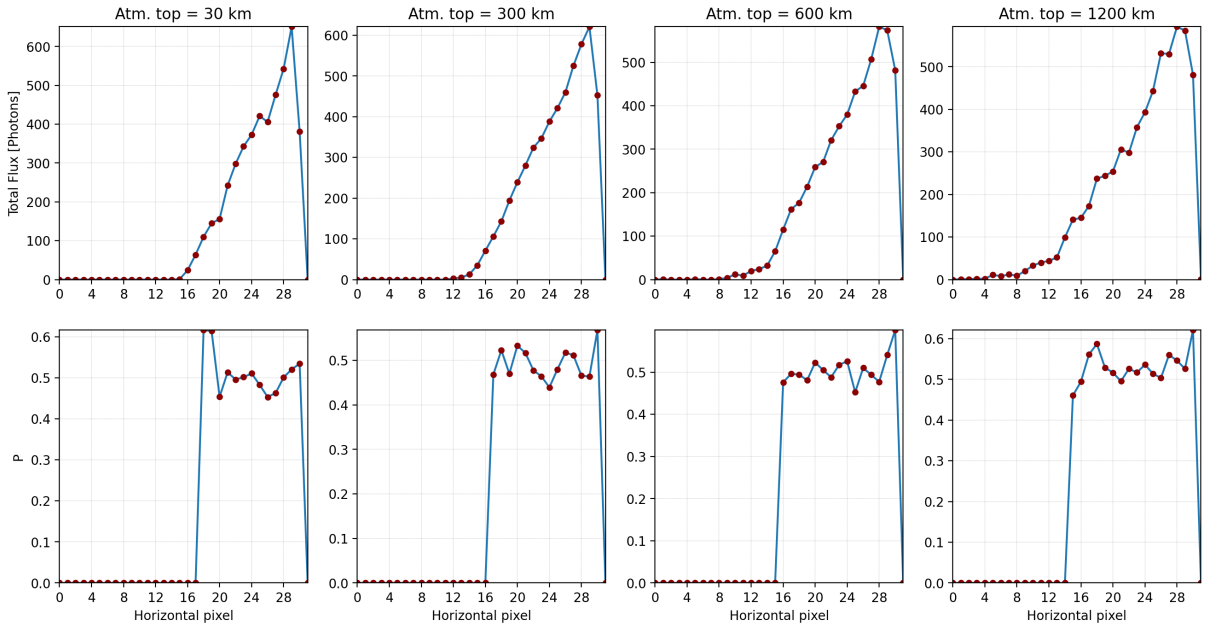

Figure 3.6: Same as Figure 3.3 but for $\alpha = 90°$.

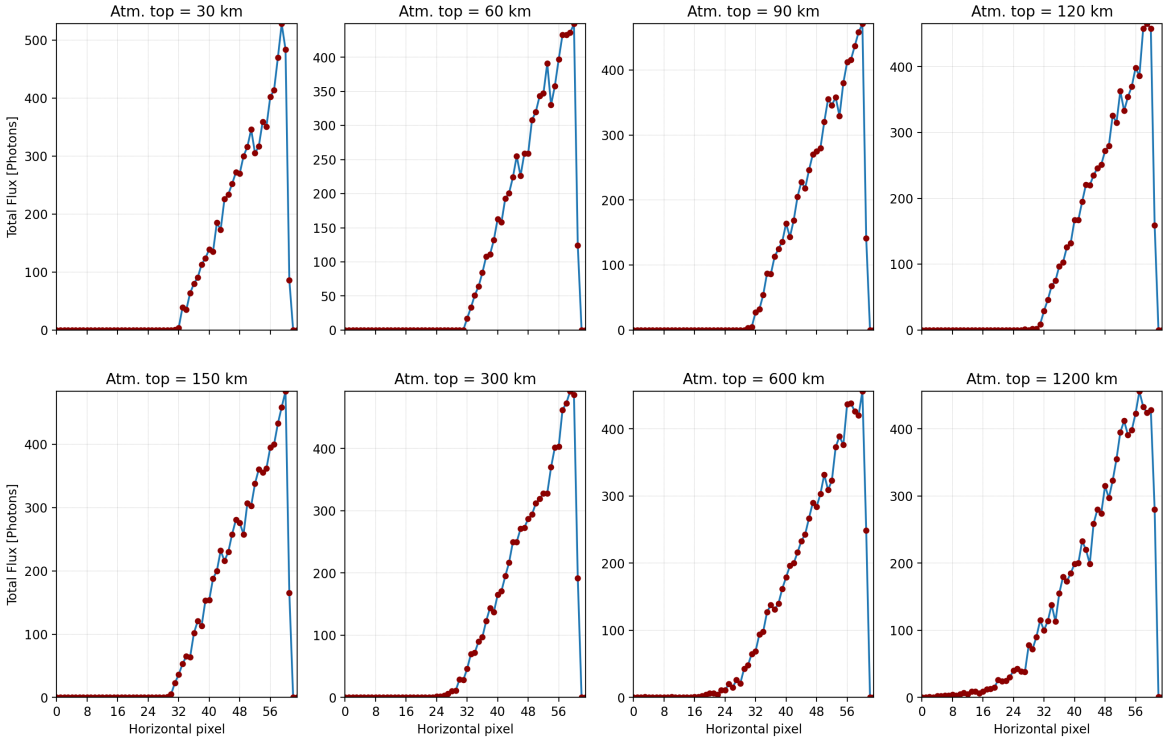

Figure 3.7: Same as Figure 3.4, but for $\alpha = 90°$.

light (see Figure 3.1). P images show a clear distinction from those for $\alpha = 0°$. It looks to be uniform across the illuminated part of the disk, contrary to the variation as seen for $\alpha = 0°$. At the extreme edges of the illuminated part of the disk, we primarily see the light which is singly scattered. In his region, we see higher P, than the other illuminated parts because P of the light scattered once at $\theta = 90°$ is higher than the one that scattered multiple times before e.g. getting scattered at around $\theta = 90°$. This is because P decreases with multiple scattering. We see this for the larger part of the limb with the increase in the atmospheric extent. This is because, the atmosphere becomes more tenuous and thus photons can have longer paths, thus increasing

the chance of singly scattered photons escaping the atmosphere. We were skeptical whether the pixels at the edge of the limb and near the terminator in P images are noisy. To rule this out, we did simulations with the triple number of photons to get a better signal-to-noise ratio and found that indeed the pixels in those regions represent the true signal. Figure 3.6 shows F and P variations across the equator of planets shown in Figure 3.5 for $\alpha = 90°$. From F and P graphs we see the broadening of the twilight zone. Horizontal pixel number 15 represents the terminator and values larger than this represent the illuminated part of the planet, while the lower pixel numbers represent the non-illuminated part of the planet. We see that more pixels get illuminated with the increase in the atmospheric thickness. To investigate from what atmospheric thickness the twilight zone starts to broaden significantly, we analyzed F graphs for the equatorial pixels for multiple atmospheric thicknesses along with the one presented in Figure 3.5. These graphs are shown in Figure 3.7. In these graphs horizontal pixel number 32 represents the terminator. From these graphs, we can see that for the atmosphere with 120 km thickness, the twilight is broadened very slightly, while for the atmosphere of 150 km thickness it is more noticeable and for 300 km it is very prominent. Thus, for $\alpha = 90°$ (or for large phase angles in general) considering the sphericity of the atmosphere is essential for the atmosphere with the thickness of 150 km, for the planet discussed in this section. This thickness is smaller than the one we found for $\alpha = 0°$.

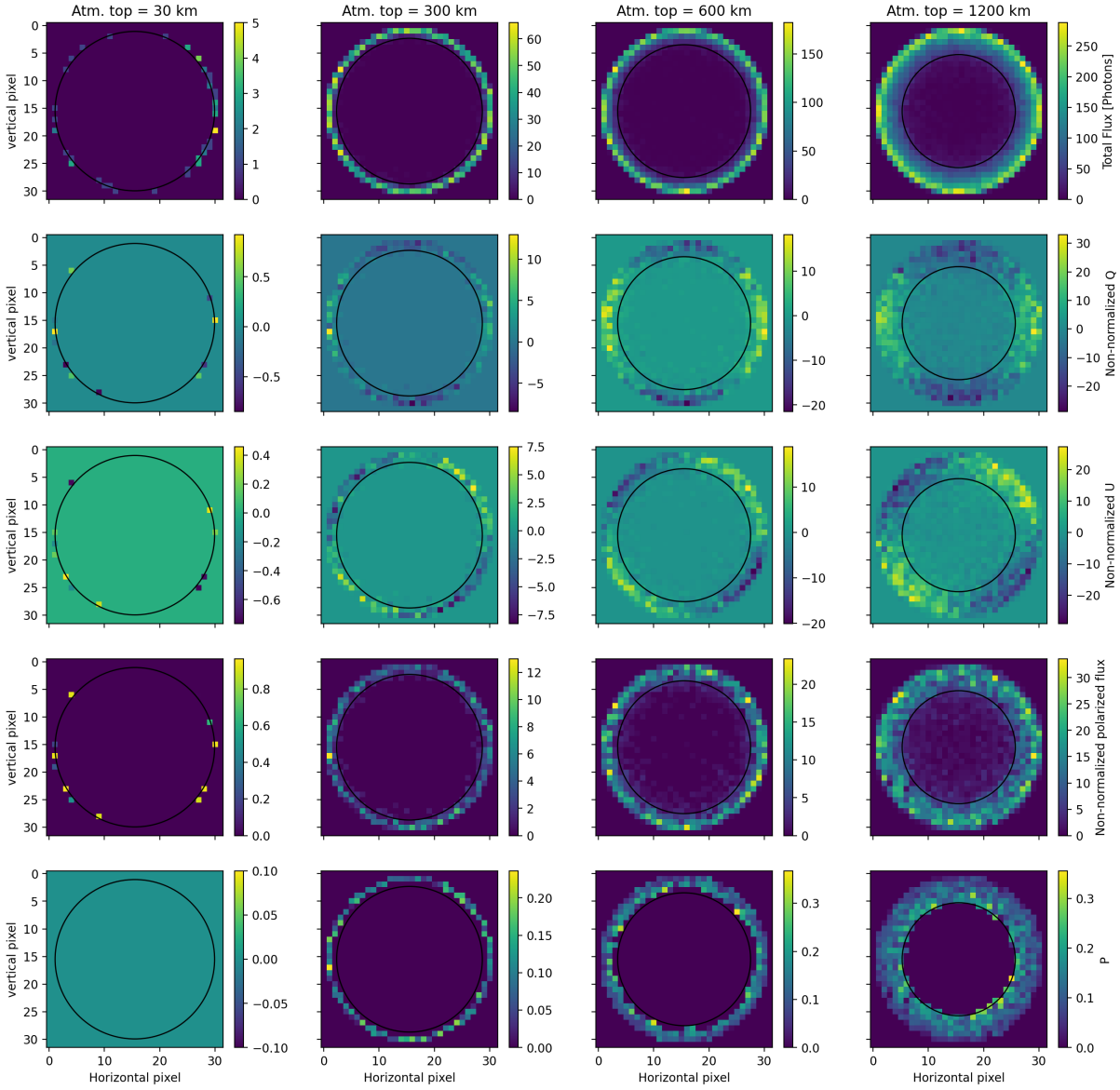

Figure 3.8: Same as Figure 3.9, but for $\alpha = 180°$

Figure 3.8 represents the disk resolved images for $\alpha = 180°$. Note that we only considered the photons that scattered at least once in the atmosphere and ignored the photons that passed through the atmosphere without any interaction. Also, we ignore the atmospheric refraction. At $\alpha = 180°$, we hardly see any flux for the atmosphere with 30 km thickness, and the total flux increases as the atmospheric extent increases. Also, We can see that F is higher near the limb than in the inner part of the visible and illuminated atmosphere. This is opposite to the flux distribution at $\alpha = 0°$. Thus, the majority of the photons at the limb are the ones that didn't contribute for the flux at $\alpha = 0°$ but contributed for $\alpha = 180°$ due to the sphericity of the atmosphere.

The high flux values for thicker atmospheres affect our interpretation of the size of the exoplanet during transits because a thinner and dense atmosphere will block most of the stellar light incident on the atmosphere causing the appropriate dip in the stellar flux, thus leading to better chances of having tighter constraints on its size. On the other hand, the extended atmospheres transmit and enhance the light due to forward scattering (which also depends on the scattering phase functions of the atmospheric constituents) and thus, in reality, we receive more light than the planet with a thinner atmosphere causing smaller dip in the stellar flux during the transit. This may lead to an interpretation that the planet has a smaller size than the actual one. When analyzing the transit spectroscopy data of exoplanets, usually the molecular absorption is considered and scattering is ignored. But from Figure 3.8, we can see that taking into account scattering as well can improve the characterization of the exoplanetary atmospheres through the transit method.

Like $\alpha = 0°$, Q and U have smaller values because the singly scattered light in the forward direction ($\theta \approx 0°$) by molecules has a very low polarization. Here we used a noise threshold of 0.2 for the P images, because with the threshold of 0.1, we could hardly see any pixel for the atmospheres with thicknesses of 300 and 600 km.

3.1.2. Atmospheres consisting of multiple layers, where layers have different geometrical thicknesses

In reality, planetary atmospheres are composed of many layers, generally having different optical and geometrical thicknesses i.e. they are vertically inhomogeneous. To investigate how the total flux and polarimetric signals for extended atmospheres with such layers would look like, we again considered atmospheres with different geometrical thicknesses, but now they are divided into three layers having b^m_{sca}=1.0, 0.2, 0.1 from the bottom-most to the top-most layer for a total atmospheric b^m_{sca} of 1.3. The layer sizes are as shown in Table 3.1. Figure 3.9 shows Stokes parameters and P for these atmospheres.

Total geometrical thickness of the atmosphere [km]	Layer 1, Layer 2, Layer 3 geometrical thicknesses [km]
30	5,10,15
300	50,100,150
600	100,200,300
1200	200,400,600

Table 3.1: Table depicting values of geometrical thicknesses of atmospheres and their constituting layers.

For the thinner atmosphere of 30 km thickness F looks more or less uniform over the disk, whereas as the extent of the atmosphere increases, the disk looks brighter in the central part and F decreases more towards the limb. Apart from the sphericity effect discussed in the case of the atmospheres with only one layer, there is also an effect of changing the atmospheric optical thickness. Here, in the central part of the disk, we mostly see the light reflected from the deeper and denser part of the atmosphere whereas around the solid body we see the light reflected by tenuous atmospheric layers where comparatively less scattering occurs than in the deeper part of the atmosphere. Looking at F image of the planet with a total thickness of 1200 km, we can even clearly see the distinction of the layers. Thus, with high-resolution images, it could be possible to better understand the stratification of the upper parts of extended atmospheres. Although, for a real planet it would be very difficult to observe such stratification if the upper part is primarily composed of gas because the gas density decreases gradually with altitude. However, if there are very sharp haze layers, it could be possible to observe the stratification. Now, even if the atmosphere is extended, in this kind of stratification, maximum Q and U signals come from the outer edges of the denser part of the atmosphere because of the more scatter-

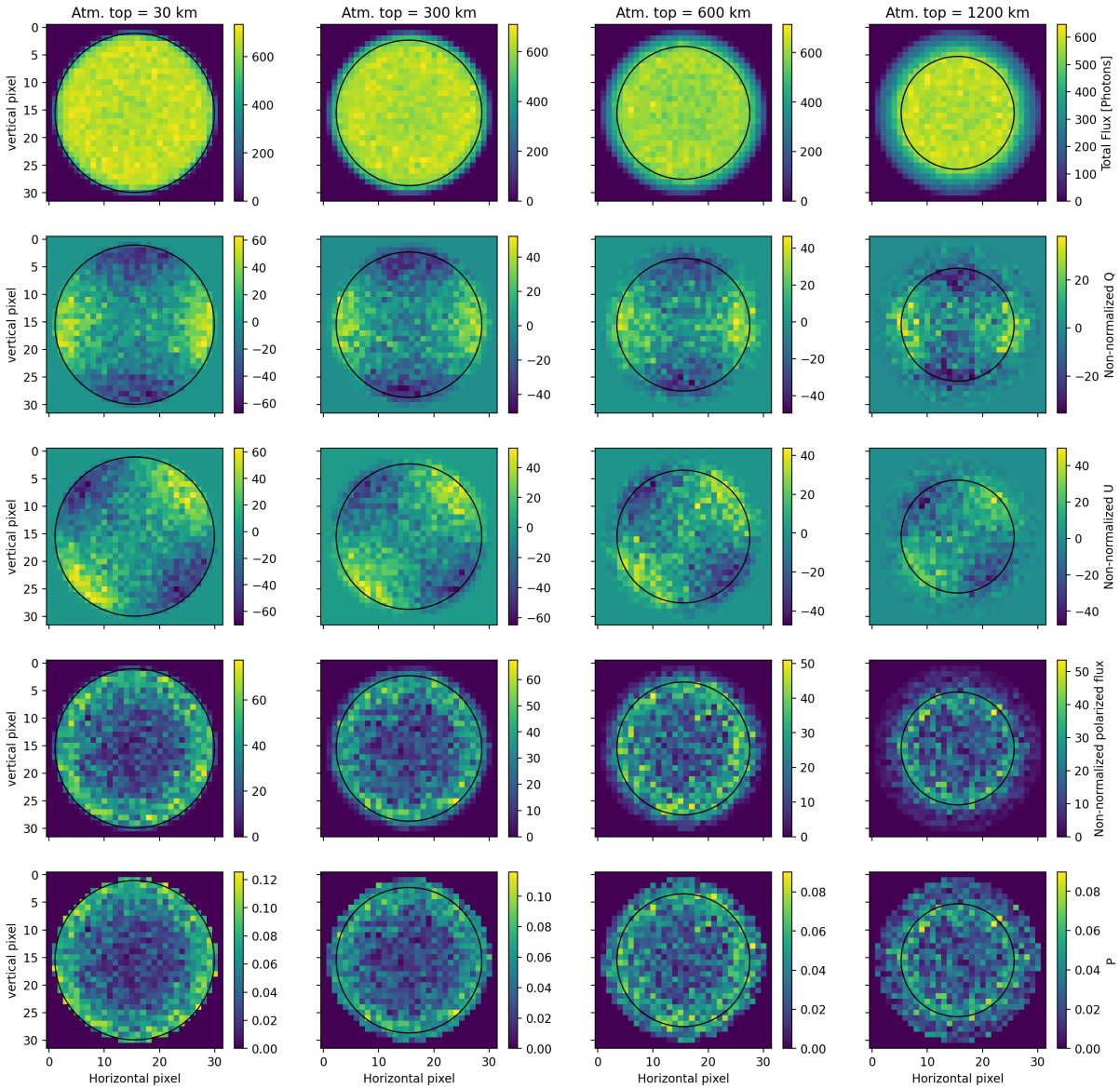

Figure 3.9: Same as Figure 3.2 but now atmospheric layers have thicknesses as described in Table 3.1 and have $b_{\rm sca}^{m}$=1.0, 0.2, 0.1 from the bottom-most to to the top-most layer.

ing occurring in the denser part. This also results in P to be maximum around the edges of the denser part of the atmosphere. Figure 3.10 shows the variation of F and P across the equatorial part of the disk for this case at $\alpha = 0°$. From F graphs we can see that F decreases significantly for the pixels in the outer part of the disk with increasing atmospheric extent. If we compare F graphs from Figures 3.3 and 3.10, we see that for atmospheres with thicknesses of 300, 600, and 1200 km, F decreases for more pixels in the outer part of the disk (and thus overall) for the vertically inhomogeneous atmosphere. From P graphs, we can also see that the atmospheric region from where we see the maximum P values shifts in the inner part of the visible disk with the increase in the atmospheric extent. Similar to the case with the atmospheres consisting of only one layer, we investigated from what atmospheric thickness we see large deviations for the observed flux values around the limb in this case. Figure 3.11 shows F graphs for the equatorial region of the disk for planets with atmospheric thicknesses of 30, 60, 90, 120, 150, 300, 600, and 1200 km for this case. We used images with resolution of 64x64 pixels to generate these graphs. From these graphs we can see that for the atmospheric thickness of 120 km significant number of pixels around the limb have lower F values. Recall that for the case of atmospheres consisting of only one layer, we found that at $\alpha = 0°$ the decrease in F values for large number of pixels was evident for atmospheric thickness of 300 km. This suggests that the effect of the sphericity of

the atmosphere on the observed flux values around the limb for smaller phase angles depends on how much tenuous the upper part of the atmosphere is.

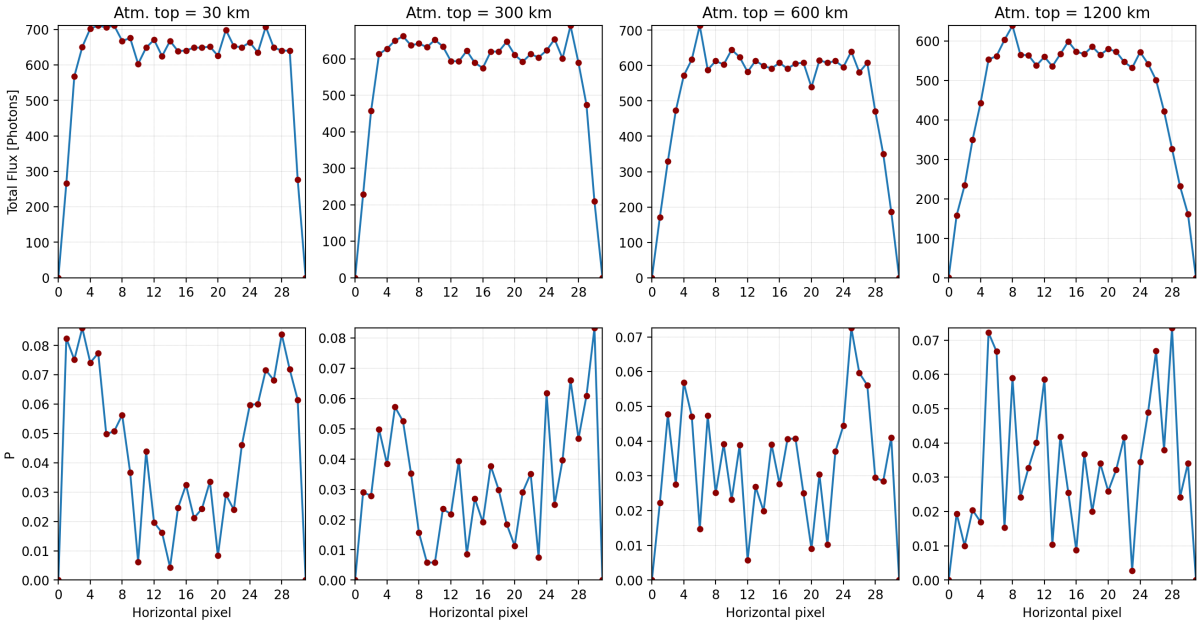

Figure 3.10: First and second rows representing F and P, respectively for the pixels along the equator (vertical pixel number 15) in Figure 3.9.

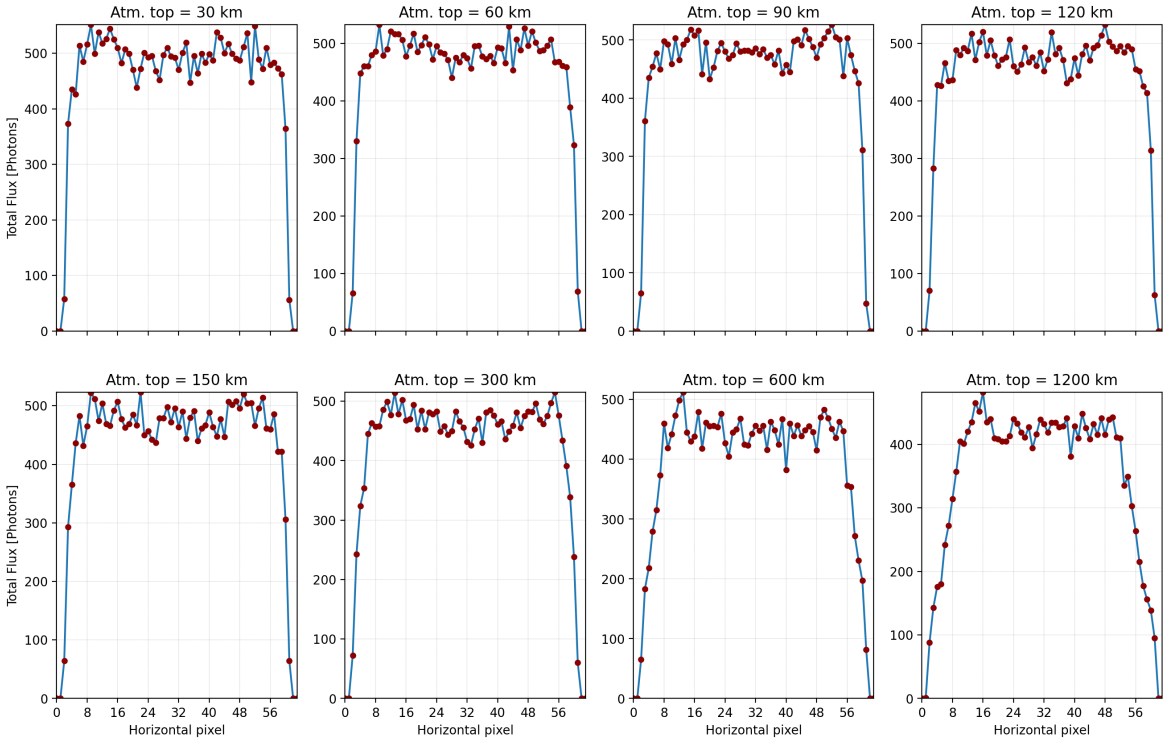

Figure 3.11: Graphs representing F values along the equator of the planets with different atmospheric thicknesses (mentioned in the title of every graph) for $\alpha = 0°$. The atmospheres consist of three layers with the layers having geometrical thicknesses of 1x, 2x, and 3x, where x = 5,10,15,20,25,50,100, and 200 km for atmospheres with total thicknesses of 30,60,90,120,150,300,600, and 1200 km, respectively. Three layers have $b^m_{\rm sca} = 1.0, 0.2, 0.1$ from bottom-most to the top-most layer. Graphs were produced using images of resolution of 64x64 pixels. To have a better S/N ratio we used three vertical pixel lines near the equator of planets.

Figure 3.12 shows Stokes parameters and P for planets with the atmospheric thicknesses of 30, 300, 600, and 1200 km for $\alpha = 90°$. From the figure it can be seen that the twilight zone is more broadened than for the corresponding atmosphere thicknesses in the case of a single layer atmosphere. This is because as the upper layers become more tenuous, more photons can travel longer paths in the atmosphere than for the single layer case. P looks similar to the corresponding single layer atmospheres (see Figure 3.5) for the major part of the disk, but it is increased on the limb owing to an increased percentage of flux from singly scattered photons. Similar to Figure 3.11 where we saw at what atmospheric thickness, effect of the sphericity becomes prominent at $\alpha = 0°$ for the atmospheres discussed in this subsection, Figure 3.13 shows variation in F across the equatorial region for planets with atmospheric thickness of 30,60,90,120,150,300,600, and 1200 km and having three layers. The thicknesses of layers are as mentioned in the caption of Figure 3.13. In the figure horizontal pixel number 32 represents the terminator. From F graphs, we see a thin twilight zone for the planet with an atmospheric thickness of 30 km. We can also see that the twilight zone has already prominently broadened for the atmospheric thickness as low as 60 km. Recall that for the atmospheres consisting of only one layer (discussed in subsection 3.1.1), we saw the prominent broadening of the twilight zone for the atmospheric thickness of 150 km, showing that at large phase angles as well the effect of sphericity of the atmosphere on the observed flux values depends on how much tenuous the (upper part of the) atmosphere is.

Figure 3.14 shows Stokes parameters and P for the planets with the atmospheric thicknesses of 30, 300, 600, and 1200 km for $\alpha = 180°$. Similar to $\alpha = 0°$ and 90°, we see the radial variation in transmitted flux for $\alpha = 180°$. This kind of stratification was observed for Pluto by New Horizons spacecraft for such a large phase angle and is shown in Figure 3.15.

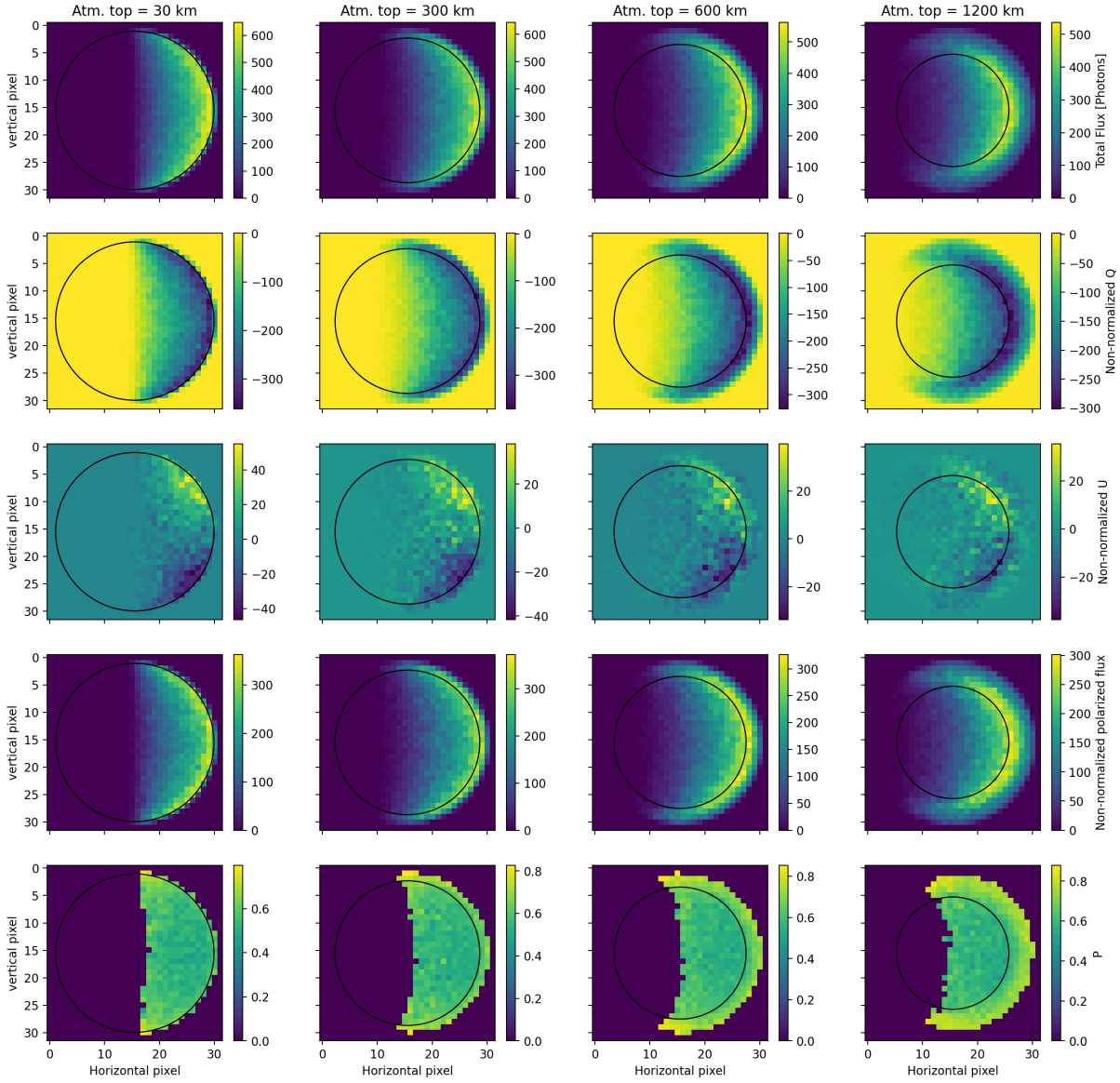

Figure 3.12: Same as Figure 3.9 but now for $\alpha = 90°$.

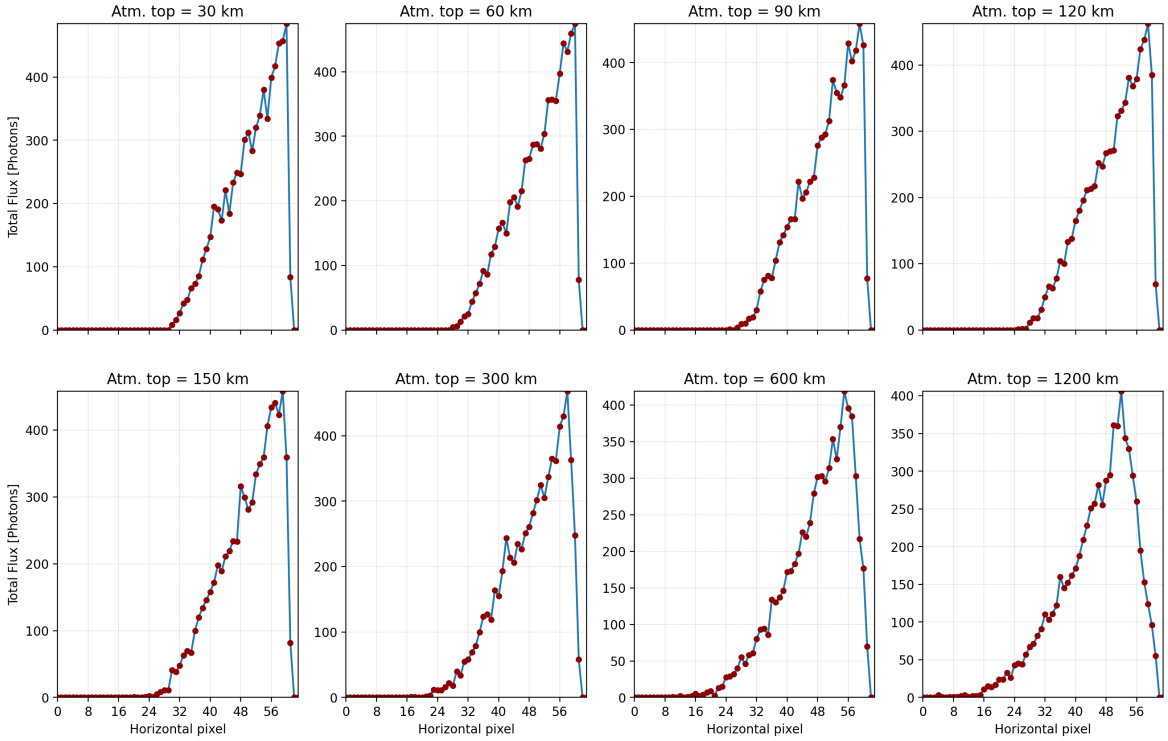

Figure 3.13: Graphs representing F values along the equator of the planets with different atmospheric thicknesses (mentioned in title of every graph) for $\alpha = 90°$. The atmospheres consist of three layers with the layers having geometrical thicknesses of 1x, 2x, and 3x, where x = 5,10,15,20,25,50,100, and 200 km for atmospheres with thicknesses of 30,60,90,120,150,300,600, and 1200 km, respectively. Three layers have $b_{\text{sca}}^{m} = 1.0, 0.2, 0.1$ from bottom-most to the top-most layer Graphs were produced using images of resolution of 64x64 pixels. To have a better S/N ratio we used three vertical pixel lines near the equator of planets.

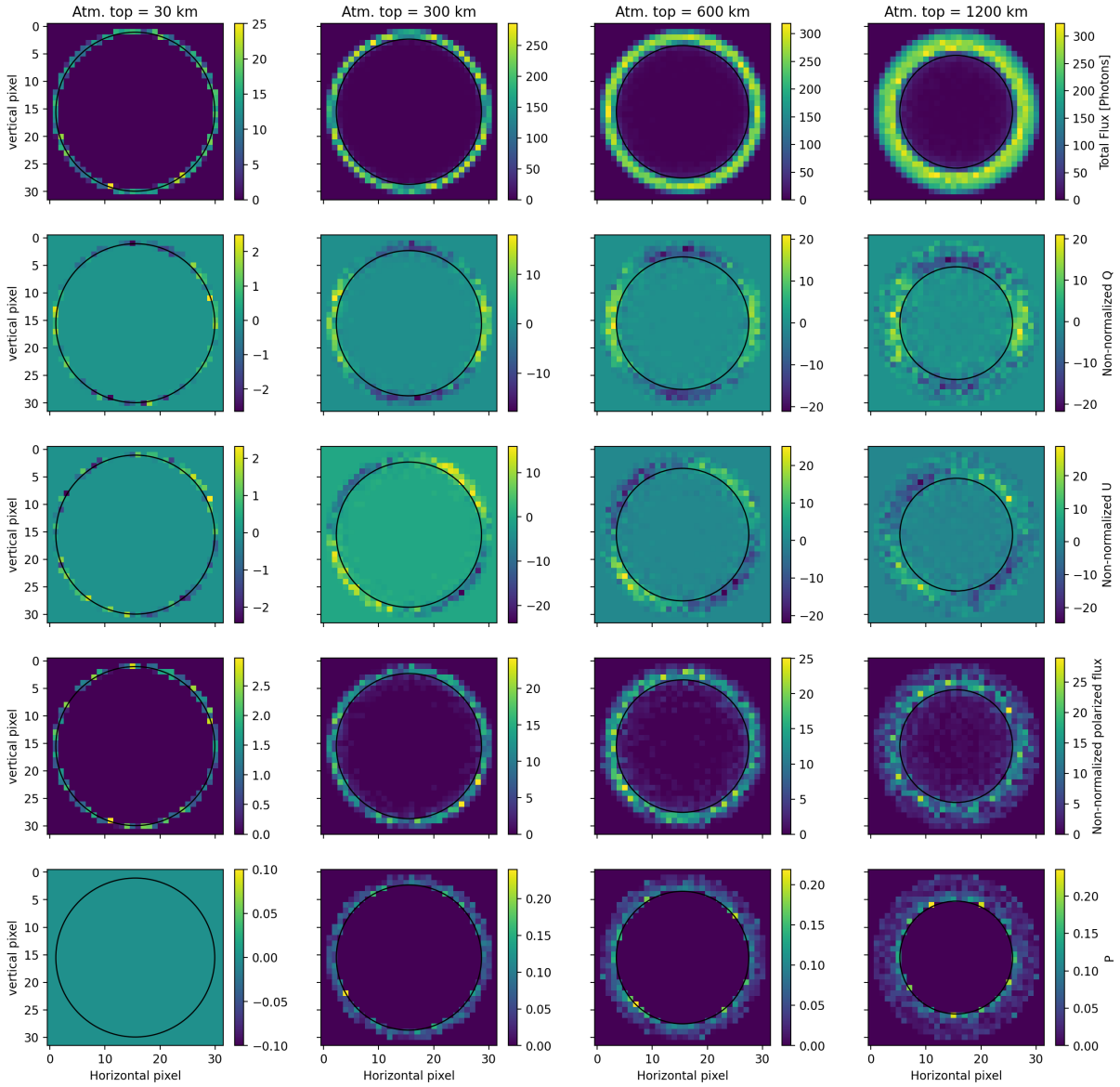

Figure 3.14: Same as Figure 3.9 but now for $\alpha = 180°$.

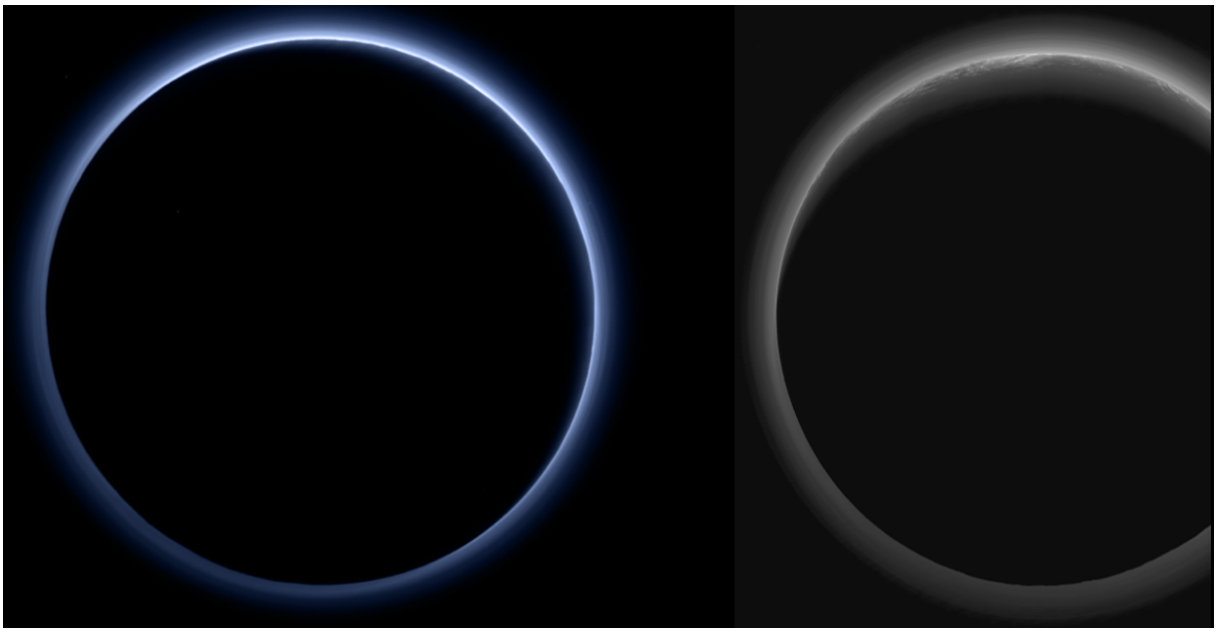

Figure 3.15: Left: picture of Pluto taken by New Horizons spacecraft's Ralph/Multispectral Visible Imaging Camera (MVIC) at a large phase angle. The back-lit blue coloured atmosphere is comprised of multiple layers of hazes. Right: another image of Pluto taken by New Horizons spacecraft at a large phase angle. Note that the original itself is cropped on the right side. More information on these pictures can be found here and here, respectively (credits for both the images: NASA/JHUAPL/SwRI).

3.2. Effect of the surface albedo

After investigating the effect of increasing geometrical thickness of the atmosphere, we analyzed the effect of the surface albedo (A_S) on the observed Stokes parameters and P of a planet with an extended atmosphere. For this analysis, an atmosphere with a total thickness of 600 km and consisting of 3 layers having thicknesses of 100, 200, and 300 km was used (from the discussion in Section 3.1, we saw that this setting represents an extended atmosphere). $b^m_{\rm sca}$ values of the layers were taken to be 1.0, 0.2, and 0.1 from the bottom-most to the top-most layer (same as in Section 3.1).

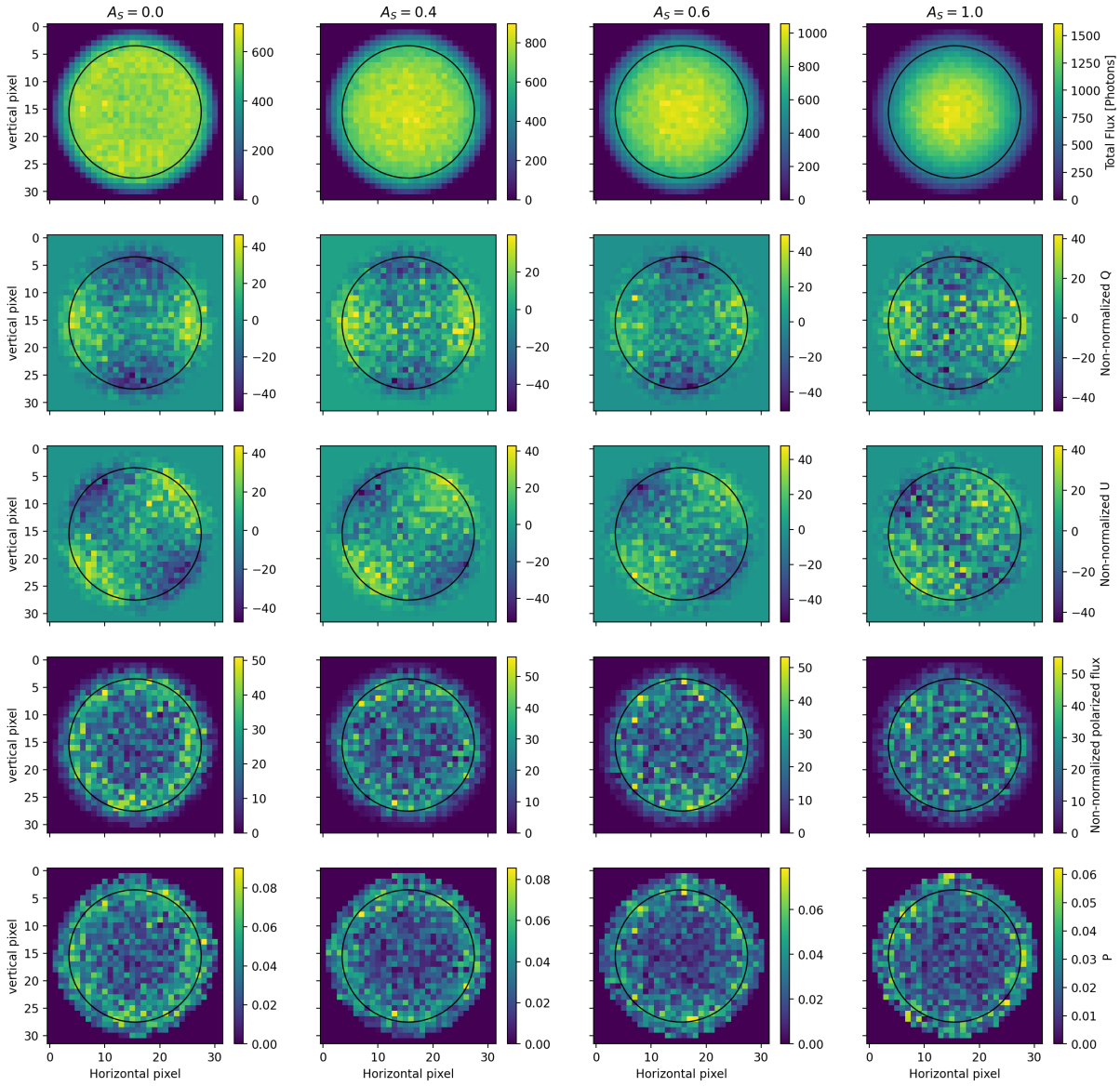

Figure 3.16: Disk resolved images at $\alpha = 0°$ for planets with variable surface albedo (mentioned in the title of every column) and a similar atmosphere consisting of three layers with geometrical thicknesses of 100, 200, and 300 km from the bottom-most to the top-most layer. First to last rows depict non-normalized F in photons, Q, U, total polarized flux ($\sqrt{Q^2+U^2}$), and P, respectively. The black circle represents the projection of the surface in the case of a rocky planet.

Figure 3.16 shows Stokes parameters and P at $\alpha = 0°$ for disk resolved planets with same atmospheric settings but different A_S. As A_S increases, we see that the central part of the disk becomes brighter than other parts as the photons in that region cover shorter distances and more of them are reflected by the surface. Q, U, and thus the total polarized flux values do not show much variation in the overall magnitudes. This is because we are using a Lambertian surface which completely depolarizes the light after reflection. Though the change

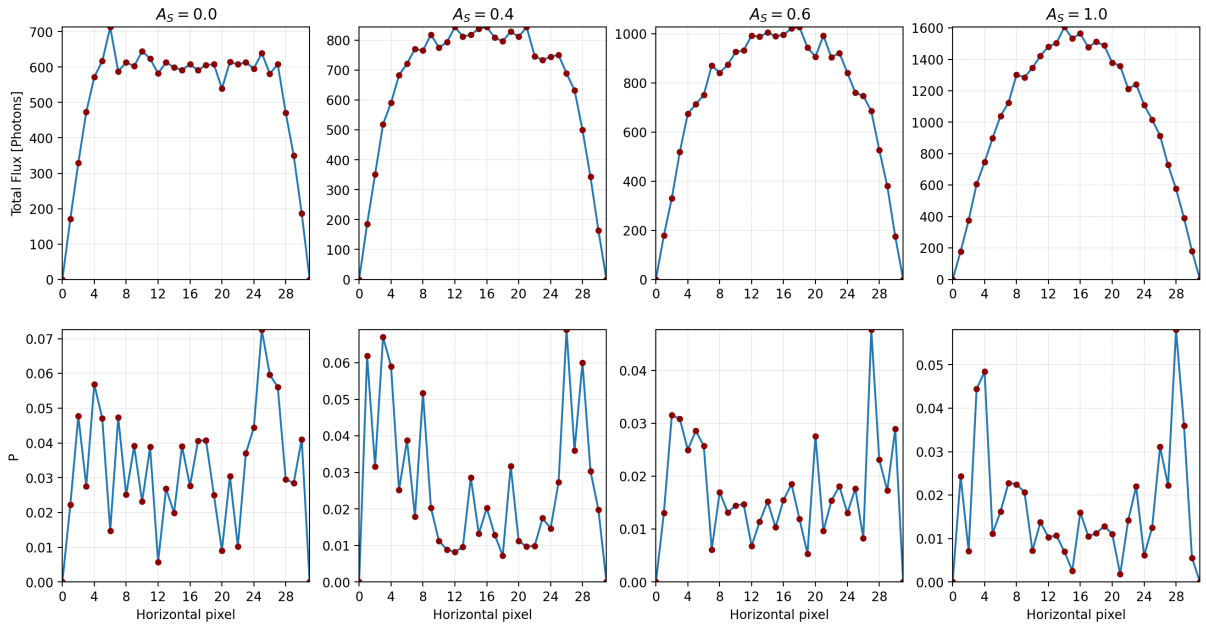

Figure 3.17: First and second rows representing F in photons and P, respectively for the pixels along the equator (vertical pixel number 15) in Figure 3.16.

in surface albedo does not affect the magnitude ranges of Q and U, it does affect their distribution over the resolved disk. It can be seen that Q, U, and thus total polarized flux patterns start to diminish with the increase in A_S. This is because apart from the photons that only scattered in the atmosphere and didn't reflect from the surface, we also see some of the photons that reflected from the surface, where they got depolarized, and then again got polarized in the atmosphere. And as the number of reflected photons increases with the increase in A_S, we see Q and U patterns (which are caused by photons that only scattered in the atmosphere) start to diminish. The area on the disk with higher P shrinks with increased A_S because of the more percentage of unpolarized or slightly polarized photons escaping the atmosphere while Q and U values remaining similar for all the A_S cases. Figure 3.17 shows the variation of F and P across the equatorial part of the disk for these planets with different A_S at $\alpha = 0°$. From F graph we can clearly see the brightening of planetary disk in the central part, while from the P graphs we see decrease in values of P with increase in A_S.

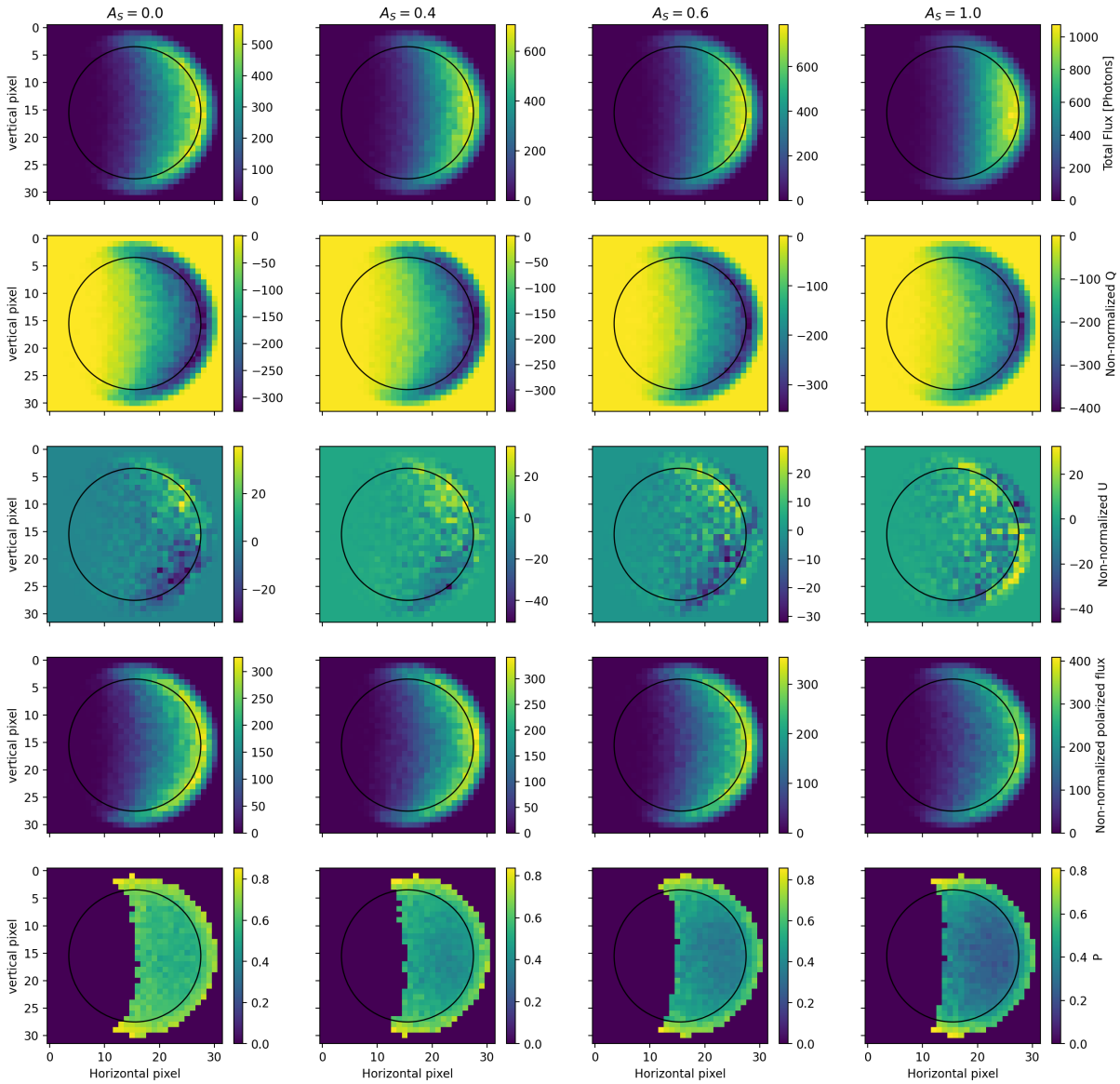

Figure 3.18: Same as Figure 3.16 but for $\alpha = 90°$

Figure 3.18 shows Stokes parameters and P at $\alpha = 90°$ for disk resolved planets with same atmospheric settings but different A_S. As can be seen from Figure 3.18, at $\alpha = 90°$ also, a similar distribution for F can be seen as that of for the $\alpha = 0°$. Q shows a similar pattern to F, while U becomes noisier. This is because Q has much higher values for this phase angle and while U has very low values and thus the noisiness in U is more apparent. As A_S increases, P decreases in most parts of the disk, including a prominent drop along the limb. Note that P doesn't seem to drop for the part of the limb near the terminator. This is because at these parts of the atmosphere, the percentage of reflected photons is less, or in other words, the surface has little direct influence on the number of photons emerging out of the atmosphere from these areas. The Stokes parameters and P look almost the same for planets with different A_S cases at $\alpha = 180°$ and thus are not shown here. They look very similar, because at this larger phase angle, A_S has very small influence on the emergent flux and remember that we are using the same atmosphere settings for all the planets.

3.3. Effect of the single scattering albedo

Another important factor influencing Stokes parameters and P of the planet's reflected light is the single scattering albedo ($\tilde{\omega}$) of the scatterers in the atmosphere. To investigate its effect, we chose the same atmosphere layer setting as in Section 3.2 i.e. they have geometrical thicknesses of 100, 200, and 300 km and b^m_{sca}= 1.0,0.2, and 0.1 from the bottom-most to the top-most layer. A_S was set to be 0, and we varied $\tilde{\omega}$. Stokes parameters and P for $\alpha = 0°$ are shown in Figure 3.19.

The first obvious thing to notice would be the decrease in total as well as polarized flux across all parts of the disk due to increased absorption as $\tilde{\omega}$ decreases. Q, U and thus the total polarized flux become noisy due to very low photon counts as $\tilde{\omega}$ decreases. P shows interesting behavior with the decrease in $\tilde{\omega}$. As $\tilde{\omega}$ represents the scattering probability, every time photon scatters, part of it (or the photon bundle) is absorbed, and we terminate the photon after a significant part of it is absorbed (so basically the photon is absorbed in the atmosphere). Now, as the photons near the limb or near the outer edges of the denser part of the atmosphere are generally scattered twice or thrice, more of them are absorbed as $\tilde{\omega}$ decreases. Recall that these are the photons that cause a higher degree of polarization around the limb. Thus, because the number of such photons is decreased, P in this area decreases with the decreasing $\tilde{\omega}$. Figure 3.20 shows the variation of F and P discussed above for the equatorial part of the disk at $\alpha = 0°$.

Figure 3.21 shows Stokes parameters and P for the planets having atmosphere with different $\tilde{\omega}$ at $\alpha = 90°$. Though the total and polarized fluxes show a similar behavior as for $\alpha = 0°$, P varies differently. With the increase in the percentage of singly scattered photons, P increases in most parts of the disk with decreasing $\tilde{\omega}$. In Figure 3.21 even after using the noise threshold of 0.2, the number of pixels falling within this threshold decreases with a decrease in $\tilde{\omega}$. At $\alpha = 180°$, similar variation in Stokes parameters and P as for $\alpha = 0°$ for the visible part of the disk can be seen and thus are not shown here.

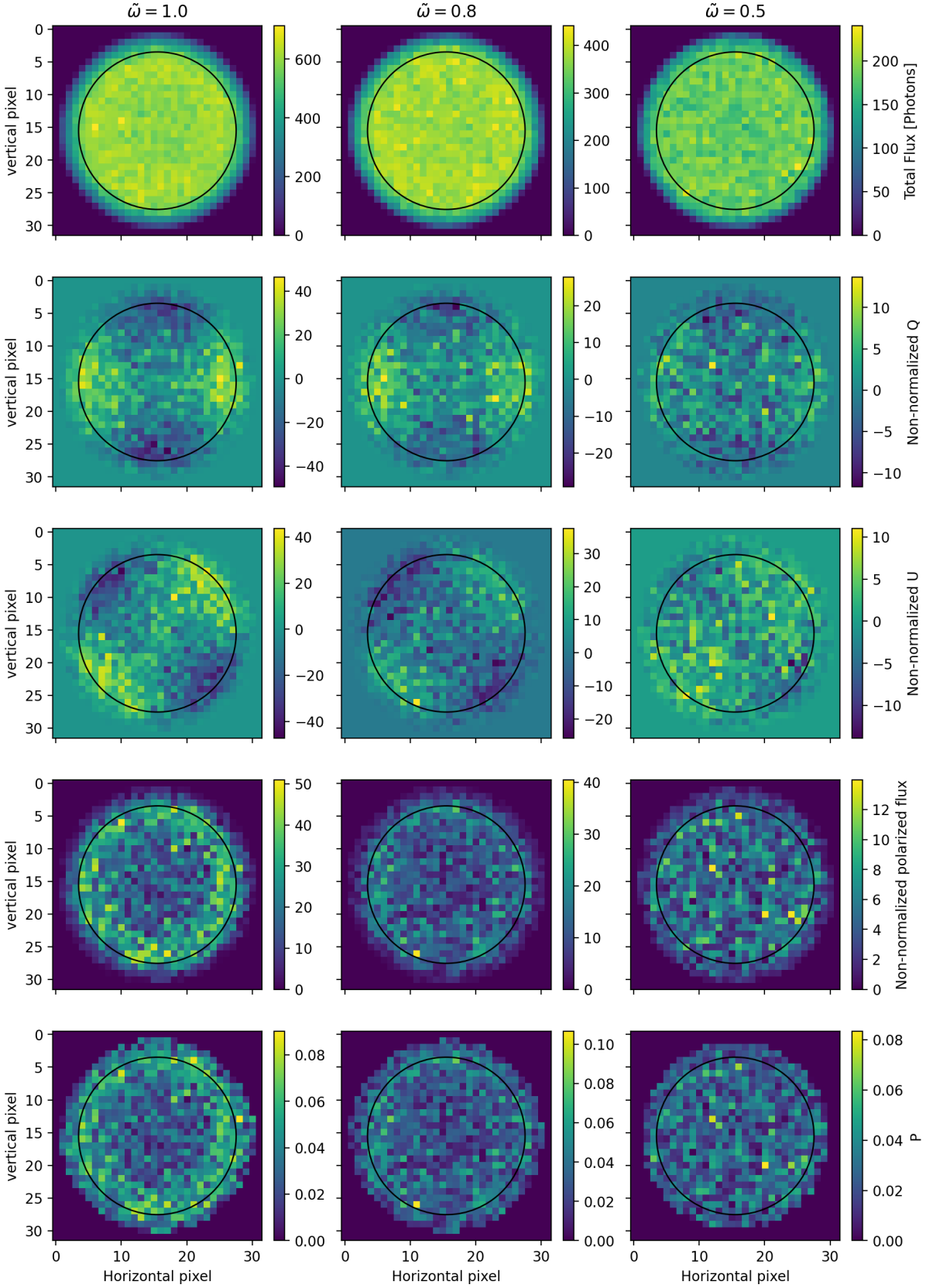

Figure 3.19: Same as Figure 3.16 but now $A_S = 0$ and $\tilde{\omega}$ is different (mentioned in the title of every column) for all planets.

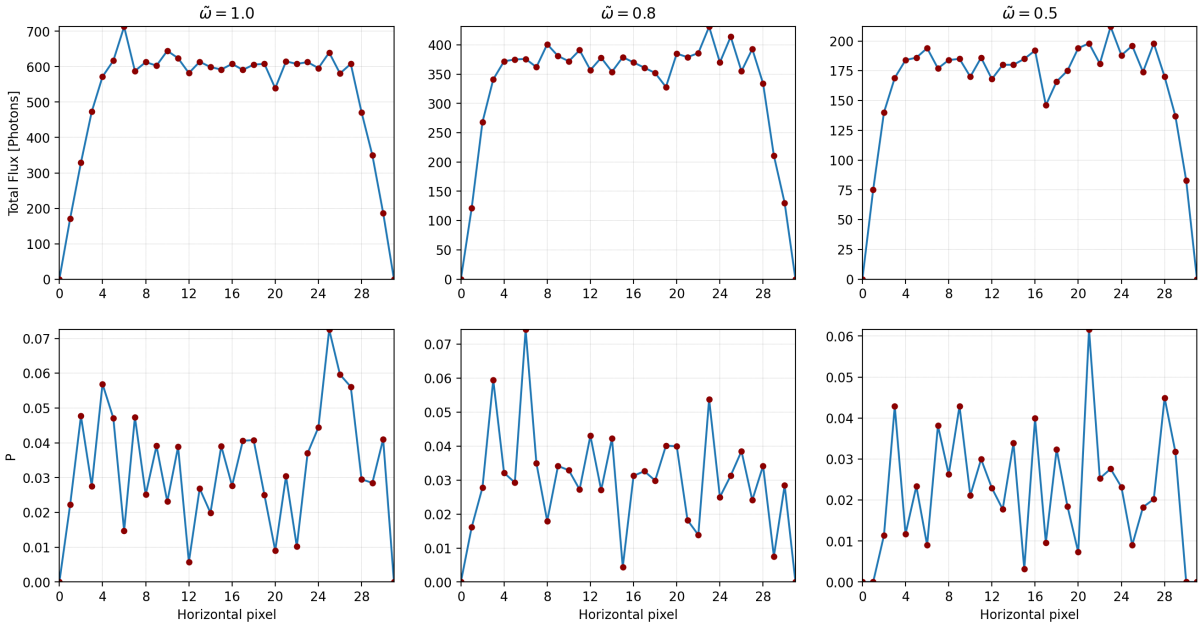

Figure 3.20: First and second rows representing F in photons and P, respectively for the pixels along the equator (vertical pixel number 15) in Figure 3.19.

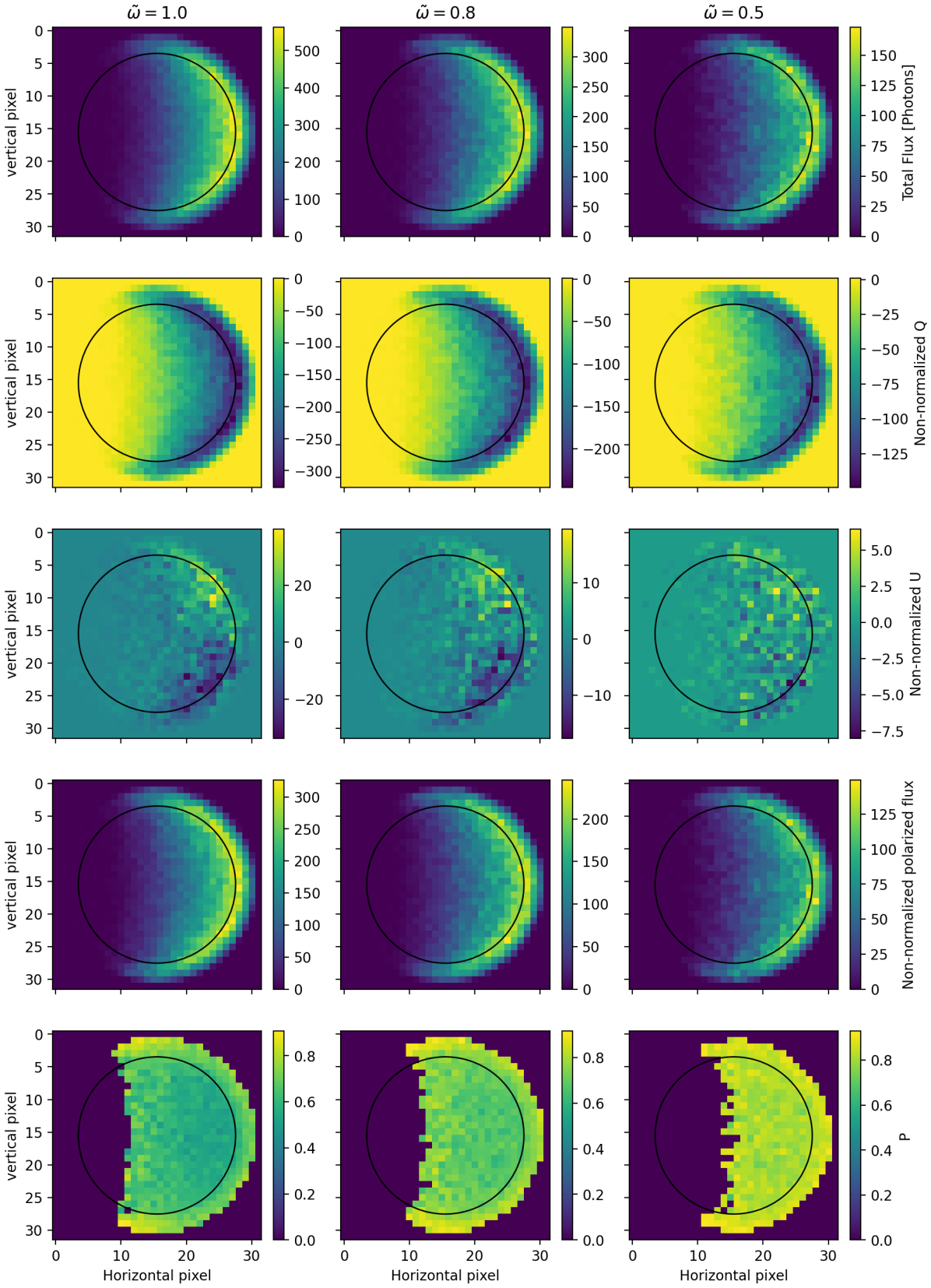

Figure 3.21: Same as Figure 3.19 but now for $\alpha = 90°$.

3.4. Titan's atmosphere

After investigating hypothetical extended atmospheres, we simulated polarimetric signals that can be observed from Titan (e.g. see Figure 1.1). Titan's atmosphere primarily consists of N_2 and CH_4 that cause the Rayleigh scattering. It contains a plethora of organic trace gases (a good review of those can be found in Hörst (2017)). An important constituent of Titan's atmosphere is its organic haze, which also gives it its peculiar orange colour. This haze strongly scatters the light and because of it, Titan's surface is difficult to observe at most of the wavelengths.

To construct Titan's atmosphere, we considered a total atmospheric geometrical thickness of 550 km and divided it into 13 layers; Table 3.2 depicts the values of different parameters. We took the pressure profile from Fulchignoni et al. (2005). We considered the Rayleigh scattering only by N_2 and CH_4 and ignore other trace gases. We find this as a good approximation for molecular scattering in Titan's atmosphere because mole fractions of other species are very small. The CH_4 mole fractions were taken from Niemann et al. (2010). For N_2 and CH_4, the refractive indices (n_r) were obtained using dispersion formulas given in Bates (1984) and He et al. (2020), respectively. Wavelength independent values of δ were taken as ≈ 0.02 for N_2 (Bates, 1984) and 0.0 for CH_4 (He et al., 2020). Considering these values, we calculated b^m_{sca} for every layer using Equation 2.8. Sylvestre et al. (2019) observed Titan in August 2018 using several polarimetric filters of the SPHERE facility including the N_R filter mentioned in Figure 1.1. Though these observations are not processed yet, they will be processed in future and can be used to study Titan's atmospheric haze. Methane strongly absorbs light for many wavelength bands in the visible and IR region but it has a weak absorption for the wavelength band of the N_R filter of SPHERE (and almost no absorption at its central wavelength at 646 nm). Also N_2 has negligible absorption in the visible and infrared wavelengths. As we have not yet included the code for the molecular absorption calculations in SPORT, we chose to do the computations for 646 nm wavelength and thus we ignore the molecular absorption (i.e. $b^m_{\text{abs}} = 0$) in this research.

Layer	Bottom Alt. [Km]	Bottom P [Pa]	N_2 %	CH_4 %	b^m_{sca}	b^a	Aerosol $\tilde{\omega}$	b^a_{sca}	b^a_{abs}
1	0	146700	95.25	4.75	0.2645	0.4410	0.9875	0.4355	5.511E-3
2	11.3	82740	96.99	3.01	0.1423	0.3864	0.9875	0.3816	4.828E-3
3	21.2	47700	98.2	1.8	0.1471	0.9133	0.9875	0.9019	1.141E-2
4	44.6	11280	98.52	1.48	4.278E-2	1.7852	0.9815	1.7523	3.290E-2
5	100	951	98.52	1.48	3.002E-3	1.2274	0.9607	1.17932	4.813E-2
6	150	254.17	98.52	1.48	7.845E-4	0.6229	0.9310	0.5799	4.291E-2
7	200	78.62	98.52	1.48	2.365E-4	0.2433	0.9162	0.2229	2.037E-2
8	250	27.58	98.52	1.48	8.409E-5	8.508E-2	0.9162	7.796E-2	7.125E-3
9	300	10.06	98.52	1.48	3.136E-5	2.858E-2	0.9162	2.619E-2	2.394E-3
10	350	3.75	98.52	1.48	1.214E-5	9.475E-3	0.9162	8.681E-3	7.934E-4
11	400	1.39	98.52	1.48	4.787E-6	3.126E-3	0.9162	2.864E-3	2.617E-4
12	450	0.49	98.52	1.48	1.755E-6	1.029E-3	0.9162	9.436E-4	8.624E-5
13	500	0.1708	98.52	1.48	5.787E-7	3.391E-4	0.9162	3.107E-4	2.839E-5
Top	550	0.0689							

Table 3.2: Table depicting values of atmospheric parameters used to construct Titan's atmosphere (model H550) in this research. For the top of each layer we used the bottom of the upper layer. Note that N_2 % + CH_4 % = 100 %. b^a designates the total aerosol optical thickness for a particular layer.

The haze optical thickness and single scattering albedo profiles were taken from Doose et al. (2016). Titan's haze particles are of type fractal aggregates (Rages and Pollack, 1983, Tomasko, 1980, West et al., 1983). Doose et al. (2016) provided the recent constraints on their properties. The scattering matrix of fractal aggregate particles can be calculated by the T-matrix method (Waterman (1971)). Mishchenko et al. (1996) and Mishchenko et al. (2000) described this method in detail and also provided publicly available T-matrix codes. However, the T-matrix method is computationally very intensive and it would be very time consuming to obtain the scattering matrix of fractal aggregate particles described in Tomasko et al. (2008), the precursor paper of Doose et al. (2016) using this method, because they used the aggregate particles having 3000 monomers to constrain observations by Descent Imager/Spectral Radiometer (DISR) instrument on-board the Huygens probe, and

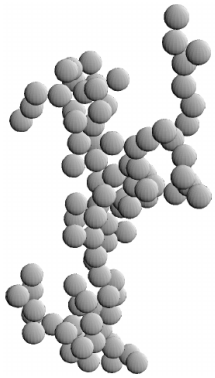

Figure 3.22: Aggregate haze particle that we used in Titan's atmosphere.

the time taken to calculate scattering matrix of an aggregate particle by T-matrix method increases with increase in the number of monomers which coagulate and form the aggregate particle. Though Tomasko et al. (2008) provide the values of phase functions of Titan's haze particles at multiple wavelengths, they do not provide other elements of the scattering matrix. Although they have described the algorithm to calculate those using the parameterization method they developed, it would have been time-consuming to implement and test it. Thus, we decided to use the haze scattering matrix of the particles described in Karalidi et al. (2013). This matrix was already available and the particles roughly resemble Titan's fractal aggregate haze particles. To first generate the fractal aggregate particles, they used the cluster-cluster aggregation (CCA) method that starts with sequentially adding spheres from random directions to the existing cluster till it has a certain size and then these clusters are combined to form the resultant aggregate particle of the desired size. Here, the small spherical particles are called monomers. The haze particle that we used consists of 94 monomers, with each monomer having an approximate radius of 0.035 μm. The resultant aggregate particle has a volume-equivalent-sphere radius of 0.16 μm. They calculated the single scattering matrix of this particle using the T-matrix method combined with the superposition theorem (Mackowski and Mishchenko, 2011). More details of the particle can be found in Karalidi et al. (2013). Figure 3.22 shows a sample fractal particle and Figure 3.1 shows the single scattering matrix elements of these particles for $\lambda = 646$ nm. Finally, we considered the surface to be Lambertian and considered $A_S = 0.2$ (Brossier et al., 2018).

We did simulations for the following three atmosphere models

- purely molecular till 550 km (model M550)
- molecules + haze till 350 km and then purely molecular till 550 km (model H350)
- molecules + haze till 550 km (model H550)

Note that we kept the same total haze optical depth in the model H350 as in the model H550 by adding the haze optical thicknesses from layers above 350 km to the layers below 350 km. We chose such kind of settings for the haze because Titan is known to have a detached haze layer that varies seasonally between the altitudes of 350 km to 500 km. It undergoes a cycle of construction and destruction as the season changes on Titan. It was observed to be completely disappeared near the equinox and then appeared at higher altitudes of about 500 km when the spring-summer began in one of the hemispheres and then it subsequently moved to the lower altitudes (Seignovert et al., 2021). Thus models H350 and H550 can very roughly simulate Titan's atmosphere during such periods in Titan's year. But it is important to mention that Titan's detached haze layer evolves in a much complex way than it was thought earlier (Seignovert et al., 2021).

Figure 3.23 shows the disk resolved images of Stokes parameters and P for these three models. It can be seen that F is almost uniform for model M550 except near the limb, while it decreases with the addition of haze. This is because the haze particles strongly scatter the light in a forward direction (see Figure 3.1). Thus, as b^a increases, the amount of light scattered in the backward direction decreases. For models H350 and H550, we see that the disk is brighter in the middle part and the brightness decreases towards the limb. This is because photons in the central part of the disk need to travel a shorter distance than in the other parts and thus, they

undergo less scatterings, and thus have smaller probability of scattering by the haze particles. Looking at Table 3.2 it can be seen that the scattering in Titan's atmosphere is dominated by haze particles due to higher b^a_{sca} than b^m_{sca}. Another reason for decreased flux is $\tilde{\omega}$ of haze particles; it is not 1, which means there is an absorption by haze particles. It can also be seen that the limb of Titan looks expanded when the haze is present in the atmosphere, due to larger scattering combined with the sphericity of the atmosphere.

Polarized fluxes (Q and U) decrease with the increase in the haze. This is because haze causes less polarization of light than molecules (see Figure 2.6). Also, Q and U patterns become noisy because of the lower amount of light scattered back toward smaller phase angles (0° in this case) and thus leading to lower Q and U values. P in the area around the limb decreases in models H350 and H550, owing to the reduced second-order scattering by molecules. Figure 3.24 shows the variation of F and P discussed in above paragraphs for the equatorial part of the disk for models M550, H350, and H550 at $\alpha = 0°$.

Figure 3.25 shows Stokes parameters and P of Titan for these three atmosphere models for $\alpha = 90°$. It can be seen that the twilight zone is more broadened when the haze is present in the atmosphere. Polarized fluxes (Q and U), and thus the total polarized flux show smaller values for H350 and H550 model atmospheres than the M550 atmosphere. This is because we see the photons scattered by molecules as well as haze particles and the haze particles cause lower polarization than molecules at $\theta \approx 90°$. Figure 3.26 shows the above discussed variations of F and P across the equatorial part of the disk for these model atmospheres at $\alpha = 90°$.

Finally, Stokes parameters and P for $\alpha = 180°$ are shown in Figure 3.27. Looking at the total flux, it can be seen that Titan is extremely bright at this larger phase angle for model H350 and H550 atmospheres than for the model M550 atmosphere! This is again due to the strong forward scattering by haze particles. Also, F at this phase angle is higher for H550 than H350. Note that we used the resolution of 64x64 pixels for these images to have a clearer idea of the region of the atmosphere contributing the most to F. From Table 3.2, it can be seen that b^a_{sca} still has higher values in the upper atmosphere and thus leading to strong scattering by haze in this region as well. If we look carefully, it can be seen that the highest flux comes from the upper part of the visible atmosphere of Titan (this is the area having lower flux for $\alpha = 0°$), indicating that apart from the strong forward scattering of the haze, this is also the effect enhanced by Titan's extended atmosphere and thus due to increased role of the sphericity of the atmosphere. As both molecules and haze particles cause very low polarization at $\theta \approx 0°$, we see lower values of Q, U, and P.

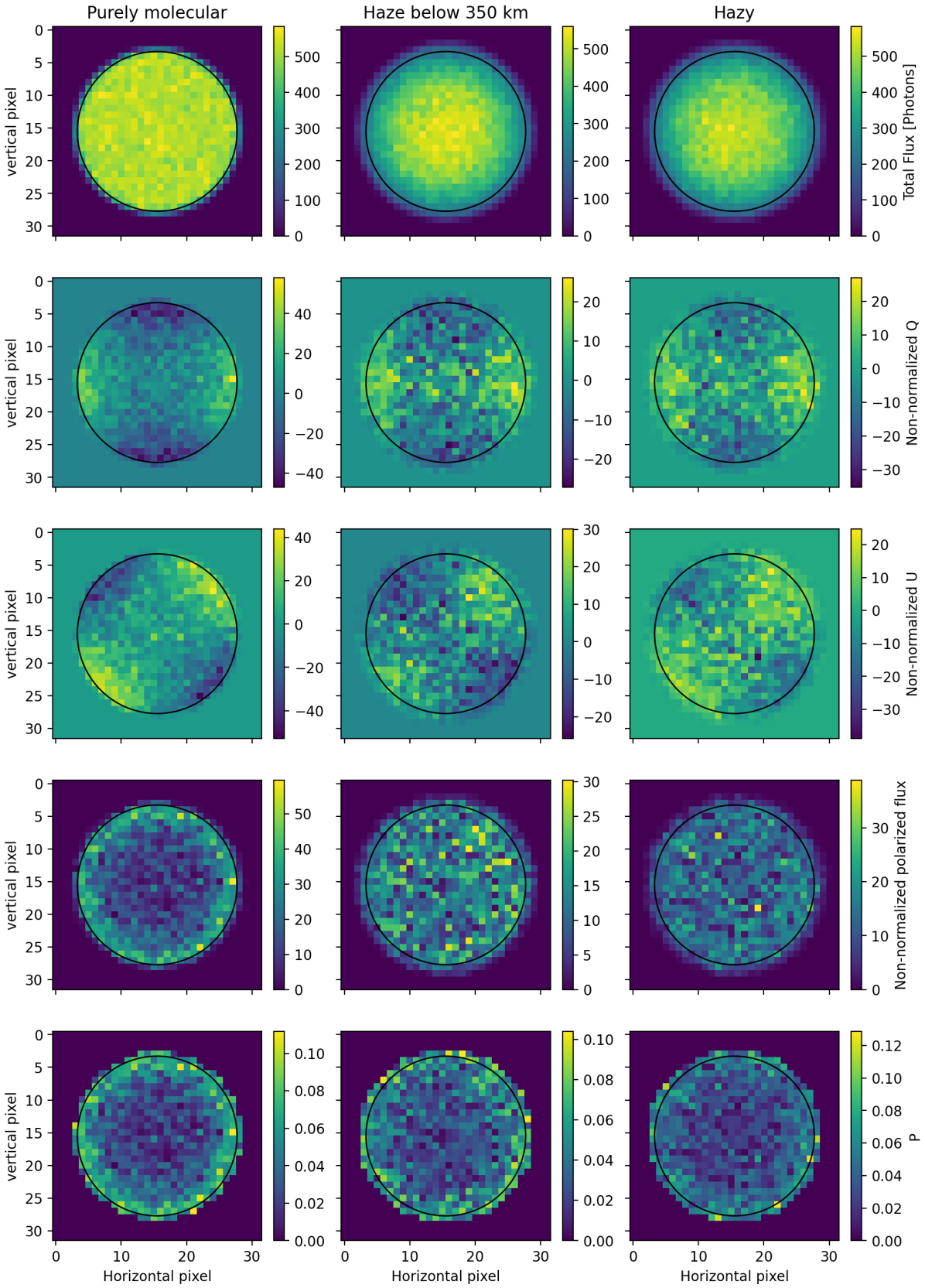

Figure 3.23: Disk resolved images of Stokes parameters and P of Titan for three atmosphere models, M550 (purely molecular), H350 (haze below 350 km), and H550 (hazy), at $\alpha = 0°$. The atmosphere parameters are depicted in Table 3.2

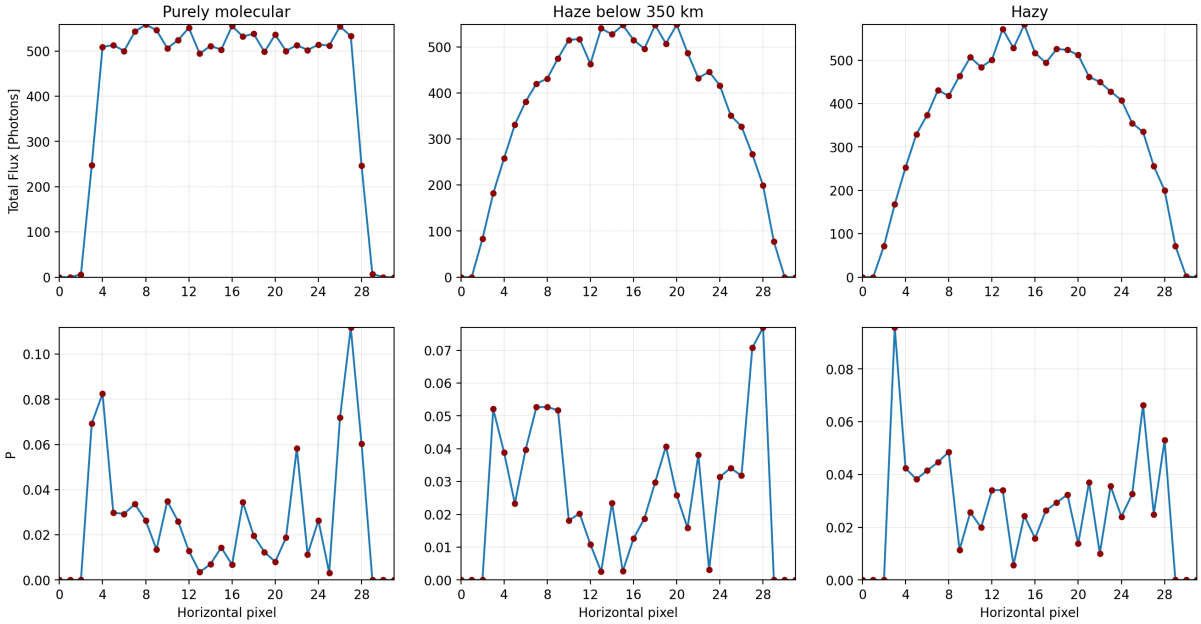

Figure 3.24: First and second rows representing total flux in photons and P, respectively for the pixels along the equator (vertical pixel number 15) in Figure 3.23.

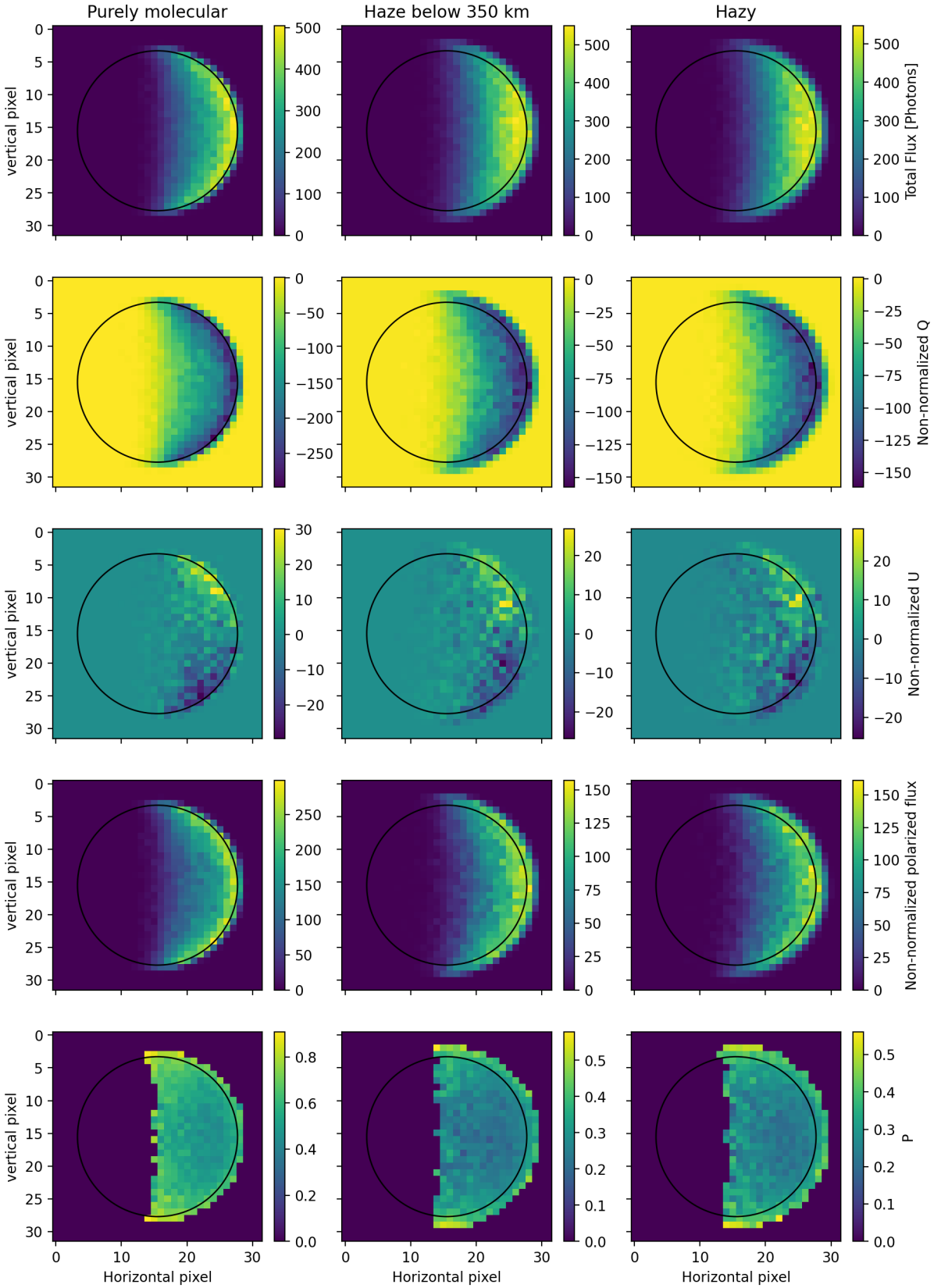

Figure 3.25: Same as Figure 3.23, but for $\alpha = 90°$.

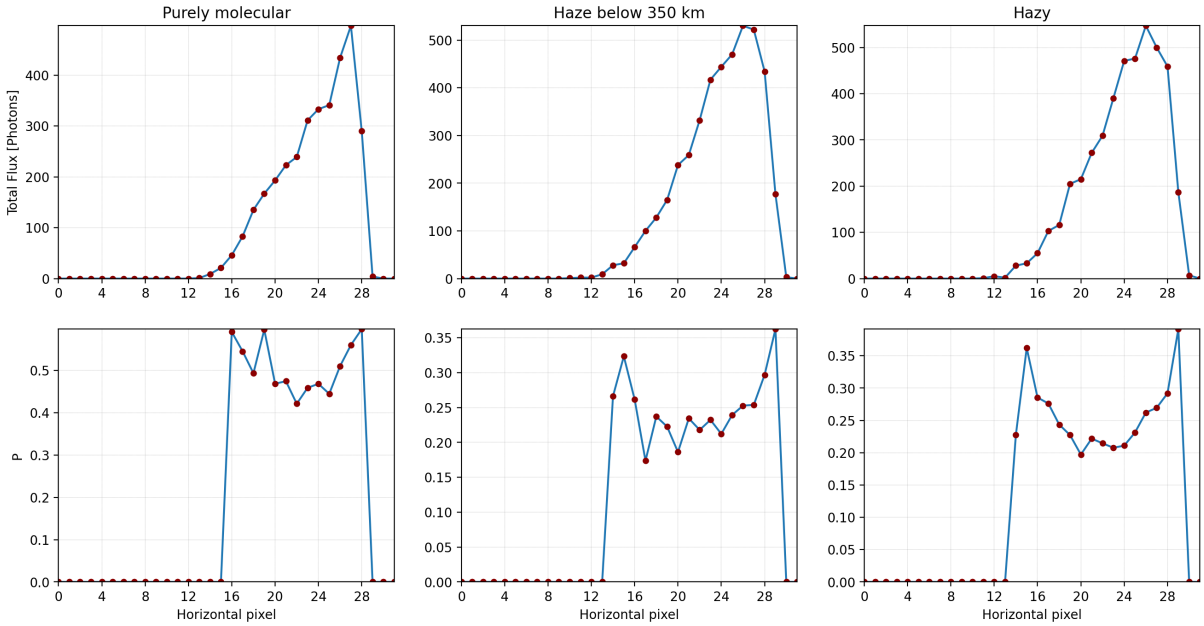

Figure 3.26: Same as Figure 3.24, but for $\alpha = 90°$

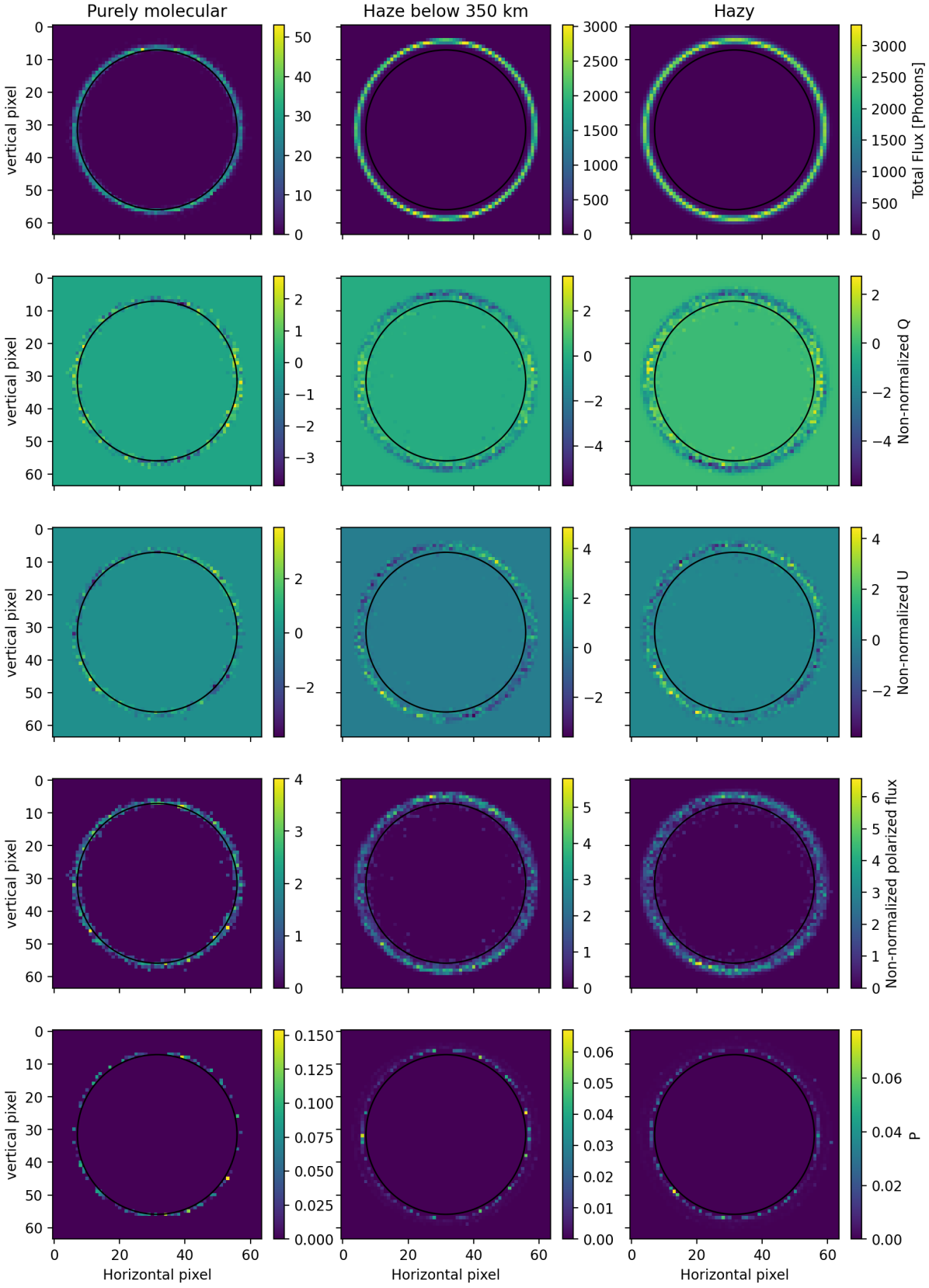

Figure 3.27: Same as Figure 3.23, but for $\alpha = 180°$.

4

Results: Spatially Unresolved Planets

Though disk resolved images of the solar system planets/moons are already available, they are very difficult to be (or will not be) available for exoplanets. Nevertheless, in the near future, we will be able to obtain spatially unresolved observations of the reflected star light from exoplanets. Thus, it is crucial to investigate how the disk integrated total flux and polarization signals of planets with extended atmospheres vary with the phase angle (i.e. phase curves). In this Chapter, we discuss the disk integrated total flux and polarimetric phase curves for the model planets discussed in Chapter 3.

4.1. Effect of the geometrical thickness of the atmosphere

In Figure 2.6, we compared the phase curves generated using SPORT with those from the model using the adding-doubling method that assumes the plane-parallel atmosphere. For these comparisons, a geometrically very thin atmosphere with a total thickness of 6 km was used in SPORT simulations. This setting closely simulates the plane-parallel atmosphere geometry as the effect of the sphericity of the atmosphere is low due to a very small extent of the atmosphere. To investigate how the phase curves of planets change with the increasing atmospheric thickness, in this section, we will discuss phase curves for the planets with increasing atmospheric thickness for the following cases:

- atmospheres consisting of single homogeneous layer (hereafter, first case)
- atmospheres consisting of multiple layers, where layers have the same geometrical thickness (hereafter, second case)
- atmospheres consisting of multiple layers, where layers have different geometrical thicknesses (hereafter, third case)

4.1.1. Atmospheres consisting of single homogeneous layer

Recall that for the first case, described in Section 3.1, we considered the atmosphere consisting of single homogeneous layer. We considered b^m_{sca} of the layer to be 1.3. We used a planet with a radius of 2575 km and the surface albedo was set 0. In Section 3.1 we considered atmospheric thicknesses of 30, 300, 600, and 1200 km. Phase curves for planets having these atmospheric thicknesses and an additional atmospheric thickness of 900 km are shown in Figure 4.1. Top-left panel in this figure shows phase curves of normalized total flux (hereupon, F). We normalized F such that at $\alpha = 0°$ F represents geometric albedo (A_G) of the planet. Recall from Section 2.4 that geometrical albedo of a planet is the ratio of the brightness of the planet/moon at $\alpha = 0°$ to the brightness of the Lambertian disk of same radius illuminated with the same amount of irradiance. To obtain A_G for a planet with a particular atmospheric thickness, we used a Lambertian disk having radius equal to 2575 + total atmosphere thickness. From F curves in Figure 4.1 we see that A_G decreases as the atmospheric extent increases. Let us recall from Eq. 2.16 that the extinction cross-section, k_{ext} is nothing but b/l, where b and l are the layer optical and geometrical thicknesses, respectively. When the l of the layer increases while the b is same, k_{ext} decreases and the layer becomes more tenuous. Also, recall that the photon mean free path is the reciprocal of k_{ext}. This means, with increasing l for the same b of the layer, photons will have longer mean free paths and thus they travel longer distances in the atmosphere before having an interaction. Table 4.1 shows the values of k_{ext} for different layers thicknesses . Smaller k_{ext} values with increasing atmospheric extent led to two effects. First, more photons passed through the atmosphere without

any interaction. Because with smaller k_{ext} photons had larger probabilistic distances and for some photons this distance exceeded the distance to the atmosphere boundary along their path, and thus they escaped the atmosphere without any interaction. It was observed that for the atmosphere with a total thickness of 30 km, a negligible percentage of the total incoming photons didn't interact in the atmosphere while for the extreme case of 1200 km, around 3% photons didn't interact in the atmosphere. Second, as more photons traveled longer distances, they contributed to the flux from the larger phase angles. Because of these two effects, we see lower flux at smaller phase angles and thus a drop in A_G with increasing atmospheric thickness. From F curves, it can be seen that F has larger values for a particular higher phase angle with increasing atmospheric extent. This is due to more broadened twilight zone (result of the second effect mentioned above). This light from the twilight zone is not considered in the calculations from the adding-doubling method and thus F curves show huge deviations from the one generated using the adding-doubling method as the atmosphere gets extended. Phase function (hereafter, $\varphi(\alpha)$) curves show how F varies with phase angle with respect to F at $\alpha = 0°$.

l [km]	k_{ext} (for b=1.3)
30	0.43
300	4.33E-3
600	2.16E-3
900	1.44E-3
1200	1.083E-3

Table 4.1: Table depicting values of k_{ext} for an atmosphere consisting of only one layer (Atmosphere total thickness = l).

As we are using a (horizontally) homogeneous atmosphere, U shows symmetry and has opposite signs in the north and south hemispheres (see Figures 3.2, 3.5, and 3.8) of the planet for all the phase angles. Due to this, when we integrate U over the entire disk it has a value equal to 0 (although in the Monte Carlo computations it is generally not exactly equal to 0, but it is negligible). This is the reason, we present the phase curves of only Q for the polarized flux in this chapter. When we integrate Q over the planetary disk, the locations on the disk having opposite polarization cancel each other out. When there is a symmetry in such locations, the net Q integrated over the disk will be 0 (almost 0 in Monte Carlo simulations). There is a symmetry of such locations when there is a uniform illumination over the entire disk of the planet i.e. at $\alpha = 0°$ and $\alpha = 180°$ and thus Q integrated over the disk for these phase angles will be 0. At other phase angles as there is no exact symmetry for such locations having opposite Q values, the disk integrated Q will have non-zero values.

Looking at Q in Figure 4.1 we see that longward of around $\alpha = 40°$, Q shows higher values as the atmospheric extent increases. This is because of more overall flux due to broadened twilight zone at these phase angles for the extended atmospheres as compared to thinner atmospheres. It can be seen that Q phase curves start to converge with increase in atmospheric thickness. We expect that they will converge at a certain threshold atmospheric thickness and after that thickness Q will have lower values. This is because after this threshold thickness, the atmosphere starts to become tenuous at such an extent that significant number of photons will pass through the atmosphere without any interaction, leading to overall less scattering in the atmosphere and thus ultimately less overall flux emerging out of the atmosphere for all phase angles. It can be seen that P curves are symmetrical around $\alpha \approx 90°$. It is because in these model atmospheres only molecular (Rayleigh) scattering is considered. If we capture photons that were scattered only once by gas molecules we will see P to be perfectly symmetrical around $\alpha = 90°$ (see Figure 2.6). But in reality we see a mixture of photons that scattered single as well as multiple times in the emergent flux. And a light scattered multiple times will not have P that is symmetrical exactly around $\alpha = 90°$. Although still for these model atmospheres as the percentage of photons that scattered less times (< 4 times) is higher in the emergent flux, we see Q curves symmetrical close to $\alpha = 90°$. Interestingly, P curves overlap and are indistinguishable for all the atmospheres till $\alpha \approx 140°$ in this case. This is because all the model atmospheres are composed of one homogeneous layer resulting in a similar mixture of number of times the photons scattered in the emergent flux (this will be more clear in the next subsection). Longward of $\alpha \approx 140°$ P curves diverge for larger atmospheric thicknesses. This effect has to do with the balance between singly scattered light with very low polarisation and second order scattered light, with higher, negative polarisation near the polar regions of the planet. With the plane-parallel

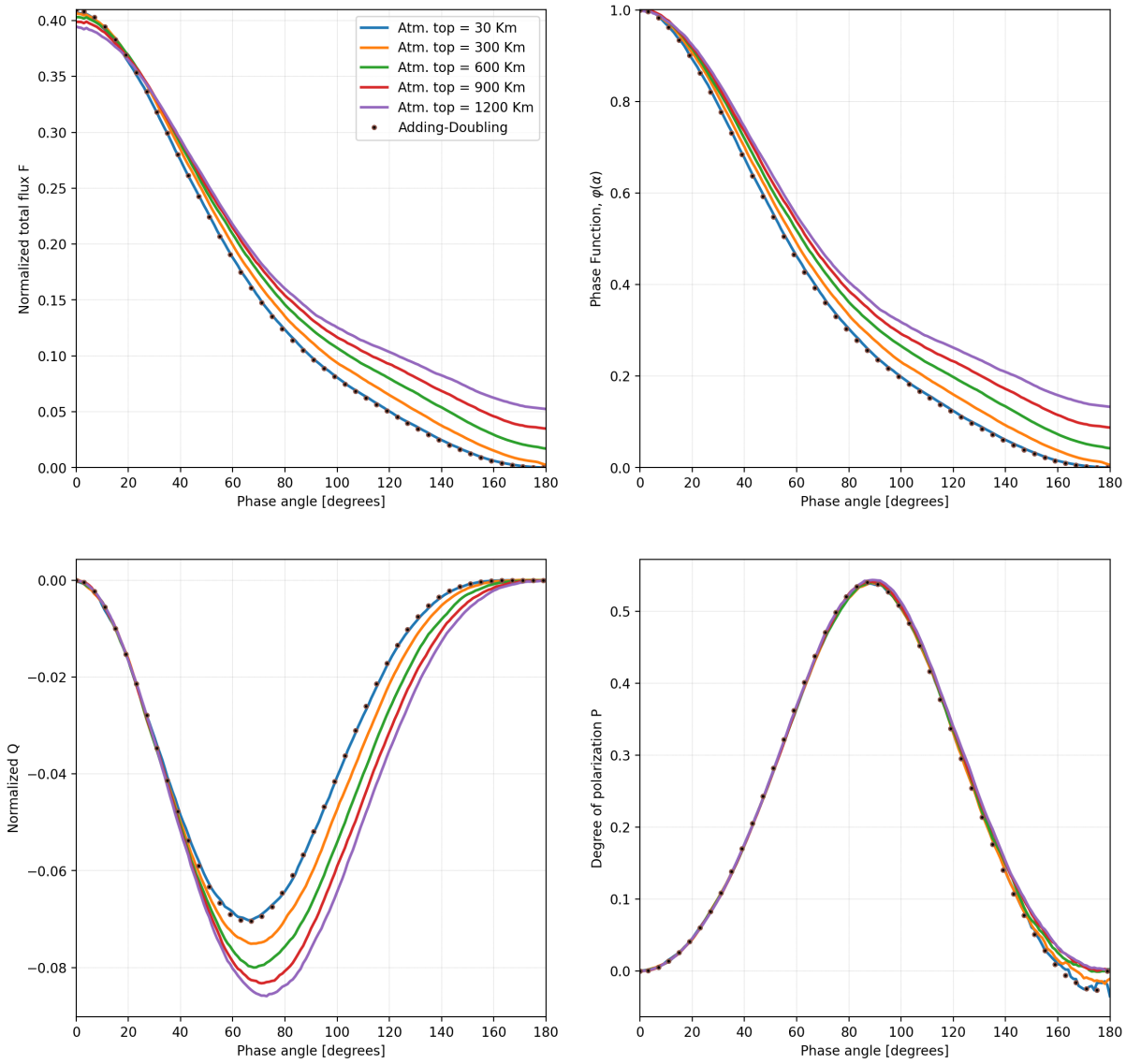

Figure 4.1: Top-left: Reflected planetary total flux (F) phase curves, normalized such that at $\alpha = 0°$, F represents the geometric albedo of the planet. Top-right: Phase function of the planet. Bottom-left: Q, normalized using the same factor that was used for the normalization of F. Bottom-Right: The degree of polarization, $P(-Q/F)$. Every model atmosphere consists of single homogeneous layer.

approximation, the equatorial region is dominated by singly scattered light, while the two polar regions are dominated by the second order scattered light. As this light is polarised parallel to the equatorial plane, it has negative sign. Because the equatorial region causes $P \approx 0$ and it is dark when the sun is below the horizon, P is negative at large phase angles, approaching zero as the singly scattered light takes over the polar regions at the largest phase angles. With the spherical atmosphere, the single scattering remains important at all phase angles, as the light is filtered through the twilight zone, and thus prevents P from becoming negative. Instead P just decreases towards zero.

4.1.2. Atmospheres consisting of multiple layers, where layers have the same geometrical thickness

In the next step, we modeled the planets having an atmosphere that is comprised of multiple layers. We divided the atmosphere into three layers having the same geometrical thickness while making $b^m_{\text{sca}} = 1.0, 0.2, 0.1$ from the bottom-most to the top-most layer. Thicknesses of the layers are as shown in the first column of Table 4.2. The surface albedo was again taken to be 0. Note that we did not present disk resolved images of this (second) case in Section 3.1, because we presented the third case and for disk resolved images the con-

clusions for both the cases are similar in qualitative manner. Phase curves for the second case are shown in Figure 4.2. Here, we see larger drops in F for smaller phase angles with the increase in the atmospheric extent as compared to the first case. Table 4.2 shows the values of k_{ext} for different layer thicknesses. In this case, more photons passed through the atmosphere without any interaction with the increase in the atmospheric extent than in the first case. This primarily occurred in the last two layers (i.e. layer 2 and 3). It was observed that for the atmosphere with a total thickness of 30 km, around 0.2% of the total incoming photons didn't interact in the atmosphere while for the extreme case of 1200 km, around as high as 16% photons didn't interact in the atmosphere. This led to overall much less scattering in the atmosphere than in the first case with the increased atmospheric extent. Apart from this, as the upper two layers are more tenuous than the one layer in the first case for the similar total atmospheric thickness, photons traveled longer distances in the atmosphere in this case than in the first case. In the second case, F has lower values for the thicker atmospheres till a comparatively larger phase angle ($\approx 70°$) than in the first case. After this α, F decreases sharply for the thinner atmosphere with 30 km thickness, while as the atmosphere becomes extended the rate at which F drops decreases and we see higher flux values than for thinner, less extended atmospheres for the corresponding phase angles (similar to the first case). Thus, F curves start to become flat. We see higher F values for larger phase angles in the second case than in first case, because, as the upper layers are more tenuous than the single layer in the first case, more photons can travel longer distances resulting into broader twilight zone than in in the first case. Comparing $\varphi(\alpha)$ curves for the first and second cases, it can be seen that the relative drop in F with respect to F at $\alpha = 0°$ is almost similar till $\alpha \approx 80°$ and then it starts diverging for the corresponding atmospheric thickness.

l [km] ↓	Layer 1 (b=1.0)	Layer 2 (b=0.2)	Layer 3 (b=0.1)
10	0.1	0.02	0.01
50	0.02	4E-3	2E-3
100	0.01	2E-3	1E-3
200	5E-3	1E-3	5E-4
250	4E-3	8E-4	4E-4
400	2.5E-3	5E-4	2.5E-4

Table 4.2: Table depicting values of k_{ext} for three atmospheric layers for different values of l. Columns 2, 3, and 4 depict k_{ext} values for layers 1, 2, and 3, respectively for a particular l depicted in Column 1. *Atmosphere total thickness = 3*l.*

Similar to the first case, we see that in the second case Q values for atmospheres of all thicknesses are similar for smaller phase angles and they start to become more negative for larger phase angles as the atmospheric extent increases. Although, in the second case, the values start to diverge at larger phase angles than in the first case. In the second case, P curves show significant variation with the atmospheric thickness than in the first case. P has higher values for larger phase angles with increasing atmospheric extent. This is because with decreasing k_{ext} values (and thus increasing probabilistic path lengths), the probability that the photon undergoes multiple scattering decreases. Thus, due to higher percentage of photons in the emergent flux that scattered less number of times as the atmospheric thickness increases, we see higher P values with increase in atmospheric extent for larger phase angles. This is also apparent from the fact that P curves peak and become more symmetrical closer to $\alpha = 90°$ with the increasing atmospheric extent, as the contribution of singly scattered photons increases.

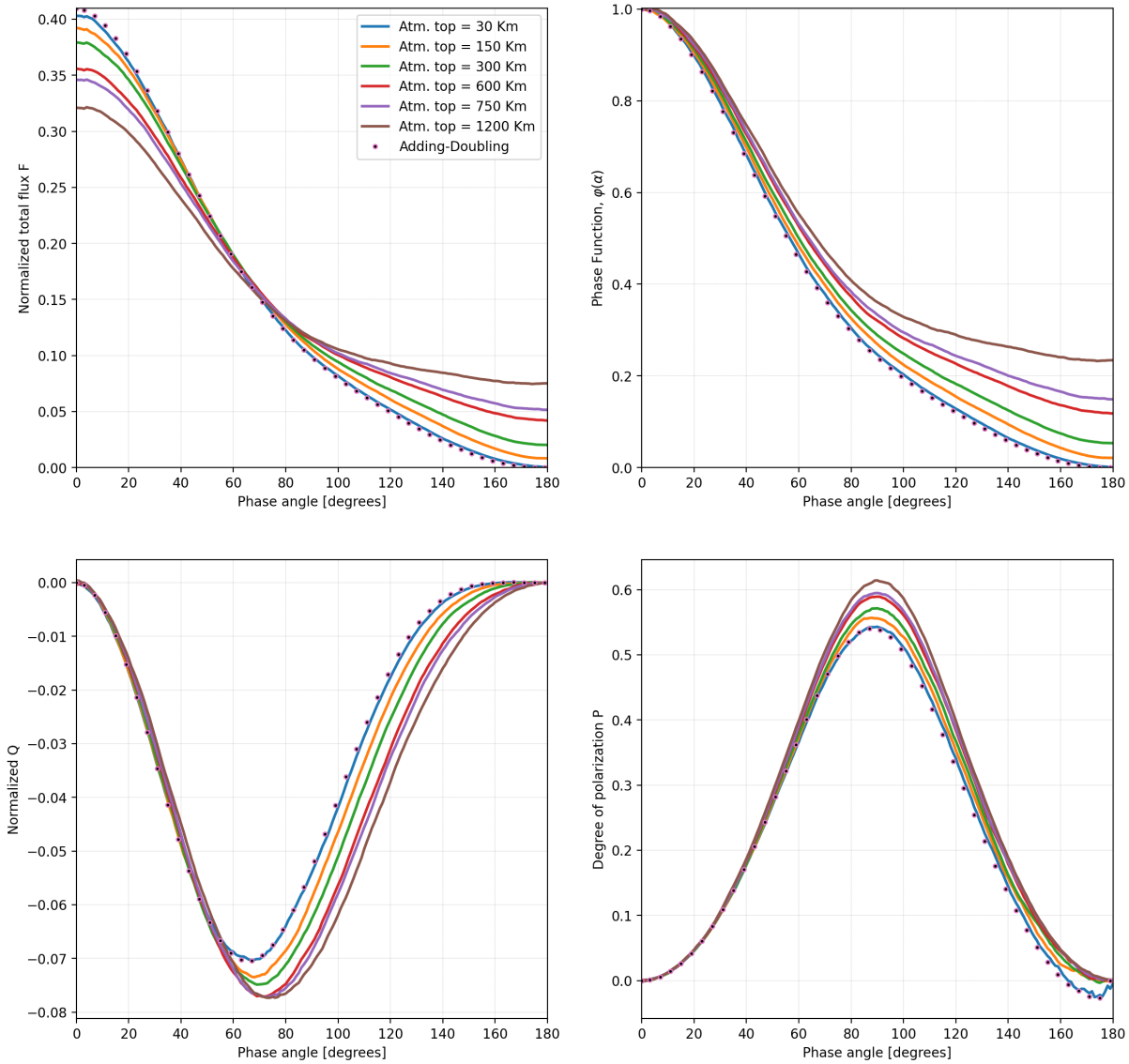

Figure 4.2: Same as Figure 4.1 but now the atmosphere is divided into three layers having the same geometrical thickness, while they have $b^m_{\text{sca}} = 1.0, 0.2, 0.1$ from the bottom-most to the top-most layer. For every model atmosphere, the layer thickness is *(atmosphere top altitude)*/3.

4.1.3. Atmospheres consisting of multiple layers, where layers have different geometrical thicknesses

In this subsection, we will discuss phase curves of the atmospheres consisting of multiple layers with different thicknesses which we discussed in Section 3.1. Figure 4.3 shows phase curves for these atmospheric settings.

l [km] ↓	Layer 1 (b=1.0)	Layer 2 (b=0.2)	Layer 3 (b=0.1)
5,10,15	0.2	0.02	6.66E-3
50,100,150	0.02	2E-3	6.66E-4
100,200,300	0.01	1E-3	3.33E-4
150,300,450	6.66E-3	6.66E-4	2.22E-4
200,400,600	5E-3	5E-4	1.66E-4

Table 4.3: Table depicting values of k_{ext} for three atmospheric layers for different values of l. Column 1 depicts the values of l from bottom-most to the top-most layer. Columns 2, 3, and 4 depict k_{ext} values for layers 1, 2, and 3, respectively. Atmosphere total thicknesses are 30, 300, 600, 900, and 1200 km.

As discussed in Section 3.1, this setting may resemble a more realistic atmosphere. From F curves it can be seen that the drop in A_G and F for the lower phase angles with increasing atmospheric extent is even higher than in the second case (Figure 4.2). This can be explained by looking at Tables 4.2 and 4.3. In this case, as l for the last (3rd) layer is higher than that from the second case, for a particular atmospheric extent, this layer is more tenuous and thus leading to longer photon paths in the atmosphere. Thus resulting in more photons passing through the atmosphere without interaction. It was found that for the extreme case of the atmosphere with 1200 km thickness, around 23% of a total number of incident photons didn't interact in the atmosphere leading to a lower number of scattered photons than in the second case. The shapes of F curves look similar to those in the second case. However, in this case, all the curves do not intersect at one particular phase angle. F curves for atmosphere with the thickness of 300 km and above intersect at around $\alpha = 100°$ (larger than the one for the second case) and longward of this phase angles, they show higher fluxes than the atmospheres with the same total geometric thicknesses from the second case. Also, we see that for larger phase angles F curves are flatter in the third case than in the second case.

Although P curves show almost the same variation with increasing atmospheric thickness in second and third cases (though the peaks of P have higher values in the third case), variation in Q curves differ significantly. In both cases, peaks of Q are shifted to higher αs with the increase in the atmospheric thickness, but the peak values of Q do not increase all the time in the third case, as opposed to in the second case. For the atmospheric thicknesses we investigated here, the maximum peak value of Q might have occurred for a thickness in between 300 and 600 km, and then it started to decrease. This is because the as upper layers became tenuous below a threshold that the total reflected flux was lower for the α at which atmospheres with total thicknesses of 300 and 600 km got their maximum Q. Shift of peaks of Q to higher phase angles, and shift of peaks of P towards $\alpha = 90°$ indicate more contribution of singly scattered photons as the atmospheric extent increases.

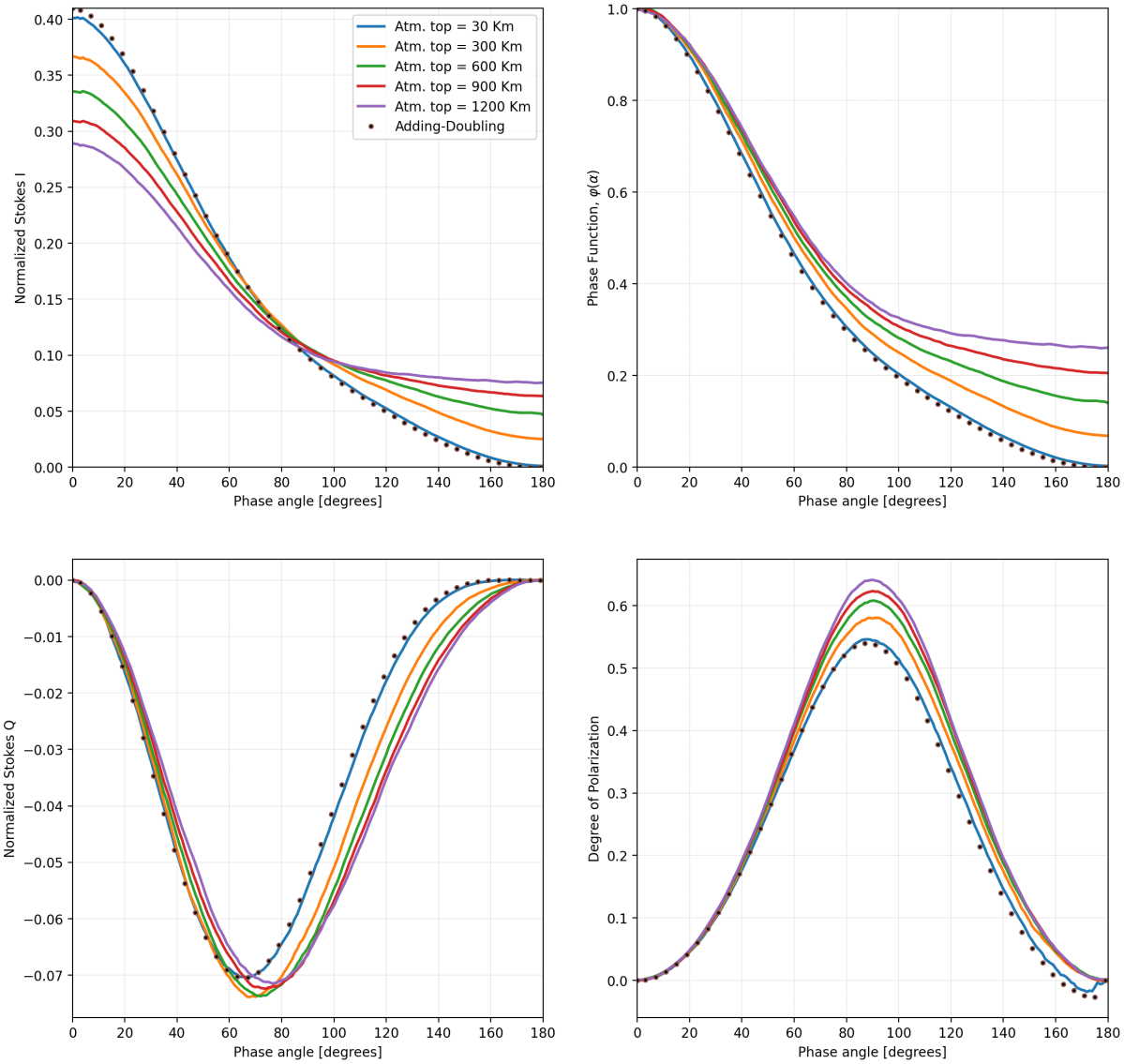

Figure 4.3: Same as Figure 4.1 but now the atmosphere is divided into three layers having different geometrical thicknesses, while they have $b^m_{\text{sca}} = 1.0, 0.2, 0.1$ from the bottom-most to the top-most layer. For every model atmosphere, layer thicknesses are 1x, 2x, and 3x km, where x = 5,50,100,150,200 km for the atmospheres with increasing total geometrical thicknesses.

4.2. Effect of the surface albedo

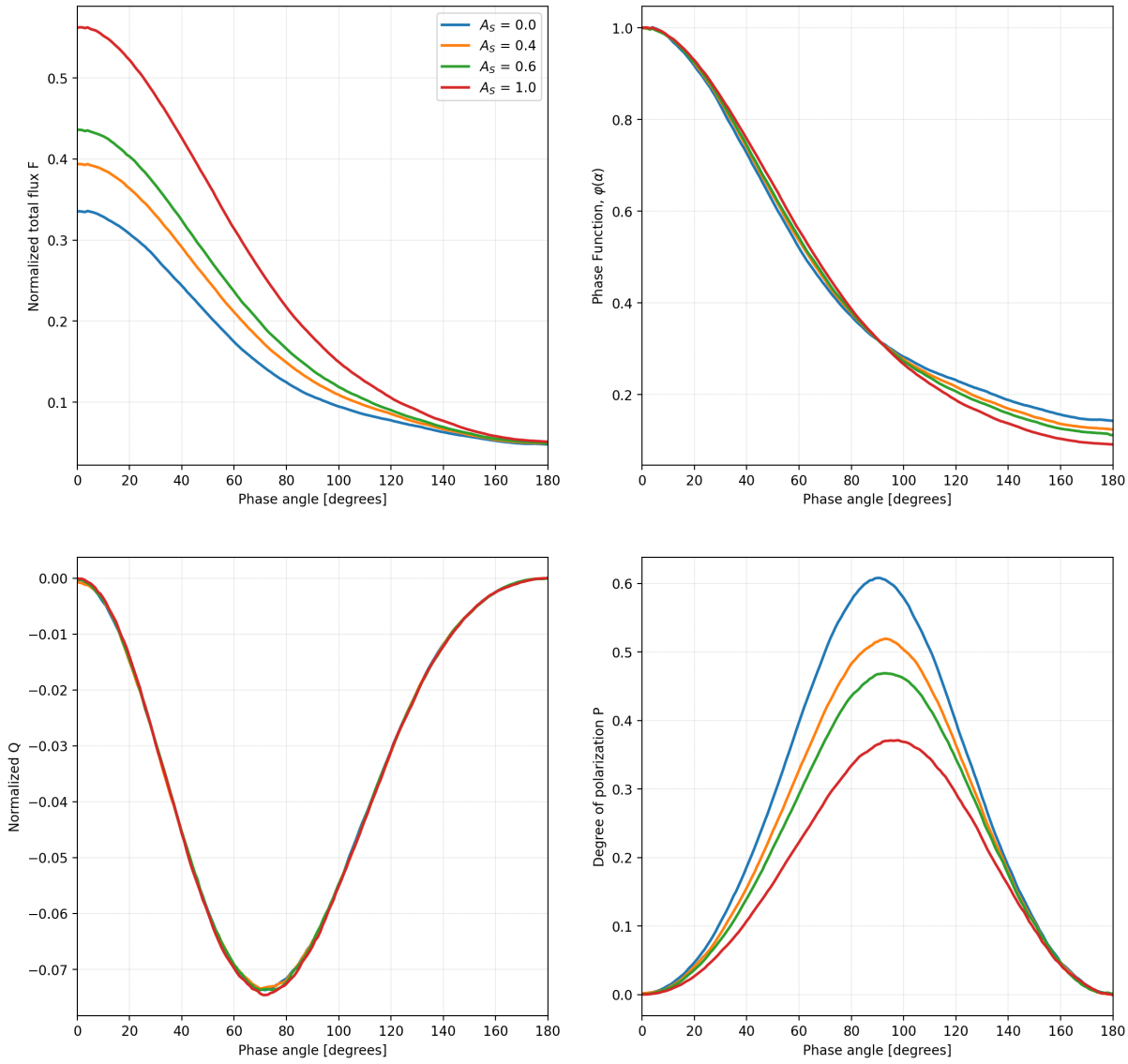

Figure 4.4: Same as Figure 4.1 but now for all the model planets, the atmospheric layers have l=100, 200, and 300 km, and thus the total atmospheric thickness is 600 km, while A_S is different.

Phase curves of planets with different surface albedos (A_S) that were described in Section 3.2 are shown in Figure 4.4. With the increase in A_S, geometric albedo (A_G) and total flux (F) at other phase angles also increase. This is because as the absorption by the surface decreases, more photons escape the atmosphere, contributing to the increased flux. We also see that F curves converge towards larger phase angles, showing that the role of the surface (albedo) on the emergent flux decreases with the increase in phase angle, because less of the surface is in view. $\varphi(\alpha)$ curves show interesting behavior with increase in α. From these curves we see that before $\alpha = 90°$, F relative to $\alpha = 0°$ is higher for a planet with a higher A_S, while after $\alpha = 90°$ we see a reversal and now it is higher for the planet with a lower A_S. This is because, before $\alpha = 90°$ larger portion of the planet is illuminated and thus A_S directly controls F emerging from the major part of the disk, while after that the atmosphere plays the major role in the emergent flux.

From the disk-resolved images in Section 3.2 we saw that the pattern for Q on the planetary disk diminishes with the increase in A_S (see Figure 3.16), but interestingly we see from Figure 4.4 that Q curves seem invariant to the change in surface albedo. Recall that we are using a Lambertian surface that completely depolarizes the light. We saw Q pattern diminishing in Figure 3.16 because along with photons that scattered only in the at-

mosphere and didn't reflect from the surface, we also see photons that were reflected by the surface and again scattered in the atmosphere. Now as we are using a homogeneous surface for the entire planet that reflects light isotropically, the distribution of the reflected photons and thus those get scattered and thus polarized in the atmosphere is symmetric over the planetary disk, specifically over the north-south hemispheres for all phase angles (although it is a bit difficult to see the exact symmetry in Figure 3.16 due to statistical fluctuations). This is the reason, integrated over the disk, Q (and in fact also U) caused by photons reflected from the surface and then scattered in the atmosphere is 0. Remember that we are using the same atmosphere setting for all the planets discussed in this section. And as the surface does not affect the overall disk integrated Q, we see that Q has the similar values for all the phase angles for all A_S cases (although we see slight differences due to statistical fluctuations). With increased surface albedo, the amount of depolarized light escaping the atmosphere increases, leading to smaller P values with an increase in the surface albedo. This is evident from P curves from Figure 4.4. The shift in peaks of P curves are due to the differences in F values as the Q values are similar for corresponding phase angles.

4.3. Effect of the single scattering albedo

In Section 3.3, we discussed disk resolved images of planets having atmospheres with same geometrical and optical thicknesses for the layers and same A_S, but having different single scattering albedos ($\tilde{\omega}$). Phase curves of F, Q, and P for those settings are shown in Figure 4.5.

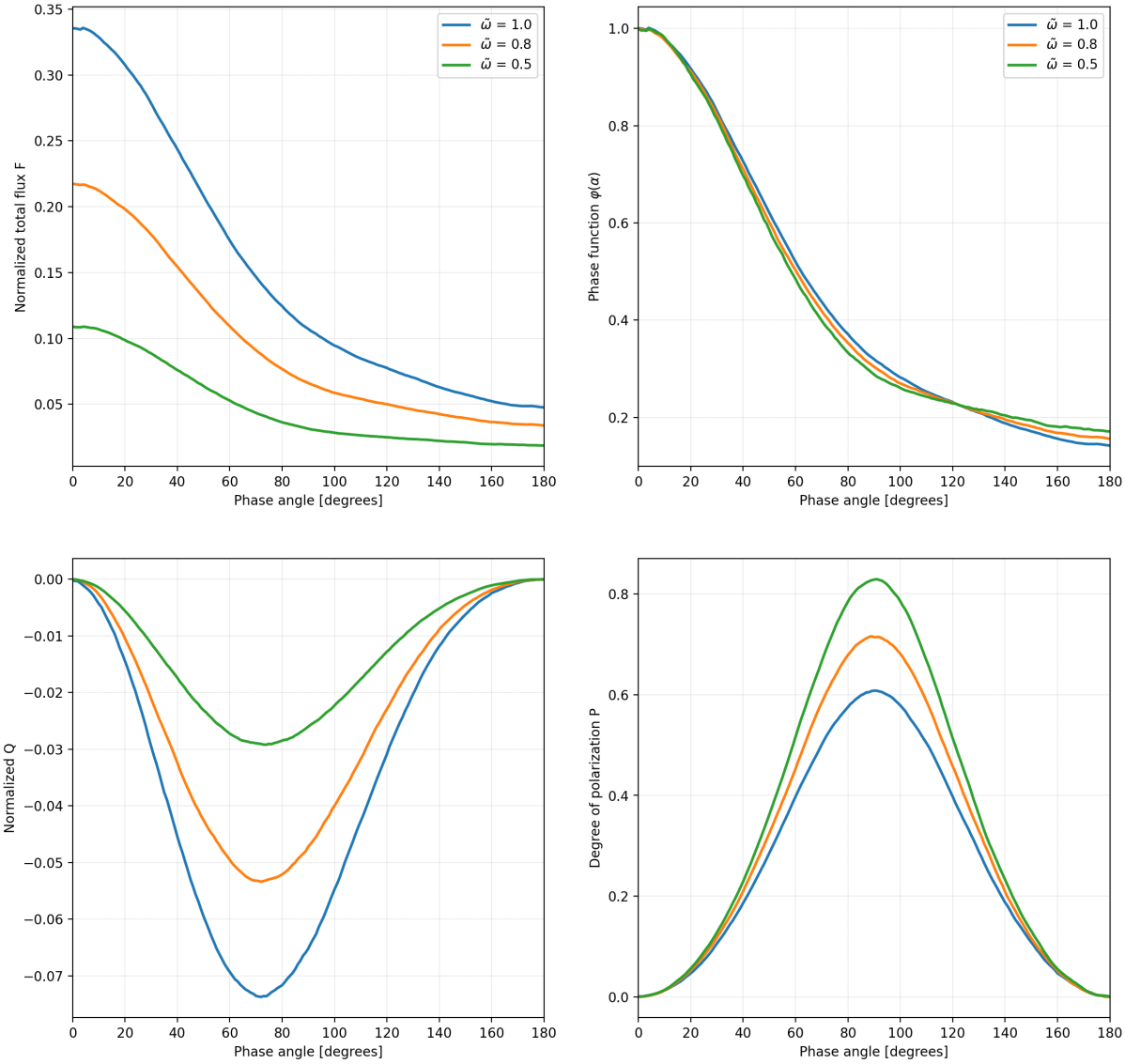

Figure 4.5: Same as Figure 4.1 but now for all the model planets, the atmospheric layers have l=100, 200, and 300 km, and thus the total atmospheric thickness is 600 km, $A_S = 0.0$, while the $\tilde{\omega}$ is different.

The drop in F across all phase angles with decreasing $\tilde{\omega}$ is because of more absorption in the atmosphere. $\varphi(\alpha)$ curves show smaller differences with the variation in $\tilde{\omega}$ meaning that the difference in variation in F with respect to F at $\alpha = 0°$ with changing $\tilde{\omega}$ is small.

Similar to F, Q curves show lower values with decreasing $\tilde{\omega}$, because of the increased absorption in the atmosphere and thus lower emergent flux out of the atmosphere. Higher P values for the atmosphere with lower $\tilde{\omega}$ attributes to decreased multiple scattering. Also peaks of P curves slightly shift toward $\alpha = 90°$ due to increased percentage of singly scattered photons, although it is a bit difficult to see this in Figure 4.5.

4.4. Titan's atmosphere

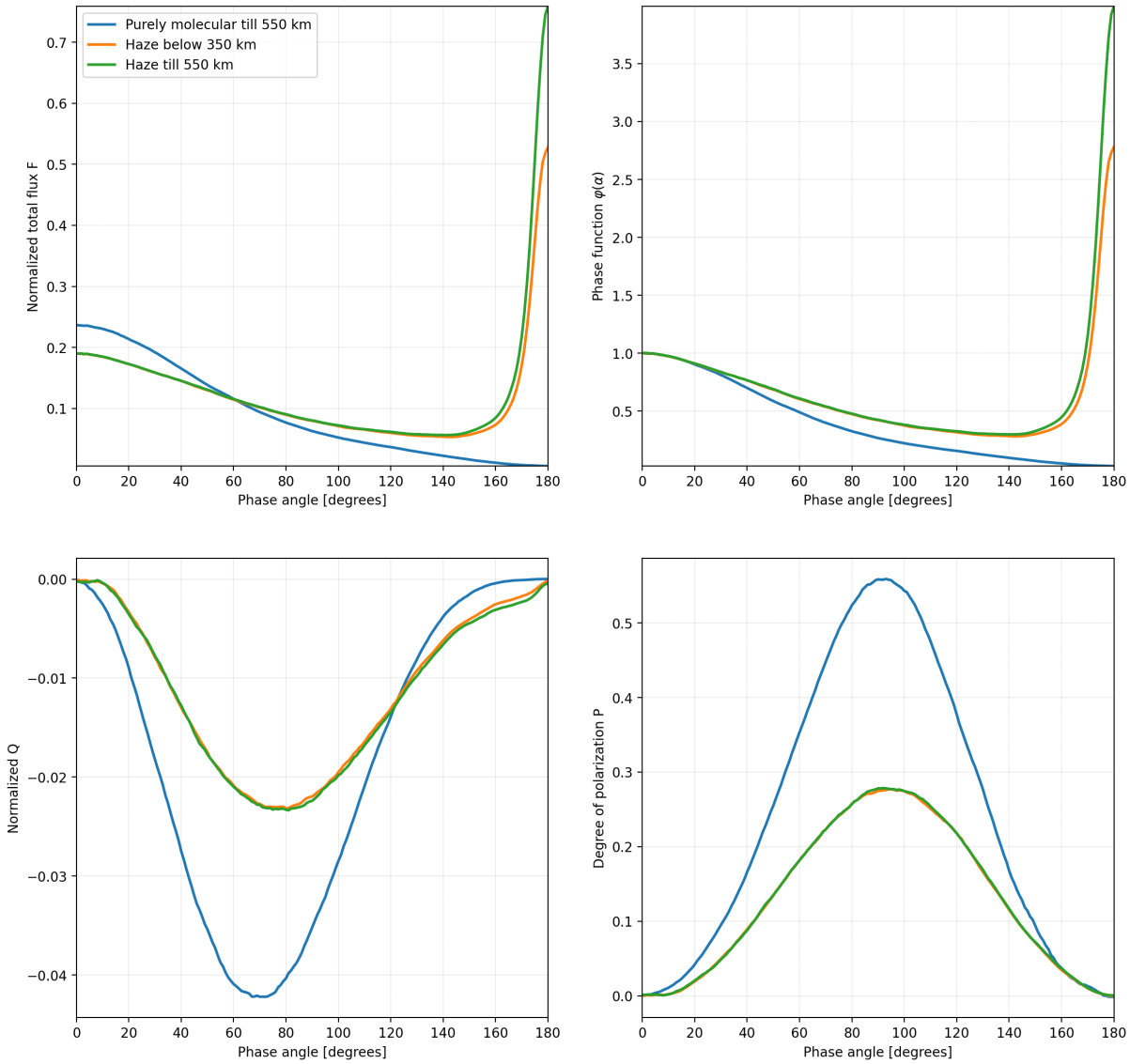

Figure 4.6: Same as Figure 4.1 but now for the three models of Titan's atmosphere, M550 (Purely molecular till 550 km), H350 (Haze below 350 km), and H550 (Haze till 550 km) discussed in Section 3.4

Figure 4.6 shows the phase curves for the three atmosphere models of Titan: M550, H350, and H550, which were discussed in Section 3.4. Remember that these models represent following atmospheric settings of scatterers:

- purely molecular till 550 km (model M550)
- molecules + haze till 350 km and then purely molecular till 550 km (model H350)
- molecules + haze till 550 km (model H550)

From F curves we can see that the geometrical albedo (A_G) for models H350 and H550 are lower than A_G for the model M550, owing to less backward scattering by haze particles than the molecules (see Figure 3.1). Also, we can see that though the atmosphere is extended till 550 km, we see negligible flux longward of $\alpha = 160°$ for the model M550 due to very low $b^m_{\rm sca}$ in the upper part of the atmosphere (see Table 3.2), and thus around 34.5% of total incoming photons passed through the atmosphere without any interaction (for the model H550

this percentage was 14%). On the other hand, for models H350 and H550, Titan starts to become brighter after $\alpha \approx 150°$ due to strong forward scattering by haze particles. F curves for models H350 and H550 also seem to diverge from this phase angle, and F at $\alpha = 180°$ for H550 is much higher than for H350. Remember that we used the same total haze optical depth (b^a) in both models. Thus the presence of haze at the higher altitudes (350 to 550 km) led to such a higher flux at these large phase angles. Looking at $\varphi(\alpha)$ curves, we can see that Titan is around 2.75 and 4 times brighter at $\alpha = 180°$ than at $\alpha = 0°$ for model H350 and H550, respectively. Garciá Munõz et al. (2017) found similar results (in qualitative terms; quantitatively they differ due to the difference in model settings) after analyzing the data from the Imaging Science Subsystem (ISS) instrument of the Cassini spacecraft for multiple phase angles at multiple wavelengths. Their phase curve results for normalized total flux (normalized such that at $\alpha = 0°$, the total flux represents geometrical albedo of Titan) are shown in Figure 4.7 while Titan's full disk images at $\alpha \approx 0°$ and $\alpha = 166°$ obtained using the CL1_CB3 filter combination and described in their work are shown in Figure 4.8.

Gas molecules cause higher polarization than haze particles (e.g. see P_{12} and P from Figure 3.1). For three models of Titan's atmosphere we presented, we can see that, though total b^a_{sca} is much higher than b^m_{sca}, from Figure 4.6 we see that Q from model M550 is higher for most of the phase angles than Q from models H350 and H550, except for larger phase angles, where the emergent total flux (and thus the polarized flux) for M550 becomes significantly lower. For model M550, P is higher than for model H350 and H550 for most of the phase angles and almost the same for some phase angles. For higher phase angles, though Q for the model M550 has lower values than for Q for models H350 and H550, P has higher or similar values because it is a relative measure.

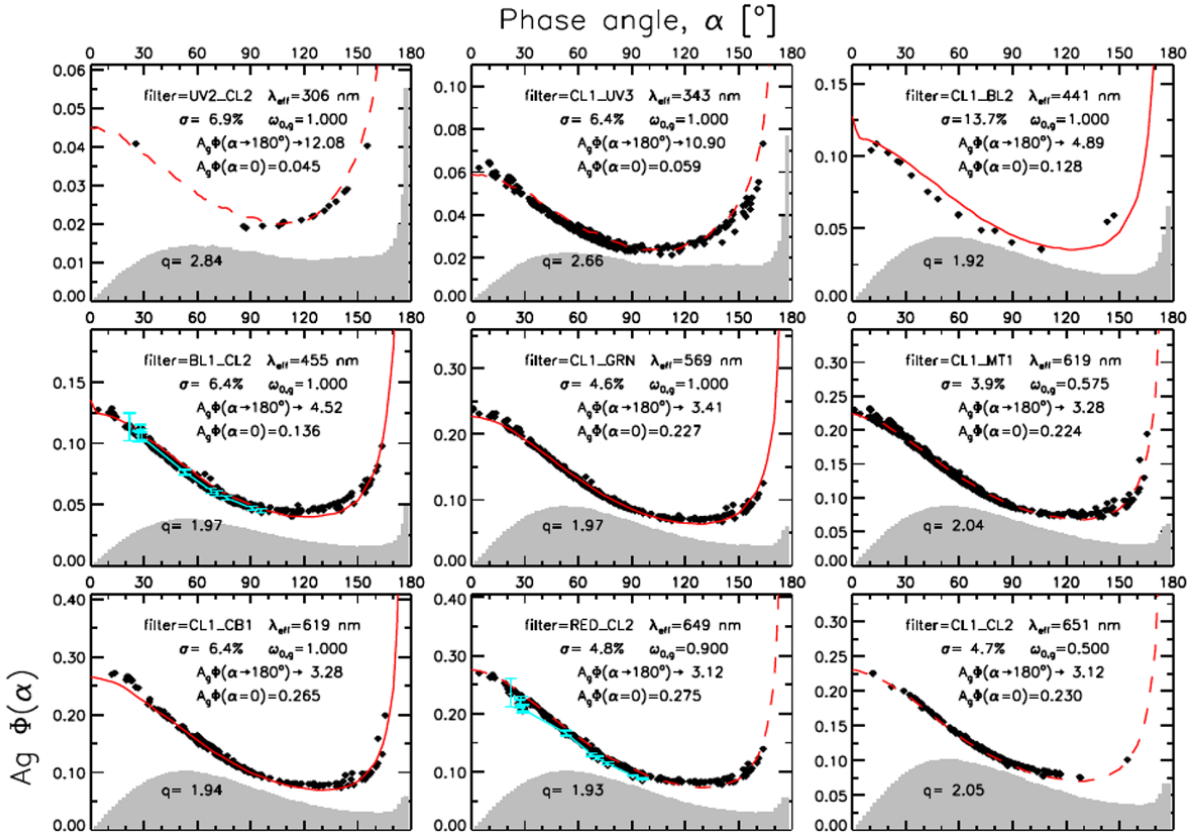

Figure 4.7: Figure 1 from Garciá Munõz et al. (2017). Original caption: "Cassini/ISS measurements (black symbols) and model calculations (red curves; see text for meaning of solid and dashed lines). Each graph contains information on filter combination and effective wavelength (λ_{eff}), mean relative difference between measurements and model (σ), adopted single scattering albedo of the gas ($\omega_{0,g}$), limiting values of $A_G\varphi(\alpha)$ for $\alpha \to 0°$ and 180°, and passband-averaged phase integral (q). The grey area shows (arbitrary normalization) the product $\varphi(\alpha)sin(\alpha)$ that enters into the evaluation of the phase integral $q(\equiv 2\int_0^\pi \varphi(\alpha)sin(\alpha)d\alpha)$. Pioneer 11 phase curves in blue (452 nm) and red (648 nm) passbands are shown in cyan color together with the Cassini/ISS curves for λ_{eff} =455 and 649 nm. The Pioneer 11 curves were re-normalized from $R_{452\text{nm}}$=2850 km and $R_{648\text{nm}}$=2800 km to R=2575 km." See Garciá Munõz et al. (2017) for meanings of the quantities described in the caption. We cropped the original image so as to include the phase function panels only till $\lambda = 649$ nm (we used $\lambda = 646$ nm for models M550, H350, and H550).

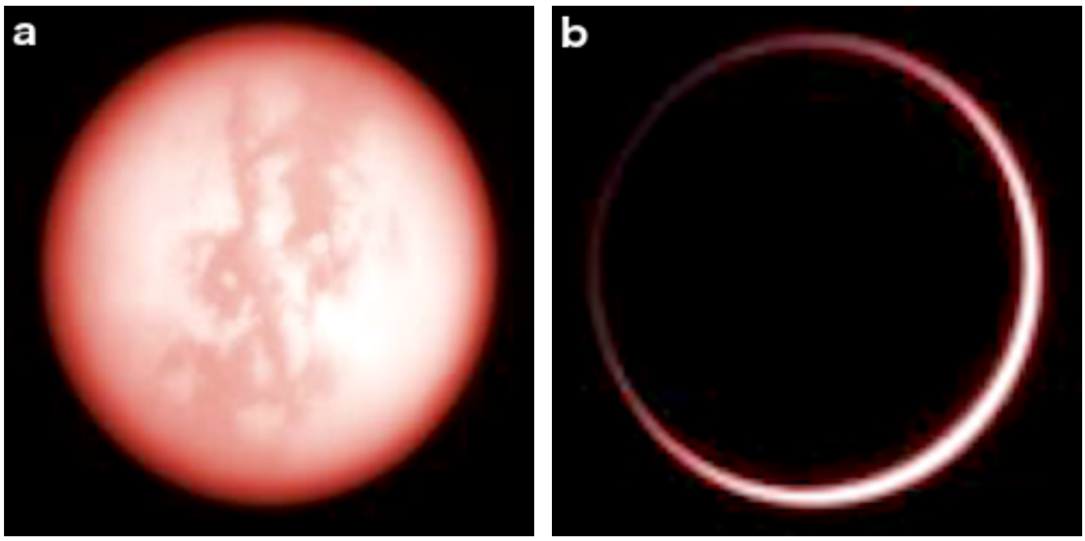

Figure 4.8: Figure 3 a and b from Garciá Munõz et al. (2017). Original caption: "Cassini/ISS images of Titan at $\alpha \approx 0°$ and $\alpha \approx 166°$ obtained with the CL1_CB3 filter combination (λ_{eff} =938 nm). The contrast in the full-disk image arises near the surface. The overall brightness of both configurations is nearly the same (Fig. 1), despite the disparate projected area of Titan's illuminated disk in each case (full disk for $\alpha \approx 0°$; the equivalent to a ring a few scale heights wide for $\alpha \approx 166°$)."

5

Conclusions and Discussion

Inspired by the need for a radiative transfer code that can accurately interpret spatially resolved images of Titan from ground-based telescopes as well as spacecrafts, we have developed, from scratch, a 3D radiative transfer code based on the Monte Carlo method, that fully takes into account the spherical shape of a planetary atmosphere, multiple scattering and the polarized nature of light. We named the code as Spherical POlarimetric Radiative Transfer (SPORT). Throughout its development, we did step-by-step validation of the code. First, we validated it using the simple case of an atmosphereless Lambertian sphere. Then we validated it for a planet having an atmosphere, using the phase curves of planetary total and polarized fluxes generated using the adding-doubling method as benchmarks. For these validations, we used different atmospheric optical depths as well as surface albedos. We used molecules as well as haze particles as scatterers and we ignored molecular absorption. From the validation tests, we confirmed that SPORT can be used to model and analyze total flux and polarization signals of starlight reflected from a planet. SPORT can produce planetary phase curves as well as disk-resolved images for total as well as polarized flux.

As SPORT considers the spherical shape of the atmosphere, it can be used to analyze observations near the planetary limb and of the twilight zone. Thus, we decided to simulate the flux and polarization signals for spatially resolved and spatially unresolved model planets. Our major conclusions are as follows:

Effect of the geometrical thickness of the atmosphere on observed total and polarized fluxes of a planet In the first step we tried to investigate at what atmospheric extent assumption of plane-parallel atmosphere introduces large errors for calculations around the limb of a planet in case of small phase angles and the twilight zone in case of large phase angles. For this investigation, we used a simple model planet with a radius of 2575 km and we assumed the surface albedo to be 0 to investigate solely the atmospheric effect. We considered a purely molecular atmosphere. We did the investigation for three different atmospheric settings: atmosphere consisting of only one homogeneous layer, atmosphere consisting of multiple layers where layers have the same geometrical thickness but different optical thicknesses, atmosphere consisting of multiple layers where layers have different geometrical and optical thicknesses. In all these settings total optical thickness of the atmosphere was kept to be the same. These settings allowed us to take into account possible ways in which the atmosphere can be vertically inhomogeneous (in terms of distribution of optical thickness) and its effect on the observed flux and polarization signals. We did simulations for different atmospheric geometrical thicknesses. For these simulations, we found the following results:

- Atmospheric geometrical thickness at which it is important to take into account the sphericity of the atmosphere to avoid large errors in total and polarized flux calculations strongly depends on the total optical thickness of the atmosphere as well the vertical distribution of this optical thickness.
- By analyzing disk resolved images we found that for a particular atmospheric thickness, errors introduced due to not taking into account the sphericity of the atmosphere are larger at large phase angles (where errors primarily arise due to neglecting light coming from the twilight zone of the planet) than at small phase angles (where errors primarily arise due to neglecting the gradient in brightness around the limb of the planetary disk).
- When we increase the geometrical thickness of the atmosphere while keeping the optical thickness the same, we found that the planet becomes darker at smaller phase angles while it becomes brighter

at large phase angles due to the broadening of the twilight zone. We found that the amount of this variation in brightness depends on the vertical distribution of the total atmospheric optical thickness.

- For disk resolved planets, we see the degree of polarization to be higher around the limb of the planet or around the edges of the denser part of the atmosphere than in the inner part of the disk for small phase angles, while it is larger around the limb than the inner part of the disk for large phase angles.

- For vertically inhomogeneous atmospheres the degree of polarization increases for larger phase angles with an increase in the atmospheric extent.

Effect of the surface albedo on observed total and polarized fluxes of a planet with an extended atmosphere
In the next step, we investigated the effect of the surface albedo on total and polarized flux signals of spatially resolved and unresolved planets having an extended atmosphere. We considered the same atmospheric setting for all the planets while we varied the surface albedo. Also, we considered a Lambertian surface. We found the following results:

- Total flux of a planet increases for most of the phase angles. The influence of the surface albedo on the total flux decreases with an increase in phase angle.

- Increase in surface albedo diminishes on-disk patterns of polarized flux Q (and U), however, it does not affect the disk integrated value of Q.

- Degree of polarization decreases with an increase in surface albedo. Also the peak of the degree of polarization phase curve shifts towards a higher phase angle with the increase in surface albedo.

Effect of the single scattering albedo on observed total and polarized fluxes of a planet with an extended atmosphere
In the next step, we considered planets with the same atmospheric settings in terms of optical and geometrical thicknesses of the atmospheric layers. We assumed the surface albedo to be 0 and we varied the single scattering albedo. We found the following results:

- Decreasing single scattering albedo decreases total as well as polarized flux across all phase angles.

- For disk resolved planets we observed that decreasing single scattering albedo decreases the degree of polarization around the limb for small phase angles, while it increases the degree of polarization across the disk for large phase angles.

- The peak of the degree of polarization phase curve shifts towards the phase angle = 90° with the decrease in single scattering albedo.

Titan's atmosphere
After investigating total and polarized flux signals of hypothetical planets having extended atmospheres, we simulated disk-resolved images and phase curves of total and polarized fluxes of Titan. We used surface albedo to be 0.2 and considered the atmospheric geometrical thickness of 550 km. We analyzed three model atmospheres for Titan: purely molecular till 550 km (model M550), molecules + haze till 350 km and purely molecular from 350 to 550 km (model H350), and molecules + haze till 550 km (model H550). For the model settings we used, We found the following results:

- For smaller phase angles Titan looks brighter for the M550 model. From models H350 and H550 we see that its limb is strongly affected by the addition of haze.

- Titan appears brighter at large phase angles than at small phase angles due to the strong forward scattering nature of haze particles in its atmosphere. Moreover, it appears brighter at large phase angles for model H550 than for model H350 even when the total haze optical depth of the atmosphere in both the models is the same. This indicates that the presence of haze in its upper atmosphere strongly affects Titan's brightness at large phase angles due to the extendedness of its atmosphere.

- Titan showed lower Q values for models H350 and H550 than for the model M550 for most of the phase angles except at larger phase angles.

- This brings us to an important conclusion that errors in total and polarized flux calculations arising due to neglecting the sphericity of the atmosphere also depend on the composition of the atmosphere.
- Titan shows a lower degree of polarization across all phase angles for models H350 and H550 than for the model M550.

From the above conclusions we find that for every planet/moon we need to individually assess if the assumption of plane-parallel atmosphere introduces large errors for analyzing their total and polarized flux observations because of the dependence of errors on the factors discussed in conclusions. This also depends on the research goals. To study spatially resolved observations of twilight zones of the solar system planets/moons especially taken at high phase angles from spacecrafts, and for the near limb observations of Titan taken at smaller phase angles spherical atmospheric models seem to be important tools. One of the important use of spherical models can be to constrain the radius of exoplanets using their transit signals. Scatterers such as haze particles that strongly scatter light in a forward direction may enhance the transit signal of exoplanets and thus causing a smaller dip in the stellar flux. This may lead to large errors in constraining exoplanetary radius through their transit signals. Finally, spherical models can be used to effectively study puffy exoplanets or rocky exoplanets having extended atmospheres using their polarimetric phase curves which may be available in near future. Thus, SPORT (with further added functionalities) seems to be an effective tool for such studies.

6

Recommendations for Future Work

Following features can be added in SPORT and they will be subject of its upcoming development.

Fresnel reflection
Currently, in SPORT, we have modeled planetary surface to be Lambertian which completely depolarizes the light after surface reflection. However, reflection of light from a liquid surface cannot be modeled using a Lambertian surface because reflection by a liquid surface changes the polarization of light. Reflection by liquid surface can be modeled using Fresnel equations. This is essential to study Titan's seas/lakes and also it can possibly help to detect oceans on exoplanets (Trees and Stam, 2019).

Atmospheric refraction
Refraction can modify the propagation path as well as the polarization state of light. Hu et al. (2016) found that relative changes in total fluxes of reflected and transmitted light due to atmospheric refraction can be as high as 6.3% and 7.4% for Rayleigh scattering atmosphere, 7.2% and 7.8% for an atmosphere consisting aerosol, and 6.2% and 6.8% for a cloudy atmosphere, respectively. They also found that relative change in the degree of polarization due to refraction can be as high as 9.5%. Thus taking into account refraction can improve the accuracy of radiative transfer calculations, especially e.g. to study transit signals of exoplanets.

Gaseous absorption
In the current version of SPORT, we modeled atmospheric absorption only using a single scattering albedo of scatterers. However, to analyze observations in wavelength bands in which some atmospheric gas has strong absorption e.g. methane in case of Titan, it is essential to consider gaseous absorption.

Addition of clouds and inhomogeneity in the atmosphere
Clouds can strongly affect flux and polarization signals of a planet. Thus to detect their presence in the planetary atmosphere and to characterize their properties it is essential to consider them in radiative transfer calculations. Planetary atmospheres can have inhomogeneity (e.g. change in particle number density, composition, etc.) even at similar altitudes. Thus a provision to construct inhomogeneous atmospheric layers should be made.

Bibliography

J. W. Barnes, R. N. Clark, C. Sotin, M. Ádámkovics, T. Appéré, S. Rodriguez, J. M. Soderblom, R. H. Brown, B. J. Buratti, K. H. Baines, S. L. Mouélic, and P. D. Nicholson. A TRANSMISSION SPECTRUM OF TITAN'S NORTH POLAR ATMOSPHERE FROM A SPECULAR REFLECTION OF THE SUN. *The Astrophysical Journal*, 777(2):161, 10 2013. ISSN 0004-637X. doi: 10.1088/0004-637X/777/2/161.

D. R. Bates. Rayleigh scattering by air. *Planetary and Space Science*, 32(6):785–790, 6 1984. ISSN 00320633. doi: 10.1016/0032-0633(84)90102-8.

J.-L. Beuzit, A. Vigan, D. Mouillet, K. Dohlen, R. Gratton, A. Boccaletti, J.-F. Sauvage, H. M. Schmid, M. Langlois, C. Petit, A. Baruffolo, M. Feldt, J. Milli, Z. Wahhaj, L. Abe, U. Anselmi, J. Antichi, R. Barette, J. Baudrand, P. Baudoz, A. Bazzon, P. Bernardi, P. Blanchard, R. Brast, P. Bruno, T. Buey, M. Carbillet, M. Carle, E. Cascone, F. Chapron, J. Charton, G. Chauvin, R. Claudi, A. Costille, V. De Caprio, J. de Boer, A. Delboulbé, S. Desidera, C. Dominik, M. Downing, O. Dupuis, C. Fabron, D. Fantinel, G. Farisato, P. Feautrier, E. Fedrigo, T. Fusco, P. Gigan, C. Ginski, J. Girard, E. Giro, D. Gisler, L. Gluck, C. Gry, T. Henning, N. Hubin, E. Hugot, S. Incorvaia, M. Jaquet, M. Kasper, E. Lagadec, A.-M. Lagrange, H. Le Coroller, D. Le Mignant, B. Le Ruyet, G. Lessio, J.-L. Lizon, M. Llored, L. Lundin, F. Madec, Y. Magnard, M. Marteaud, P. Martinez, D. Maurel, F. Ménard, D. Mesa, O. Möller-Nilsson, T. Moulin, C. Moutou, A. Origné, J. Parisot, A. Pavlov, D. Perret, J. Pragt, P. Puget, P. Rabou, J. Ramos, J.-M. Reess, F. Rigal, S. Rochat, R. Roelfsema, G. Rousset, A. Roux, M. Saisse, B. Salasnich, E. Santambrogio, S. Scuderi, D. Segransan, A. Sevin, R. Siebenmorgen, C. Soenke, E. Stadler, M. Suarez, D. Tiphène, M. Turatto, S. Udry, F. Vakili, L. B. F. M. Waters, L. Weber, F. Wildi, G. Zins, and A. Zurlo. SPHERE: the exoplanet imager for the Very Large Telescope. *A&A*, 631, 2019. URL https://doi.org/10.1051/0004-6361/201935251.

M. R. Bolcar, L. Feinberg, K. France, B. J. Rauscher, D. Redding, and D. Schiminovich. Initial technology assessment for the Large-Aperture UV-Optical-Infrared (LUVOIR) mission concept study. In *Space Telescopes and Instrumentation 2016: Optical, Infrared, and Millimeter Wave*, volume 9904, page 99040J. SPIE, 7 2016. ISBN 9781510601871. doi: 10.1117/12.2230769. URL https://ui.adsabs.harvard.edu/abs/2016SPIE.9904E..0JB/abstract.

J. F. Brossier, S. Rodriguez, T. Cornet, A. Lucas, J. Radebaugh, L. Maltagliati, S. Le Mouélic, A. Solomonidou, A. Coustenis, M. Hirtzig, R. Jaumann, K. Stephan, and C. Sotin. Geological Evolution of Titan's Equatorial Regions: Possible Nature and Origin of the Dune Material. *Journal of Geophysical Research: Planets*, 123(5): 1089–1112, 5 2018. ISSN 21699100. doi: 10.1029/2017JE005399. URL https://doi.org/.

Carrión-González, A. G. Muñoz, J. Cabrera, S. Csizmadia, N. C. Santos, and H. Rauer. Catalogue of exoplanets accessible in reflected starlight to the Nancy Grace Roman Space Telescope. A population study and prospects for phase-curve measurements. 4 2021. URL http://arxiv.org/abs/2104.04296.

S. Chandrasekhar. *Radiative Transfer*. Dover Books on Intermediate and Advanced Mathematics. Dover Publications, 1950. ISBN 9780486605906. URL https://books.google.nl/books?id=CK3HDRwCT5YC.

D. Cordier and B. Seignovert. Titan's seas observed in polarized light. In *European Planetary Science Congress (EPSC) - Division for Planetary Sciences (DPS)*, Geneva, 9 2019. EPSC-DPS. URL https://meetingorganizer.copernicus.org/EPSC-DPS2019/EPSC-DPS2019-1900-2.pdf.

L. R. Doose, E. Karkoschka, M. G. Tomasko, and C. M. Anderson. Vertical structure and optical properties of Titan's aerosols from radiance measurements made inside and outside the atmosphere. *Icarus*, 270:355–375, 5 2016. ISSN 10902643. doi: 10.1016/j.icarus.2015.09.039. URL https://www.sciencedirect.com/science/article/pii/S0019103515004534?via%3Dihub.

M. Fulchignoni, F. Ferri, F. Angrilli, A. J. Ball, A. Bar-Nun, M. A. Barucci, C. Bettanini, G. Bianchini, W. Borucki, G. Colombatti, M. Coradini, A. Coustenis, S. Debei, P. Falkner, G. Fanti, E. Flamini, V. Gaborit, R. Grard, M. Hamelin, A. M. Harri, B. Hathi, I. Jernej, M. R. Leese, A. Lehto, P. F. Lion Stoppato, J. J. López-Moreno,

T. Mäkinen, J. A. McDonnell, C. P. McKay, G. Molina-Cuberos, F. M. Neubauer, V. Pirronello, R. Rodrigo, B. Saggin, K. Schwingenschuh, A. Seiff, F. Simões, H. Svedhem, T. Tokano, M. C. Towner, R. Trautner, P. Withers, and J. C. Zarnecki. In situ measurements of the physical characteristics of Titan's environment. *Nature*, 438(7069):785–791, 12 2005. ISSN 14764687. doi: 10.1038/nature04314.

A. Garciá Munõz, P. Lavvas, and R. A. West. Titan brighter at twilight than in daylight. *Nature Astronomy*, 1(5): 1–7, 3 2017. ISSN 23973366. doi: 10.1038/s41550-017-0114. URL https://www-nature-com.tudelft.idm.oclc.org/articles/s41550-017-0114.

J. E. Hansen and L. D. Travis. Light scattering in planetary atmospheres. *Space Science Reviews*, 16(4):527–610, 10 1974. ISSN 0038-6308. doi: 10.1007/BF00168069. URL http://link.springer.com/10.1007/BF00168069.

Q. He, Z. Fang, O. Shoshamin, S. Brown, and Y. Rudich. Scattering and Absorption Cross-sections of Atmospheric Gases in the Ultraviolet-Visible Wavelength Range (307–725 nm). *Atmospheric Chemistry and Physics Discussions*, pages 1–32, 2020. ISSN 1680-7316. doi: 10.5194/acp-2020-941.

M. Hirtzig, B. Bézard, E. Lellouch, A. Coustenis, C. de Bergh, P. Drossart, A. Campargue, V. Boudon, V. Tyuterev, P. Rannou, T. Cours, S. Kassi, A. Nikitin, D. Mondelain, S. Rodriguez, and S. Le Mouélic. Titan's surface and atmosphere from Cassini/VIMS data with updated methane opacity. *Icarus*, 226(1):470–486, 9 2013. ISSN 00191035. doi: 10.1016/j.icarus.2013.05.033.

S. M. Hörst. Titan's atmosphere and climate. *Journal of Geophysical Research: Planets*, 122(3):432–482, 3 2017. ISSN 21699100. doi: 10.1002/2016JE005240.

J. W. Hovenier and C. V. M. van der Mee. Fundamental relationships relevant to the transfer of polarized light in a scattering atmosphere. *Astronomy and Astrophysics*, 128(1):1–16, 11 1983.

J. W. Hovenier, C. Van Der Mee, and H. Domke. *Transfer of Polarized Light in Planetary Atmospheres : Basic Concepts and Practical Methods*, volume 318. Springer Netherlands, 2004. ISBN 978-1-4020-2889-2. doi: 10.1007/978-1-4020-2856-4. URL http://link.springer.com/10.1007/978-1-4020-2856-4.

S. Hu, T. C. Gao, H. Li, L. Liu, X. C. Liu, T. Zhang, T. J. Cheng, W. T. Li, Z. H. Dai, and X. Su. Effect of atmospheric refraction on radiative transfer in visible and near-infrared band: Model development, validation, and applications. *Journal of Geophysical Research*, 121(5):2349–2368, 3 2016. ISSN 21562202. doi: 10.1002/2015JD024105. URL https://agupubs-onlinelibrary-wiley-com.tudelft.idm.oclc.org/doi/full/10.1002/2015JD024105https://agupubs-onlinelibrary-wiley-com.tudelft.idm.oclc.org/doi/abs/10.1002/2015JD024105https://agupubs-onlinelibrary-wiley-com.tudelft.idm.oclc.org/doi/10.1002/2015JD024105.

T. Karalidi, D. M. Stam, and D. Guirado. Flux and polarization signals of spatially inhomogeneous gaseous exoplanets. *Astronomy and Astrophysics*, 555:127, 7 2013. ISSN 00046361. doi: 10.1051/0004-6361/201321492. URL https://www.aanda.org/articles/aa/full_html/2013/07/aa21492-13/aa21492-13.htmlhttps://www.aanda.org/articles/aa/abs/2013/07/aa21492-13/aa21492-13.html.

E. Karkoschka. Seasonal variation of Titan's haze at low and high altitudes from HST-STIS spectroscopy. *Icarus*, 270:339–354, 5 2016. ISSN 10902643. doi: 10.1016/j.icarus.2015.07.007.

J. C. Kemp, G. D. Henson, C. T. Steiner, and E. R. Powell. The optical polarization of the Sun measured at a sensitivity of parts in ten million. *Nature*, 326(6110):270–273, 1987. ISSN 00280836. doi: 10.1038/326270a0. URL https://www-nature-com.tudelft.idm.oclc.org/articles/326270a0.

D. W. Mackowski and M. I. Mishchenko. A multiple sphere T-matrix Fortran code for use on parallel computer clusters. *Journal of Quantitative Spectroscopy and Radiative Transfer*, 112:2182–2192, 2011. doi: 10.1016/j.jqsrt.2011.02.019. URL www.elsevier.com/locate/jqsrt.

M. Mastrogiuseppe, A. Hayes, V. Poggiali, R. Seu, J. I. Lunine, and J. D. Hofgartner. Radar Sounding Using the Cassini Altimeter: Waveform Modeling and Monte Carlo Approach for Data Inversion of Observations of Titan's Seas. *IEEE Transactions on Geoscience and Remote Sensing*, 54(10):5646–5656, 10 2016. ISSN 01962892. doi: 10.1109/TGRS.2016.2563426.

M. Mastrogiuseppe, A. G. Hayes, V. Poggiali, J. I. Lunine, R. D. Lorenz, R. Seu, A. Le Gall, C. Notarnicola, K. L. Mitchell, M. Malaska, and S. P. Birch. Bathymetry and composition of Titan's Ontario Lacus derived from Monte Carlo-based waveform inversion of Cassini RADAR altimetry data. *Icarus*, 300:203–209, 1 2018a. ISSN 10902643. doi: 10.1016/j.icarus.2017.09.009.

M. Mastrogiuseppe, V. Poggiali, R. Seu, G. D. Achille, M. Mastrogiuseppe, V. Poggiali, A. G. Hayes, J. I. Lunine, R. Seu, G. Di Achille, and R. D. Lorenz. Cassini radar observation of Punga Mare and environs: Bathymetry and composition Bathymetry of Titan's seas and lakes View project Cassini radar observation of Punga Mare and environs: Bathymetry and composition. *Earth and Planetary Science Letters*, 496:89–95, 2018b. doi: 10.1016/j.epsl.2018.05.033. URL www.elsevier.com/locate/epsl.

B. Mennesson, S. Gaudi, S. Seager, K. Cahoy, S. Domagal-Goldman, L. Feinberg, O. Guyon, J. Kasdin, C. Marois, D. Mawet, T. Motohide, D. Mouillet, T. Prusti, A. Quirrenbach, T. Robinson, L. Rogers, P. Scowen, R. Somerville, K. Stapelfeldt, D. Stern, M. Still, M. Turnbull, J. Booth, A. Kiessling, G. Kuan, K. Warfield, H. A. Macewen, G. G. Fazio, and M. Lystrup. The Habitable Exoplanet (HabEx) Imaging Mission: preliminary science drivers and technical requirements Downloaded From: http://proceedings.spiedigitallibrary.org/ on 11/11/2016 Terms of Use: http://spiedigitallibrary.org/ss/termsofuse.aspx. 9904:99040–99041, 2016. doi: 10.1117/12.2240457. URL http://proceedings.spiedigitallibrary.org/.

M. I. Mishchenko, L. D. Travis, and D. W. Mackowski. T-matrix computations of light scattering by nonspherical particles: A review. *Journal of Quantitative Spectroscopy and Radiative Transfer*, 55(5):535–575, 5 1996. ISSN 00224073. doi: 10.1016/0022-4073(96)00002-7.

M. I. Mishchenko, J. W. Hovenier, and L. D. Travis. *Light Scattering by Nonspherical Particles: Theory, Measurements, and Applications*. Academic Press, San Diego, 2000 edition, 2000. ISBN 9780080510200.

M. F. Modest. The Monte Carlo Method for Surface Exchange. In *Radiative Heat Transfer*, pages 247–266. Elsevier, 1 2013. doi: 10.1016/b978-0-12-386944-9.50008-x.

H. B. Niemann, S. K. Atreya, J. E. Demick, D. Gautier, J. A. Haberman, D. N. Harpold, W. T. Kasprzak, J. I. Lunine, T. C. Owen, and F. Raulin. Composition of Titan's lower atmosphere and simple surface volatiles as measured by the Cassini-Huygens probe gas chromatograph mass spectrometer experiment. *Journal of Geophysical Research*, 115(E12):E12006, 12 2010. ISSN 0148-0227. doi: 10.1029/2010JE003659. URL http://doi.wiley.com/10.1029/2010JE003659.

C. C. Porco, R. A. West, S. Squyres, A. Mcewen, P. Thomas, C. D. Murray, A. Delgenio, A. P. Ingersoll, T. V. Johnson, G. Neukum, J. Veverka, L. Dones, A. Brahic, J. A. Burns, V. Haemmerle, B. Knowles, D. Dawson, T. Roatsch, K. Beurle, and W. Owen. Cassini Imaging Science: Instrument Characteristics And Anticipated Scientific Investigations At Saturn. *Space Science Reviews*, 115(1-4):363–497, 11 2004. ISSN 0038-6308. doi: 10.1007/s11214-004-1456-7. URL http://link.springer.com/10.1007/s11214-004-1456-7.

K. Rages and J. B. Pollack. Vertical distribution of scattering hazes in Titan's upper atmosphere. *Icarus*, 55(1): 50–62, 7 1983. ISSN 10902643. doi: 10.1016/0019-1035(83)90049-0.

J. C. Ramella-Roman, S. A. Prahl, and S. L. Jacques. Three Monte Carlo programs of polarized light transport into scattering media: part I. *Optics Express*, 13(12):4420, 6 2005. ISSN 1094-4087. doi: 10.1364/opex.13.004420.

L. Rossi and D. M. Stam. Circular polarization signals of cloudy (exo)planets. *Astronomy and Astrophysics*, 616:A117, 8 2018. ISSN 14320746. doi: 10.1051/0004-6361/201832619. URL https://www.aanda.org/articles/aa/full_html/2018/08/aa32619-18/aa32619-18.htmlhttps://www.aanda.org/articles/aa/abs/2018/08/aa32619-18/aa32619-18.html.

B. Seignovert, P. Rannou, R. A. West, and S. Vinatier. Haze Seasonal Variations of Titan's Upper Atmosphere during the Cassini Mission. *The Astrophysical Journal*, 907(1):36, 1 2021. ISSN 0004-637X. doi: 10.3847/1538-4357/abcd3b. URL https://doi.org/10.3847/1538-4357/abcd3b.

D. Spergel, N. Gehrels, J. Breckinridge, M. Donahue, A. Dressler, B. S. Gaudi, T. Greene, O. Guyon, C. Hirata, J. Kalirai, N. J. Kasdin, W. Moos, S. Perlmutter, M. Postman, B. Rauscher, J. Rhodes, Y. Wang, D. Weinberg, J. Centrella, W. Traub, C. Baltay, J. Colbert, D. Bennett, A. Kiessling, B. Macintosh, J. Merten, M. Mortonson,

M. Penny, E. Rozo, D. Savransky, K. Stapelfeldt, Y. Zu, C. Baker, E. Cheng, D. Content, J. Dooley, M. Foote, R. Goullioud, K. Grady, C. Jackson, J. Kruk, M. Levine, M. Melton, C. Peddie, J. Ruffa, and S. Shaklan. Wide-Field InfraRed Survey Telescope-Astrophysics Focused Telescope Assets WFIRST-AFTA Final Report, 2013. URL arXiv:1305.5422.

D. M. Stam. Spectropolarimetric signatures of Earth-like extrasolar planets. *A&A*, 482:989–1007, 2008. doi: 10.1051/0004-6361:20078358. URL http://cdsweb.u-strasbg.fr/cgi-bin/qcat?J/A+A/482/989.

D. M. Stam and J. W. Hovenier. Errors in calculated planetary phase functions and albedos due to neglecting polarization. *Astronomy & Astrophysics*, 444(1):275–286, 12 2005. ISSN 0004-6361. doi: 10.1051/0004-6361:20053698. URL http://www.aanda.org/10.1051/0004-6361:20053698.

D. M. Stam, J. F. De Haan, J. W. Hovenier, and P. Stammes. Degree of linear polarization of light emerging from the cloudless atmosphere in the oxygen A band. *Journal of Geophysical Research: Atmospheres*, 104 (D14):16843–16858, 7 1999. ISSN 0148-0227. doi: 10.1029/1999JD900159. URL https://onlinelibrary.wiley.com/doi/abs/10.1029/1999JD900159.

D. M. Stam, J. W. Hovenier, and L. B. F. M. Waters. Astronomy Astrophysics Using polarimetry to detect and characterize Jupiter-like extrasolar planets. *A&A*, 428:663–672, 2004. doi: 10.1051/0004-6361:20041578. URL http://dx.doi.org/10.1051/0004-6361:20041578.

E. R. Stofan, C. Elachi, J. I. Lunine, R. D. Lorenz, B. Stiles, K. L. Mitchell, S. Ostro, L. Soderblom, C. Wood, H. Zebker, S. Wall, M. Janssen, R. Kirk, R. Lopes, F. Paganelli, J. Radebaugh, L. Wye, Y. Anderson, M. Allison, R. Boehmer, P. Callahan, P. Encrenaz, E. Flamini, G. Francescetti, Y. Gim, G. Hamilton, S. Hensley, W. T. Johnson, K. Kelleher, D. Muhleman, P. Paillou, G. Picardi, F. Posa, L. Roth, R. Seu, S. Shaffer, S. Vetrella, and R. West. The lakes of Titan. *Nature*, 445(7123):61–64, 1 2007. ISSN 14764687. doi: 10.1038/nature05438.

M. Sylvestre, N. A. Teanby, L. Rossi, B. Seignovert, S. Vinatier, E. Lagadec, and M. Montargès. Polarimetric study of Titan's aerosols during its early northern summer. In *EPSC-DPS Joint Meeting 2019*. EPSC-DPS2019, 2019.

L. Szirmay-Kalos, B. Tóth, and M. Magdics. Monte carlo photon transport on the GPU. In *GPU Computing Gems Emerald Edition*, pages 247–262. Elsevier Inc., 1 2011. ISBN 9780123849885. doi: 10.1016/B978-0-12-384988-5.00017-6.

M. G. Tomasko. Preliminary results of polarimetry and photometry of Titan at large phase angles from Pioneer 11. *Journal of Geophysical Research*, 85(A11):5937, 11 1980. ISSN 0148-0227. doi: 10.1029/ja085ia11p05937.

M. G. Tomasko, B. Bézard, L. Doose, S. Engel, and E. Karkoschka. Measurements of methane absorption by the descent imager/spectral radiometer (DISR) during its descent through Titan's atmosphere. *Planetary and Space Science*, 56(5):624–647, 4 2008. ISSN 00320633. doi: 10.1016/j.pss.2007.10.009.

V. J. H. Trees and D. M. Stam. Blue, white, and red ocean planets - Simulations of orbital variations in flux and polarization colors. *A&A*, 626:A129, 2019. doi: 10.1051/0004-6361/201935399. URL https://doi.org/10.1051/0004-6361/201935399.

H. C. van de Hulst. *Multiple Light Scattering, Tables, Formulas, and Applications*, volume 1 and 2. Academic Press, New York, 1980. doi: 10.1016/b978-0-12-710701-1.x5001-0.

P. C. Waterman. Symmetry, unitarity, and geometry in electromagnetic scattering. *Physical Review D*, 3(4):825–839, 1971. ISSN 05562821. doi: 10.1103/PhysRevD.3.825.

R. A. West, A. L. Lane, H. Hart, K. E. Simmons, C. W. Hord, D. L. Coffeen, L. W. Esposito, M. Sato, and R. B. Pomphrey. Voyager 2 photopolarimeter observations of Titan. *Journal of Geophysical Research: Space Physics*, 88(A11):8699–8708, 11 1983. ISSN 01480227. doi: 10.1029/JA088iA11p08699. URL http://doi.wiley.com/10.1029/JA088iA11p08699.

B. A. Whitney. Monte Carlo radiative transfer. *Bulletin of the Astronomical Society of India*, 39:101–127, 2011.

K. Wood, B. Whitney, J. Bjorkman, and M. Wolff. Introduction to Monte Carlo Radiation Transfer. 2013. URL http://www-star.st-and.ac.uk/~kw25/research/montecarlo/book.pdf.